Stacking Faults and Twinning in Homoepitaxial Thin Films on Ir(111)

Inaugural-Dissertation

zur

Erlangung des Doktorgrades
der Mathematisch-Naturwissenschaftlichen Fakultät
der Universität zu Köln

vorgelegt von

Sebastian Bleikamp

aus Oberhausen

Köln, 2010

Berichterstatter:	Prof. Dr. Thomas Michely Prof. Dr. Mohsen Abd-Elmeguid
Vorsitzender der Prüfungskommission:	Prof. Dr. Ladislav Bohatý
Tag der mündlichen Prüfung:	12. April 2010

Abstract

The growth and annealing behavior of thin Iridium films on the Ir(111) surface was studied with respect to stacking fault and twin formation by means of scanning tunneling microscopy (STM), low energy electron diffraction (LEED) and surface X-ray diffraction (SXRD).

It was found that by heterogeneous nucleation of new faults at phase boundaries between areas of regular and faulted stacking, initial faulted areas spread into their surrounding (proliferation effect). In the process, the phase boundary is stabilized and evolves to a persistent fault structure, and a transition from layer-by-layer growth to a defect dominated growth with a fixed length scale takes place. During this transition, the majority of the surface area becomes twinned. A step-influenced enhancement of the stacking fault probability initially supports the effect.

By the supply of additional energy in the order of 50 eV per deposited atom using ion beam assisted deposition (IBAD), stacking fault and twin formation can be effectively lifted. Various strategies of IBAD have been tested.

The strongly twinned Ir/Ir(111) films exhibit a high stability against thermal annealing. Annealing is found to take place in a two step process: At 800 K-1000 K the boundaries between areas of different stacking are diminished. Only beyond 1200 K also the twins themselve heal. Structure models of the boundaries involved are presented. The boundaries between different stacking areas are identified to consist of {111}/{115} boundaries dissociated into coherent {111}/{111} and {112}/{552} boundaries.

The influence of adsorbates on the growth of Ir/Ir(111) was studied for CO and O. It was found that exposure of the sample to CO or O during deposition prevents coalescence, leads to columnar growth and multiple twinning. For both adsorbates, the island number density is increased, indicating a reduced mobility on the surface.

Contents

1 Introduction and Motivation 19

2 Background and Review of Previous Works 21
- 2.1 Thin Film Growth 21
- 2.2 Crystal Defects: Stacking Faults, Partial Dislocations and Twins 26
- 2.3 Thin Film Growth with Stacking Faults 28
- 2.4 Homoepitaxy on Ir(111) 34
- 2.5 Self-Healing of Stacking Faults in the System Ir/Ir(111) . . . 38

3 Experimental Details and Methods 41
- 3.1 Experimental Setup for the STM and LEED Experiments: UHV Systems Tuma III and Athene 41
- 3.2 Experimental Setup for the SXRD Experiments at the Beamline BM32 of the ESRF 43
- 3.3 Experimental Procedure 45
- 3.4 SXRD 45
  - 3.4.1 Penetration Depth 46
  - 3.4.2 Basics of Surface X-ray Scattering 48
  - 3.4.3 Application to Ir(111) 50
- 3.5 Ion Beam Assisted Deposition 53

4 Evolution of Stacking Faults and Twinned Areas in Thin Films 57
- 4.1 Growth at 350 K 57
- 4.2 The Proliferation Effect 64
- 4.3 Methods of Stacking Fault and Twin Detection 67
  - 4.3.1 Direct Observation of Stacking Faults in the First Monolayer by STM 67
  - 4.3.2 Stacking Fault Detection after Deposition of a Few Monolayers by STM 68
  - 4.3.3 Measuring the Surface Area of Twin Crystallites by LEED 70

4.3.4 Twin Crystallite Identification in Annealed Films by STM through Post Decoration . . . 72
4.3.5 Quantitative Comparison of LEED and STM Methods Applied to Annealed Films . . . 73
4.4 Influence of Stacking Faults and Twinning on the Growth Beyond the First Monolayer . . . 74
4.4.1 Layer Dependence of P_{F} and θ_{F} . . . 76
4.4.2 Influence of the Proliferation Effect . . . 78
4.5 Conclusion . . . 81

5 Annealing Behavior and Stability of Twinned Films 83
5.1 Results . . . 83
5.1.1 STM Experiments . . . 84
5.1.2 SXRD Experiments . . . 88
5.1.3 Comparison . . . 92
5.2 Discussion . . . 94
5.3 Conclusion . . . 99

6 Suppression of Twin Crystallite Formation by Ion Beam Assisted Deposition 101
6.1 IBAD Strategies to Suppress Twinning . . . 101
6.2 Results . . . 102
6.3 Discussion . . . 110
6.4 Conclusion . . . 113

7 Effect of Adsorbates on Twin Crystallite Formation 115
7.1 Adsorbates Used and Their Adsorption Sites . . . 115
7.2 Results and Discussion . . . 116
7.3 Conclusion . . . 120

8 Summary 121

Bibliography 123

List of Publications 133

Deutsche Kurzfassung 135

Danksagung 137

Offizielle Erklärung 139

Lebenslauf 141

List of Figures

2.1 Growth modes in epitaxy close to the thermodynamical equilibrium . . . 22
2.2 Growth regimes in homoepitaxy . . . 24
2.3 Schematic representation of stacking sequences . . . 27
2.4 Schematic structure of an embedded twin . . . 28
2.5 Homoepitaxy of Ag/Ag(111) . . . 29
2.6 Homoepitaxy of Cu/Cu(111) . . . 30
2.7 STM images of Co/Cu(111) . . . 31
2.8 STM images of Co/Pt(111) . . . 32
2.9 Twin boundary movement of Ag/Ru(0001) . . . 33
2.10 Atomistic model of stacking fault nucleation . . . 34
2.11 STM images of Ir islands on Ir(111) at various growth temperatures . . . 35
2.12 Island density for Ir/Ir(111) . . . 36
2.13 Relative stacking fault probability for Ir/Ir(111) . . . 37
2.14 Ball model of the self-healing effect . . . 38
2.15 Self-healing effect at intersecting A-gaps . . . 39
2.16 STM image of decoration rows on Ir/Ir(111) . . . 40

3.1 Sketch of the vacuum chamber Athene . . . 42
3.2 Experimental setup at the beamline BM32 of the ESRF . . . 44
3.3 Scheme of the main movements of the diffractometer . . . 45
3.4 X-ray attenuation length . . . 48
3.5 CTR maps for fcc crystals . . . 52
3.6 Island number densities for Pt/Pt(111) . . . 53

4.1 STM topographs after deposition of 0.20 ML - 5.00 ML of Ir on Ir(111) at 350 K . . . 58
4.2 STM topographs after deposition of 10 ML - 90 ML of Ir on Ir(111) at 350 K . . . 59
4.3 Ball model of the Ir(111) surface . . . 60
4.4 RMS roughness for coverages up to 90 ML . . . 62

4.5 Average lateral length scale and average distance of decoration rows for coverages up to 90 ML 63
4.6 STM topograph and schematic drawing illustrating the proliferation effect 64
4.7 Ball model of the proliferation effect 65
4.8 STM topographs after deposition of 2.18 ML at 350 K, colored with respect to the stacking sequence 68
4.9 LEED I/V spectra 71
4.10 Illustration of the post decoration method 72
4.11 Comparison of θ_{F} for a 90 ML Ir film between LEED and STM 74
4.12 Fraction of surface area covered by stacking faults θ_{F} versus Θ 75
4.13 Comparison of STM topographs of films grown at 350 K and below 210 K 76
4.14 STM topographs after sputtering and successive deposition 78
4.15 Ball model of the proliferation effect for up to four layers . . 80

5.1 STM topographs of 90 ML Ir/Ir(111) after annealing to different temperatures 84
5.2 STM topographs and linescans showing fractional steps after annealing 86
5.3 STM topographs of Ir/Ir(111) after annealing, marked with respect to the stacking sequence 87
5.4 Map of the calculated peak positions at CTRs 89
5.5 Scans of the $(10L)^{hex}$ and the $(01L)^{hex}$ CTRs 90
5.6 Integrated intensity at the $(011)^{hex}$ position during deposition 91
5.7 Scans along the $(\,0\,K\,(3-K)\,)^{hex}$ and $(\,H\,0\,(3-H)\,)^{hex}$ CTRs 91
5.8 Results of the annealing experiments for STM, LEED and SXRD 93
5.9 Model of possible incoherent twin boundaries involving low index planes 95
5.10 Ball models for incoherent high symmetry twin boundaries . 97
5.11 Calculated intensity maps for various {111}/{115} boundary structures 98

6.1 STM topographs of Ir(111) after sputtering and subsequent annealing 103
6.2 STM topographs of Ir(111) after deposition at 350 K with PVD and IBAD 104

6.3 RMS roughness of PVD and IBAD films as function of deposited amount . . . 106
6.4 θ_{F} and P_{F} for homogeneous nucleation as function of the deposited amount . . . 107
6.5 λ_{DR} and $\xi_{\mathrm{fDR/DR}}$ as a function of the deposited amount . . . 108
6.6 STM topographs of annealed films grown with either PVD or IBAD . . . 110

7.1 STM topographs of 0.2 ML Ir/Ir(111) deposited with and without adsorbates . . . 116
7.2 STM topographs of 50 ML Ir/Ir(111) deposited with adsorbates . . . 118

List of Tables

7.1 Comparison of 50 ML Ir/Ir(111) grown with and without adsorbates. 118

Frequently Used Symbols

Symbols

α_c	critical angle for total reflection
B_j	B-factor of the Debye-Weller factor
c	speed of light in vacuum
d_R	average seperation of decoration rows
e	elementary charge
E	energy
E_{coh}	cohesive energy
E_D	activation energy for diffusion
E_e, E_a, E_c	amplitude of the scattered electric field of an electron / atom / crystal
$f_0, f^{`\prime}, f''$	atomic form factor and related dispersion corrections
F	free energy
$F(\boldsymbol{q})$	structure factor
γ	surface free energy
γ_D	surface free energy of the deposit
γ_I	interface free energy
γ_S	surface free energy of the substrate
I	intensity
$\boldsymbol{k}$	wave vector
k_B	Boltzmann's constant
λ	wavelength (also: average length scale)
λ_{DR}	decoration row length per unit area
Λ	$1/e$ X-ray penetration depth
m_e	electron mass
μ	chemical potential
μ_a	linear absorption coefficient
n	index of refraction
ν	frequency

ν_0	attempt frequency
σ	supersaturation
p	pressure
P	polarization factor
P_F	probability for homogeneous nucleation of islands in stacking fault positions
P_{hcp}	probability of finding a cluster or island in faulted (hcp) stacking (equivalent: P_{sf}, P_{SFI})
P_{fcc}	probability of finding a cluster or island in regular (fcc) stacking (equivalent: P_{reg}, P_{RI})
$\boldsymbol{q}$	momentum transfer
ρ_a	atomic electron density
T	temperature
θ_F	fraction of faulted surface area
Θ	deposited amount
ϑ	angle of incidence
V	volume
$\xi_{\mathrm{fDR/DR}}$	ratio of fat decoration rows and derived elongated structures to thin monoatomic decoration rows
Y	sputtering yield
Y^{step}	step edge sputtering yield
Y^{terr}	terrace sputtering yield

Abbreviations

a.u.	arbitrary units
DR	decoration row
ESRF	European Synchrotron Radiation Facility
fcc	face centered cubic
fDR	fat decoration row
FIM	field ion microscopy
GMR	giant magnetoresistance
hcp	hexagonal close packed
IBAD	ion beam assisted deposition
KMC	kinetic Monte Carlo (simulation)
LDOS	local density of states
LEED	low energy electron diffraction
ML	monolayer

PVD	physical vapor deposition
RHEED	reflection high energy electron diffraction
RI	regular island
r.l.u.	reciprocal lattice units
r.s.u.	reciprocal space units
RT	room temperature
SF	stacking fault
SFI	stacking fault island
STM	scanning tunneling microscopy
SXRD	surface X-ray diffraction
tDR	thin (monoatomic) decoration row
TEM	transmission electron microscopy
UHV	ultra high vacuum
XRD	X-ray diffraction

1 Introduction and Motivation

Since the early 50s of the last century, microelectronics and microtechnology have continuously gained in importance in today´s technical applications from year to year. Nowadays, nearly every technical device depends on microtechnology, be it a computer, a mass storage device, or a cell phone. With the continuous progression in miniaturization and the advancement from micro- to nanostructures, new effects become important, and new challenges arise.

Nanotechnological applications often demand the production of ultrathin metallic films with high quality. Unfortunately, many of the technically interesting transition metals with face centered cubic (fcc) crystal structure are susceptible to the formation of stacking faults during growth, which give rise to twin boundaries and twin crystallite formation [1].

Prominent examples of such materials are systems like Cu/Cu(111) [2, 3, 4], Ag/Ag(111) [5, 6], or Ir/Ir(111) [7, 8, 9] where stacking faults are formed during growth in large numbers. But stacking fault nucleation and the ensuing twin crystallite formation is not limited to homoepitaxy. In Co/Cu(111) heteroepitaxy [10, 11, 12], a system important for magnetic applications due to the giant magnetoresistance (GMR) effect [13, 14] and its applications in spintronics [15, 16], Co forms in two or three layer high islands with both regular and twinned fcc stacking.

Stacking faults and twin boundaries can give rise to pronounced property changes. The magnetic properties of deposited thin and ultra thin films are known to crucially rely on the stacking sequence [17, 18, 19]. The local density of states (LDOS) near the Fermi level of stacking faults islands in Ir/Ir(111) [20] or twinned multilayer islands of Co/Cu(111) [21] differs significantly from the one of regular islands.

Although stacking faults may cause desirable effects, e.g. remnant magnetization in small Pd nanocrystals [22, 23, 24, 25], more commonly they cause a deterioration of properties: Twin boundaries act as traps for electrons in SiC [26, 27], limit the performance of optoelectronic III-V nanowire-based devices [28], cause degradation of the active area in devices through fault expansion under operation conditions [29] and act as electron scattering planes, which is of especial importance for the electronic properties of metal nanowires due to the fact that the lateral dimensions become comparable to the electron mean free path [30].

As these examples show, stacking faults and twin crystallites in thin films are usually highly undesirable, and both detailed knowledge about the atomic processes that lead to their formation as well as strategies for the suppression of their formation and removal are of special scientific and technological interest.

Due to its properties, Iridium is ideally suited as a test system: In Ir/Ir(111) homoepitaxy, stacking faults form for kinetic reasons only. The amount of stacking faults initially formed is strongly temperature dependent and therefore easily tunable [8, 9]. Iridium is also a relatively hard material with nearly no relaxation, so that structures can be modeled in first approximation by a hard sphere model.

The present work on Ir/Ir(111) aims at promoting our understanding of the mechanisms of formation and evolution of stacking faults, twin crystallites and the associated boundaries during growth and annealing, as well as developing methods for the production of defect free films.

The work is divided into three parts: In the first part (Chapter 4) the processes during growth in a range from single islands up to thin films are investigated using using scanning tunneling microscopy (STM) and low-energy electron diffraction (LEED). Special attention is paid to processes at boundaries between different stackings, as recent investigations of the dynamics of twin boundary motion for epitaxial films of a few layer thickness highlighted the interdependence of twin boundaries and growth processes [31, 32]. The second part (Chapter 5) deals with the annealing of the films grown. To access the boundary structures below the surface, the STM and LEED investigations are extended with complementary surface X-ray diffraction (SXRD) performed at the beamline BM32 of the European Synchrotron Radiation Facility (ESRF). In the third part (Chapters 6 and 7) the results of the investigation of the influence of ion beam assisted deposition (IBAD) and adsorbates on stacking fault and twin crystallite formation are presented. It will be shown that the formation of twin crystallites can be completely suppressed using IBAD.

2 Background and Review of Previous Works

This chapter is dedicated to giving the reader an introduction in the topic. In the first part of the chapter, the theoretical concepts of thin film growth and the basics of crystal defects and stacking-fault formation are presented as a basis for future discussion. This is followed by a description of the effects of stacking faults in other systems and a review of previous works on Ir/Ir(111).

2.1 Thin Film Growth

Expressed in physical terms, crystal and thin film growth are both performed by the transport of material to the substrate and a subsequent phase transition of the deposited material from vapor or liquid phase to the solid phase. The driving force for this process is the difference in vapor pressure between the different phases. The main difference between crystal growth on the one hand and epitaxy and thin film growth on the other is the difference in strength of the driving force for the phase transition between the different processes. The supersaturation

$$\sigma = \ln \left(p_1 / p_2 \right) \,, \tag{2.1}$$

simplified in the case of identical materials for substrate and deposit to

$$\sigma = \ln \left(p(T_1) / p(T_2) \right) \,, \tag{2.2}$$

is a measure for the driving force. The difference in chemical potential between both phases is given by

$$\Delta\mu = \sigma k_B T \,. \tag{2.3}$$

Typical crystal growth is carried out close to equilibrium. The value of the supersaturation is around the order of unity and the difference in chemical

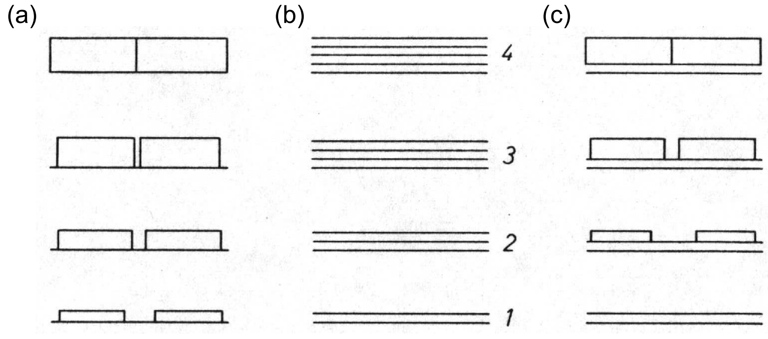

Figure 2.1: Growth modes in epitaxy close to the thermodynamical equilibrium: (a) Volmer-Weber growth mode, (b) Frank-van-der-Merwe or layer-by-layer growth mode and (c) Stranski-Krastanov growth mode. From Ref. [34].

potential is – with values about 10 meV – close to being neglectable. The low gain in energy by adsorption is the reason that only the energetically optimal binding sites are stable binding sites and get populated during growth.

In contrast, in thin film deposition methods like physical vapor deposition (PVD) with deposition from a hot wire or crucible to a substrate at lower temperatures, typical values of σ are several orders of magnitude higher. The difference in chemical potential is in the range of several eV for typical deposition conditions. The gain in energy by adsorption of atoms from the gas phase on the solid is sufficient to also populate energetically unfavorable adsorption sites, giving rise to the growth of a variety of structures ranging from perfect epitaxy over fault formation to completely amorphous growth.

The morphology of such films depends both on energetic and kinetic effects. In the following, the differences between energetic and kinetic effects and their impact on the growth mode in epitaxy will be described exemplarily to reveal the conceptual differences.

In epitaxy[1] [33], the deposit grows in crystalline layers on the substrate, but the crystalline substrate imposes an order on the deposit layer that is not necessarily equal to the equilibrium structure of the deposit.

Close to the thermodynamical equilibrium, the resulting structures are predominantly defined by the balance of the surface free energy of the substrate γ_S, surface free energy of the deposit γ_D and the interface free energy

---

[1] Epitaxy: A term derived from the words *epi* (greek for: on top) and *taxis* (greek for: to arrange or to order).

γ_I. For

$$\gamma_S < \gamma_D + \gamma_I, \tag{2.4}$$

three-dimensional islands form due to the minimization of the surface covered by the deposit (Volmer-Weber growth mode, Fig. 2.1(a)). In the opposite case

$$\gamma_S > \gamma_D + \gamma_I, \tag{2.5}$$

the surface will be completely covered by the deposit (Frank-van-der-Merwe or layer-by-layer growth mode, Fig. 2.1(b)).

In heteroepitaxy, i.e. in the epitaxy of different materials for substrate and deposit, the first layers will be usually strained due to structural differences between substrate and deposit. This can lead to the evolution of a third growth mode due to the relaxation in higher layers: Although the surface free energies γ_S and γ_D are equal, the different strain between layers causes a positive interface energy γ_I, and thus the growth of three-dimensional islands on top of the first deposited layers of the same material (Stranski-Krastanov growth mode, Fig. 2.1(c)).

In homoepitaxy, i.e. the epitaxy of equal materials for substrate and deposit with equal surface free energies $\gamma_S = \gamma_D$, no strain and no interface free energy, the growth is – by the consideration of surface free energies – expected to be a perfect layer-by-layer growth for an infinite amount of layers. Therefore deviations from perfect layer-by-layer growth in homoepitaxy can be only based on the growth kinetics. The absence of energetic reasons for deviations from perfect layer-by-layer growth in homoepitaxy thereby offers the possibility to study growth kinetics in pure form.

Thin film growth usually takes place far from equilibrium, and growth kinetics have a major impact on the morphology.

From a kinetic point of view, the morphology of thin films is mainly determined by different processes of diffusion. The probability of a process and its rate or frequency ν is determined by the the energy barrier E_D that has to be overcome between the initial and the final state. Using the Arrhenius law for the thermally activated process, the frequency is given by

$$\nu = \nu_0 \exp^{-E_D/k_B T}, \tag{2.6}$$

with ν_0 being the constant attempt frequency. The main difference between the previous energetic approach is the importance of the energy barrier E_D: Even in a situation, where an energetically favorable state exists that gives rise to a pronounced minimization of the free energy once reached, the system

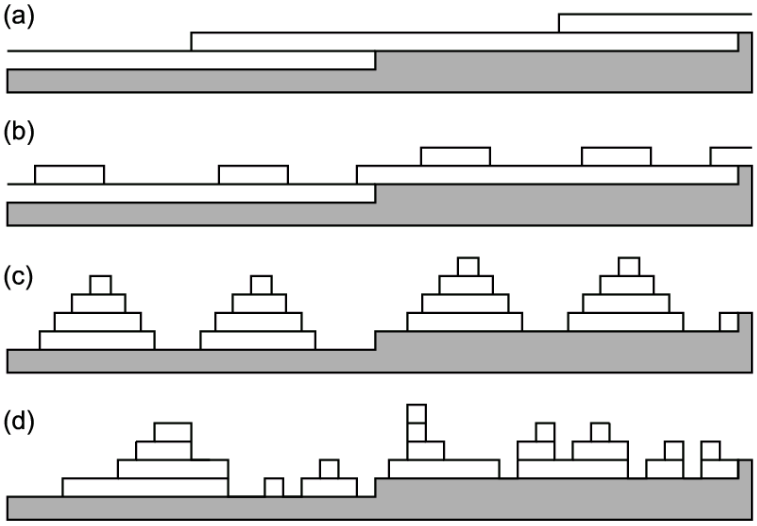

Figure 2.2: Growth regimes in homoepitaxy: (a) step flow growth (high mobility), (b) layer-by-layer growth (high interlayer transport), (c) mound formation (low interlayer transport), (d) self-affine growth (very low mobility). From Ref. [35].

will not necessarily undergo this transition. If the energy barrier between both states is too high or the temperature is too low, the rate at which the process happens will be low and the transition will not happen on the timescale of the experiment. The system will remain in the energetically less favorable state, as it is not able to reach the favorable state.

In this view, the morphology of thin films depends on the balance between the different kinds of diffusion processes that govern mass transport and the deposition rate that determines the density of adatoms on the surface. Depending on the balance, different structures arise.

Before discussing these structures, the basic concepts of the nucleation process have to be clarified. A clear distinction between cluster stability and cluster mobility has to be made: Atoms and atom clusters on the surface can be either mobile or immobile on the timescale of the experiment, depending on the temperature and – in case of clusters – on their size. In a typical growth situation of metals, single atoms (adatoms) and small clusters up to a given size (the largest mobile cluster) are mobile on the surface. Clusters grow or shrink by the attachment or detachment of further atoms or clusters.

The mobility of adatoms typically exceeds the mobility of even small clusters by far, and cluster growth and decay can be solely attributed to adatom attachment or detachment, respectively. In the atomistic nucleation theory [36], the clusters on the surface are furthermore divided into stable and unstable ones. Only once clusters have grown larger than a critical size they are regarded as being stable and are assumed not to decay on the timescale of the experiment, i.e. to be persistent objects. Although stability and mobility are not directly linked, stable clusters grow and in consequence become eventually larger than the largest mobile cluster, i.e. immobile. In the atomistic nucleation theory, such stable clusters are already referred to as "islands". In this work, the focus is set on the stacking sequence of islands, which remains undetermined until immobilization. For this reason, only clusters that are both stable and immobile are referred to as islands within the scope of this work. With this background, the discussion of the different structures is now resumed:

For a very low mobility, diffusion is completely suppressed and even single atoms are already immobile. Deposited atoms remain at the place where they are deposited. The structures formed have a random appearance. This growth mode is called self-affine growth ((Fig. 2.2(d)).

Surfaces are never perfect but always stepped. If in the opposite case to the previous example, the mobility is high compared to the deposition rate and to the average step distance, the probability for adatoms to reach a preexisting step on the surface is much higher than the probability to meet another cluster and form a new island. No new islands are formed and the film grows only by attachment of material to the preexisting steps. This growth mode is called step-flow growth (Fig. 2.2(a)).

Islands are only formed in an intermediate situation with less mobility and higher deposition rate, in which adatoms often meet other clusters. The resulting morphology depends strongly on the interlayer mass transport:

During their diffusion over the surface, adatoms encounter steps edges from both sides which originate both from preexisting steps as well as arise from islands. The energy landscape at a step differs from the terrace especially by the presence of an additional energy barrier for crossing the step, the Ehrlich-Schwoebel barrier [37]. Incorporation at the lower side of the step is energetically preferential, and step edges that are approached from the lower side lead directly to the attachment of the cluster to the step. The approach from the upper side can both lead to attraction as well as repulsion depending on the strength of the Ehrlich-Schwoebel barrier.

Is this additional barrier negative, i.e. lowers the diffusion barrier for crossing the step, adatoms get incorporated in the step. In the case of perfect interlayer transport, the next layer growth only after the first is completely filled. This regime is called layer-by-layer growth (Fig. 2.2(b)).

For a large positive Ehrlich-Schwoebel barrier, i.e. an increase in the barrier for crossing the step, adatoms are repelled and remain on the upper terrace. Interlayer mass transport is prohibited. In case of an island, clusters on top of it are trapped and will form the nuclei for the next layer. This is repeated for the following layers, and mounds with a steadily growing number of layers are formed. Accordingly, this regime is called mound formation (Fig. 2.2(c)).

The latter example emphasizes the impact of kinetic effects in thin film growth: Although energetically preferred adsorption sites may exist, they might not be occupied for kinetic reasons. On the other hand, due to the situation being far from equilibrium, also metastable adsorption sites may get occupied during growth. For this reason, imperfect films with variety of crystal defects and fault structures are often formed during the growth of thin films, which will be addressed in next section.

A deeper introduction into the physics of thin film growth can be found by the interested reader for example in the book "Islands, Mounds and Atoms" by T. Michely and J. Krug [35].

2.2 Crystal Defects: Stacking Faults, Partial Dislocations and Twins

Both the face centered cubic (fcc) and hexagonal close packed (hcp) crystal structure can be described as a sequence of single layers of atoms in [111] direction. Within the (111) layers, the atoms are in a hexagonal arrangement. Each (111) layer possesses two different kinds of hollow sites, in which the atoms of the next layer can rest. The sites differ in the resulting displacement between the layers and define the final crystal structure.

In the hcp structure, the occupation of these sites alternates from layer to layer, and so does the lateral displacement of the layers. Using the notation introduced by Frank [38] to denote layers in different registers, the resulting stacking sequence is ABAB (Fig. 2.3). Opposed to hcp, in the fcc structure only one of the two sites is occupied. As a result, only every third layer has the same lateral displacement as another one, and the stacking sequence is ABCABC.

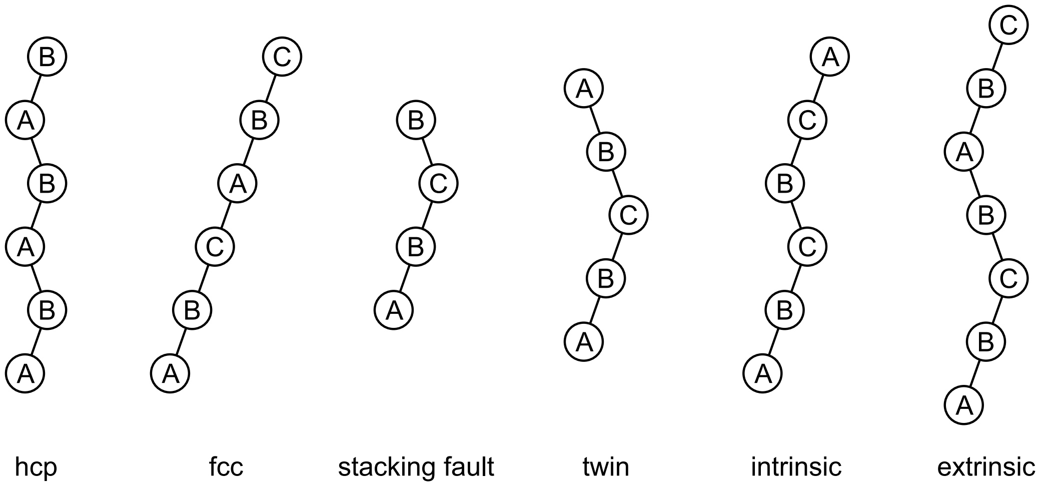

Figure 2.3: Schematic representation of the stacking sequences of the hcp and fcc crystal structures, of a stacking fault, a twin and intrinsic and extrinsic stacking faults.

Deviations from these sequences are called stacking-faults. If the regular fcc stacking sequence is broken by occupation of one layer in the other hollow site, i.e. ABCB instead of ABCA, a stacking fault is formed. Compared to grain boundaries or surfaces, stacking faults have rather low interface energies as no bonds are broken. Nevertheless, the structure is locally hcp (BCB), and in an fcc crystal energetically not favorable. From a crystallographic point of view, stacking faults are Shockley partial dislocations [39]: Stacking fault layers are slipped by a vector of $\frac{1}{6} < \bar{2}11 >$ on the (111) plane and as such displaced by less than a unit lattice vector [40].

An intrinsic stacking fault may be created by shearing one half of an fcc crystal across a (111) plane by the vector $\frac{1}{6} < \bar{2}11 >$. Repeated shearing of subsequent layers leads to an extrinsic stacking fault. By the shearing operation, always two stacking faults are created which together form the intrinsic or extrinsic stacking fault.

Above a single stacking fault, the fcc stacking sequence is continued, but due to the fault the stacking sequence is reversed: Instead of ABC it is CBA. For this obvious relationship to the regular one, the new stacking sequence is called twinned and crystallites in this stacking are referred to as twins. Upon continued growth, twins get embedded into the regular matrix, which leads to the evolution of further boundaries at the sides. While a stacking fault forms a coherent twin boundary, the new boundaries are incoherent

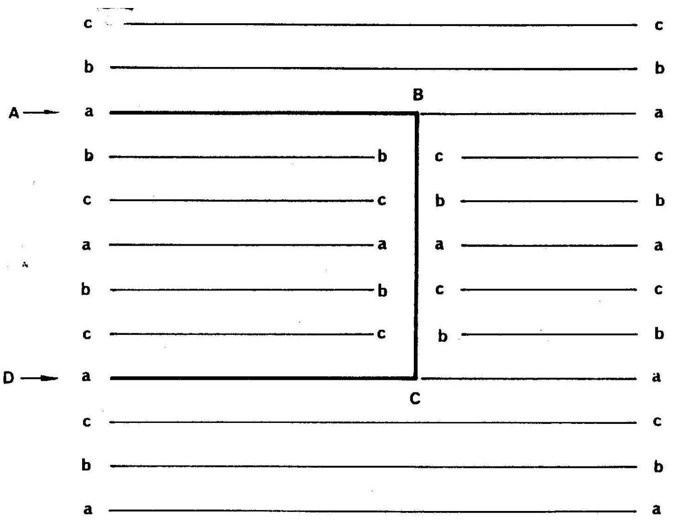

Figure 2.4: Schematic structure of an embedded twin and the respective twin boundaries. AB and CD: Coherent twin boundaries, BC: Incoherent twin boundary. Small letters denote the stacking sequence. From Ref. [1].

as shown in Fig. 2.4 and disturb the crystal rather strongly. Therefore the quality of thin films depends decisively on the density of stacking-faults.

2.3 Thin Film Growth with Stacking Faults

Many fcc materials are susceptible to the formation of stacking faults during epitaxial growth on the (111) surface. Prominent examples of such materials in homoepitaxy are silver and copper, where stacking faults are formed during growth in large numbers.

Due to the energetic preference of certain dense packed microfacets over others, islands may develop characteristic shapes. For example, the exterior shape of islands is often formed by $\{100\}$ or $\{111\}$ microfacets, which lie on opposite sites for regular and stacking fault islands. For this reason, the shapes of both kind of islands appear rotated by 180°. In case of a preference of one kind of facet over an other, e.g. of a preference of $\{111\}$ microfacets over $\{100\}$ facets, triangular islands form. The tips of the triangular shapes point in opposite directions for regular and stacking fault islands, allowing an easy distinction between both. In case all microfacets are equal in preference,

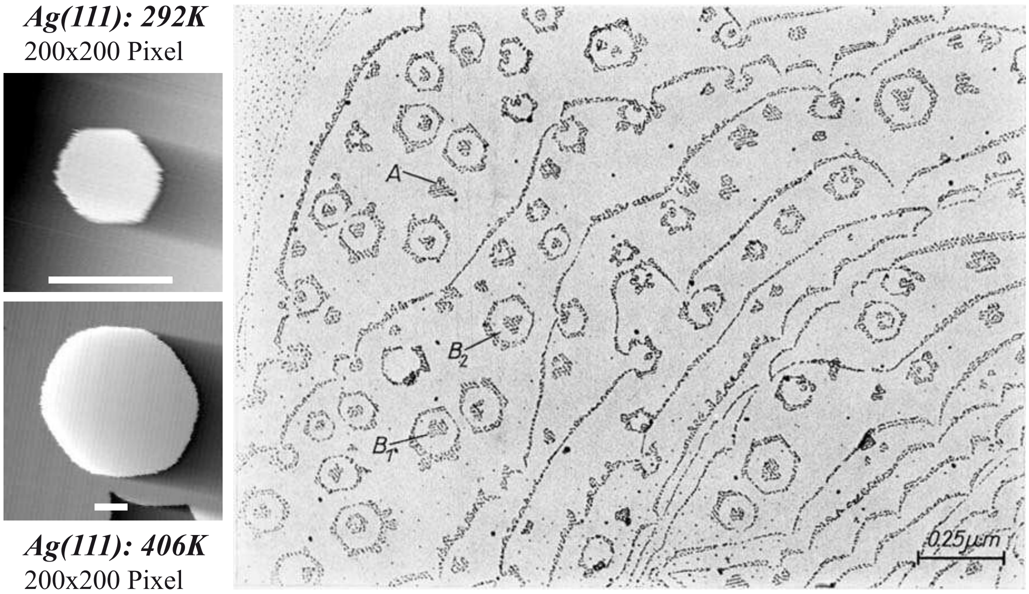

Figure 2.5: Homoepitaxy of Ag/Ag(111). (left) STM images of Ag islands grown at 292 K and 406 K. The white bar in each image corresponds to a length of 20 nm. Modified from Ref. [41]. (right) Growth of Ag on Ag(111) studied by Au decoration. The Au island marked with A continues the fcc stacking of the bulk. B_1 and B_2 mark Au islands grown on a regular (B_1) and twinned (B_2) Ag island. From Ref. [5].

hexagonal islands form which are hard to distinguish and other means of identification are necessary.

A typical example is Ag/Ag(111): During the growth of Ag on the Ag(111) surface, hexagonal islands are formed. Fig. 2.5 shows STM images of typical Ag islands at various temperatures [41]. These show a distinctive hexagonal shape consisting of {100} and {111} microfacets of equal length, and direct distinction between regular and stacking fault islands from different shapes is not possible.

Meinel et al. [5] investigated the growth of stacking faults in the system Ag/Ag(111) with Transmission Electron Microscopy (TEM). To identify regular and faulted islands, a post decoration method was deployed: On top of the Ag islands, a small amount (about 10% of a monolayer) Au was deposited. Due to the preference of only {100} microfacets, Au islands form triangular islands. The Au islands continue the stacking sequence of the Ag layer below. By comparison of the orientation of Au islands on top of the

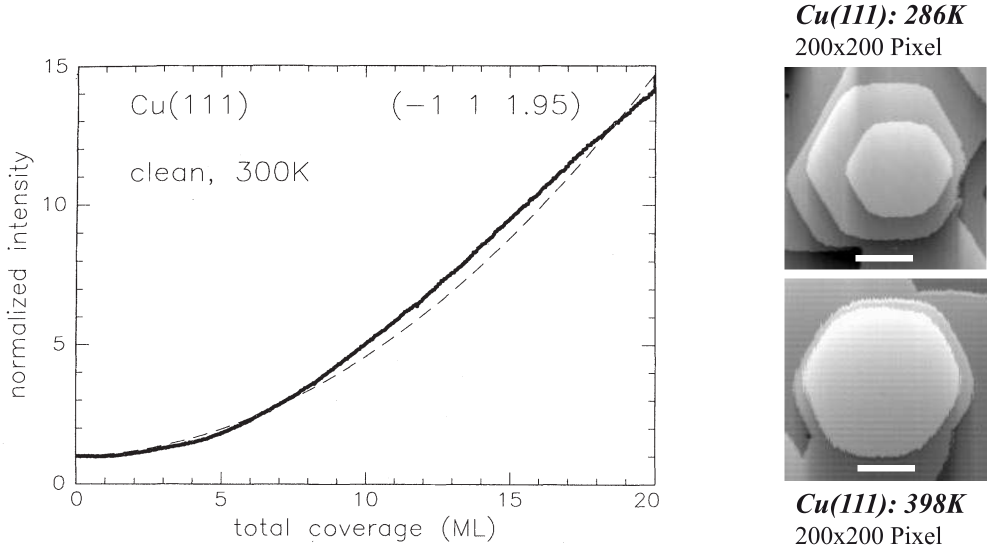

Figure 2.6: Homoepitaxy of Cu/Cu(111). (left) Evolution of the SXRD intensity at a position sensitive to twins during growth at 300 K. From Ref. [2]. (right) STM images of Cu islands grown at 286 K and 398 K. The white bar in each image corresponds to a length of 20 nm. Modified from Ref. [41].

Ag islands and of the orientation of Au islands on the terraces, an easy distinction of the underlying Ag islands in regular or stacking fault islands, is possible: On the right hand side of Fig. 2.5, a typical TEM image from Ref. [5] is shown. Au islands on the terrace point with one tip of the triangle to the top. Such an island has been marked as A. Two Ag islands have been marked with B1 and B2. The triangular Au island on top of the Ag island B1 points in the same direction as the Au island A, whereas the Au island on B2 points in the opposite direction. This indicates that B1 has the same stacking as sequence as the bulk and thus is a regular island, as opposed to B2 that has an inverted stacking sequence and thus is a stacking fault island.

A further example for a prominent system that is susceptible to stacking faults during growth is Cu/Cu(111). Cu forms similar hexagonal islands during growth as Ag does, so that direct distinction of the stacking sequence from the shape is also not possible. The evolution of such stacking faults and the resulting twin crystallites at room temperature has also been measured by SXRD for Cu/Cu(111). Both the investigations of Vegt et al. [2] (Fig. 2.6) and Camarero et al. [3] show a steady increase in the signal from twinned

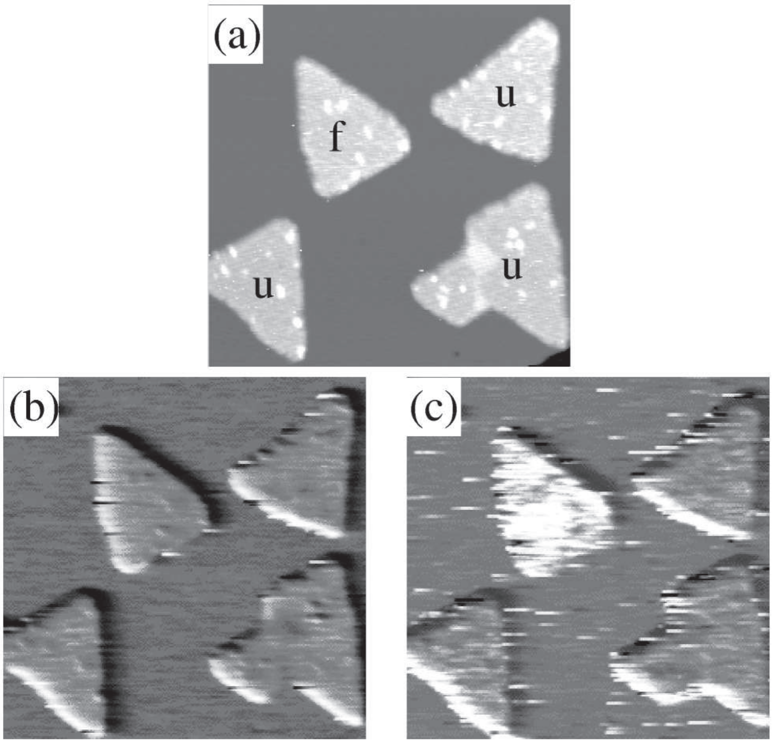

Figure 2.7: STM images after deposition of 0.4 ML of Co on Cu(111) at room temperature. (a) Topographic image. (b),(c) Spectroscopic (dI/dV) images at (b) -1.5 V and (c) +1.5 V. Image size 50 nm × 50 nm. From Ref. [21].

material with film thickness. Both measurements agree that continuously new stacking faults are formed and, as a consequence, more material gets twinned with increasing film thickness.

Stacking fault formation is not exclusive to homoepitaxy. A good example is the heteroepitaxy of Co on fcc transition metals like Co/Cu(111) or Co/Pt(111). These systems are well known for their special magnetic properties. Although Co exhibits the hcp structure, in heteroepitaxy on an fcc material it assumes the fcc stacking of the substrate material. As Co is originally hcp, it is not surprising that in these systems stacking faults are often formed.

Fig. 2.7(a) shows STM topographs of Co/Cu(111) [21]. After deposition of 0.4 ML Co at room temperature, triangular Co islands have formed.

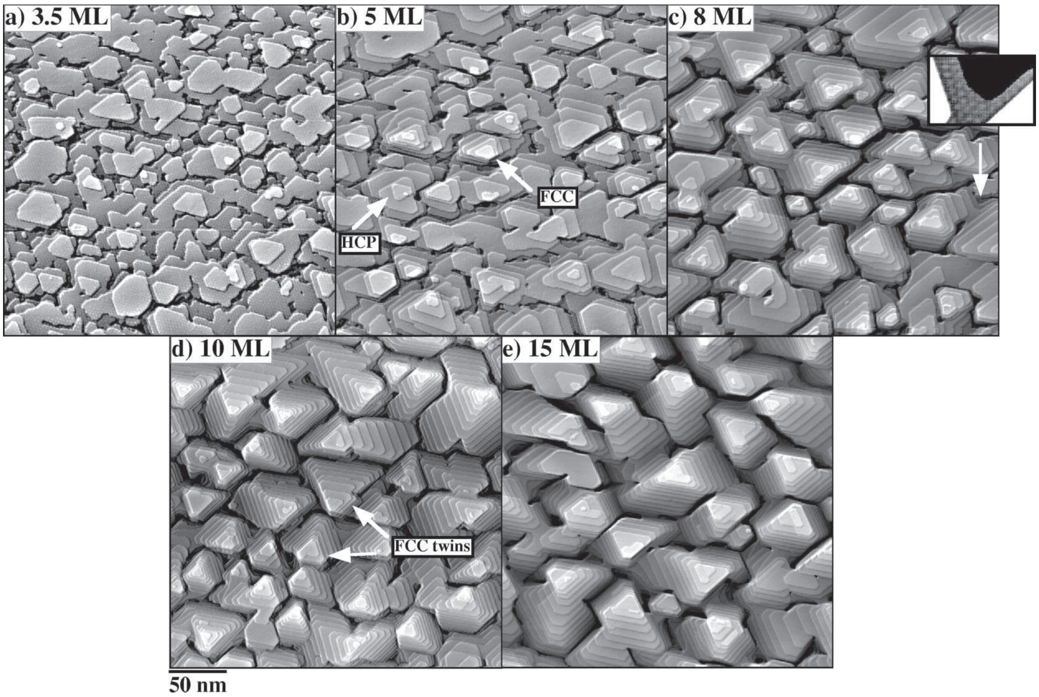

Figure 2.8: STM images after the deposition of different amounts of Co on Pt(111): (a) 3.5 ML, (b) 5 ML, (c) 8 ML, (d) 10 ML, (e) 15 ML. Arrows in (b) and (d) mark mounds in regular fcc, twinned fcc and hcp stacking. Image size 300 nm × 300 nm. From Ref. [42].

The islands are three layers high, with the first layer being within the Cu surface. The island pointing to the upper left has nucleated as a stacking fault island and continuously grown three layers heigh in twinned fcc stacking. Fig. 2.7(b) and (c) shows the corresponding spectroscopic $(dI)/(dV)$ images, measured at a bias voltage of (b) -1.5 V and (c) +1.5 V. At -1.5 V, both kind of islands appear equal. For 1.5 V, the stacking fault island appears much brighter, indicating a pronounced difference in the local density of states (LDOS). In fact, detailed spectroscopic measurements and simulations of the band structure show distinct differences in the band structure above the Fermi Level, that are caused by the break in symmetry in the xy plane due to the stacking fault and the resulting different hybridization between the $d_{xz} - d_{yz}$ orbitals of the Co layer. Changes in the LDOS have been also observed for stacking faults in the system Ir/Ir(111) [20].

A similar system is Co/Pt(111). Lundgren et al. [42] investigated the growth of thin films up to 15 ML using STM (Fig. 2.8). Initially, the growth

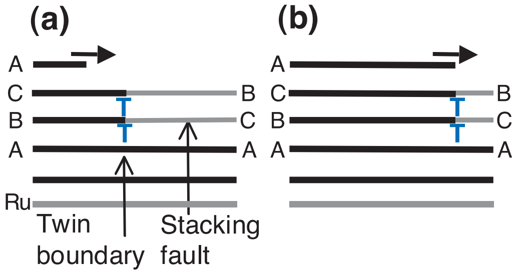

Figure 2.9: Schematic illustration of twin boundary movement in the system Ag/Ru(0001): (a) A stacking fault in the third Ag layer causes the two film regions next to the boundary to have different stacking sequences. (b) On continued growth, the twin boundary moves in step direction with the step edge of the advancing fifth Ag layer. The stacking in the twinned region changes, and the twinned region shrinks. From Ref. [32].

mode of the Co is 2D with no distinctive shapes, but changes to 3D with the growth of triangular mounds after deposition of approximately 5 ML. The authors attribute the initial 2D growth mode to the strain in the lower layers, which results in a moiré structure and an overlayer with a high density of kinks and corners, which are known to promote interlayer mass transport. With increasing coverage the influence of the strained interface decreases, resulting in a lower number of kinks and corners, decreased interlayer mass transport and a transition to 3D growth and a triangular shapes (compare Chapter 2.1, Stranski-Krastanov growth mode).

As for Co/Cu(111), both regular and stacking fault Co islands nucleate on the Pt(111) surface. Upon further deposition, they grow to mounds in either regular or twinned fcc stacking with their triangular shapes pointing in opposite directions. Two of such mounds have been marked in Fig. 2.8(d). In few cases, like in Fig. 2.8(b), also mounds in hcp stacking with the triangular shape alternating from layer to layer can be found.

Twins and crystallites in regular stacking have different stacking sequences and cannot directly coalesce without the creation of an additional boundary. Thus upon coalescence, an additional – mostly incoherent – twin boundary is formed. Twin boundaries are not necessarily stable and passive objects, but can both be influenced by and influence further growth. For example, Ling et al. [32] highlighted an interesting interplay between twin boundaries and growth mechanisms in the system Ag/Ru(0001): During growth, a film

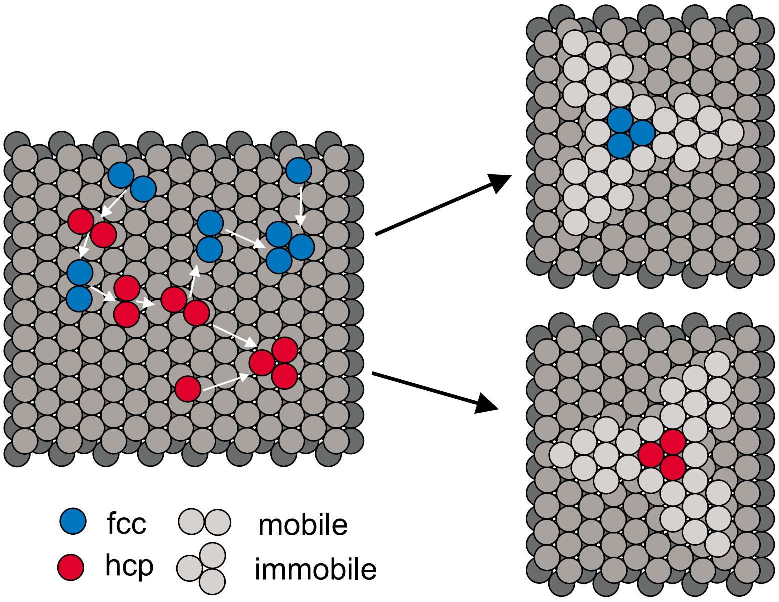

Figure 2.10: Atomistic model of stacking fault nucleation. From Ref. [8].

consisting out of twinned and regular domains separated by twin boundaries was formed. The twins "were essentially stable" and could not be removed by annealing up to the desorption temperature of 450 °C. Ling et al. found that during growth at 180 °C – and opposed to the annealing – twin boundaries in three ML thick areas were able to move as they were overgrown by advancing film steps and reduce the twinned area (Fig. 2.9).

2.4 Homoepitaxy on Ir(111)

The formation of stacking faults in thin film growth is rooted in the nucleation process itself: After deposition, single atoms and small clusters diffuse on the surface. During their random walk over the surface, they occupy different adsorption sites. In the case of fcc(111) surfaces, they occupy alternating regular sites, that continue the fcc stacking sequence, and stacking fault sites.

Once a cluster grows larger than the largest mobile cluster by the attachment of a further adatom, it becomes immobile. As all atoms in a cluster always occupy the same kind of sites, it becomes either a regular or a stacking fault island depending on the kind of sites the cluster rested in upon

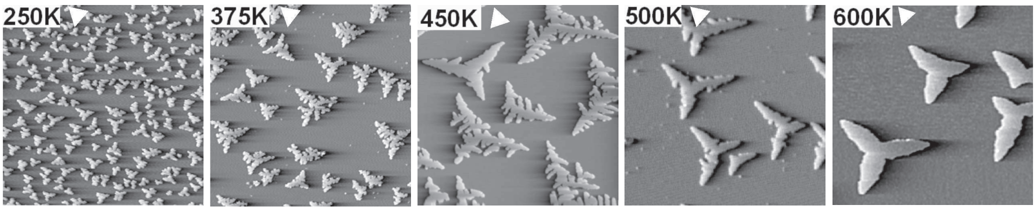

Figure 2.11: STM images after deposition of 0.13 ML Ir on Ir(111) with a deposition rate of 1.3×10^{-2} ML/s (250 K, 375 K, 500 K and 600 K) and 0.22 ML with a deposition rate of 4.9×10^{-3} ML/s (450 K). The orientation of regular islands is indicated by white triangles. Image size 120 nm × 120 nm. Modified from Ref. [9].

immobilization (Fig. 2.10).

For this reason, the probability of forming a stacking fault island is given by the distribution of the largest mobile cluster on regular (fcc) and stacking fault (hcp) sites. The distribution can be described by a Boltzmann-Distribution

$$\left(\frac{P_{hcp}}{P_{fcc}}\right)_i = e^{\Delta F_i / k_B T} \tag{2.7}$$

with the difference of the free energy $\Delta F_i = F_{i,fcc} - F_{i,hcp} = \Delta E_{b,i} - T\Delta S_i$ for the largest mobile cluster of size i on regular and stacking fault sites [8, 43]. Note that the difference of the free energy for the whole cluster is meant, which usually scales with the cluster size. Thus, in general a higher cluster mobility results in a lower stacking fault probability.

As such, nucleation is mainly governed by three parameters: The size of the largest mobile cluster, the distribution of the largest mobile clusters on the two kind of adsorption sites and on the cluster stability. Therefore one would expect stacking fault formation especially in systems with at the same time low stacking fault energy and low mobility.

For this reason, the formation of stacking faults on Ir might be surprising at first glance, as both the values of the stacking fault energy of a whole layer and the activation energy for monomer diffusion – scaled with respect to the different cohesive energies – are close to the values for Pt, where no stacking faults are formed. The formation of stacking faults in this system is due to a special behavior of small Ir clusters: The cluster size of Ir clusters has an important impact on the binding energy on regular or stacking fault sites. Small clusters, i.e. monomers and dimers, prefer stacking fault sites, trimers are found on both kinds of sites with equal probability, and only the

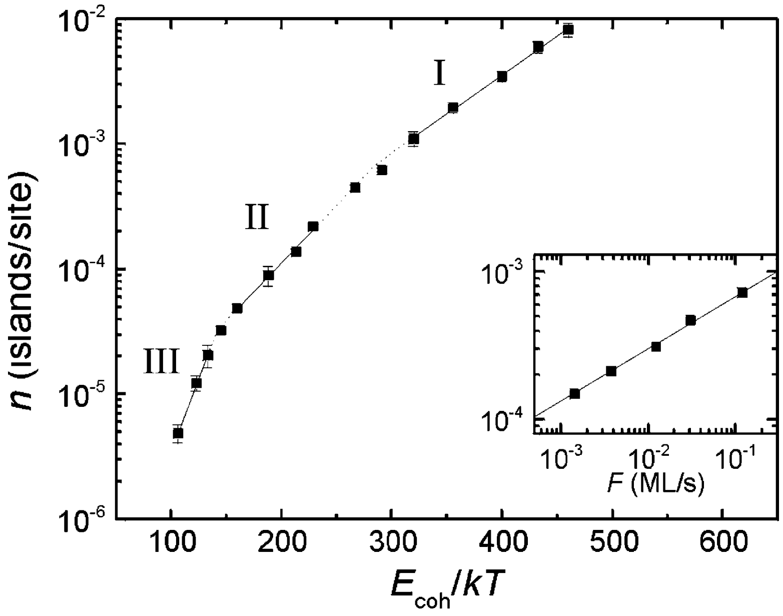

Figure 2.12: Island density n for Ir(111) in an Arrhenius representation. Inset: n vs. deposition rate F for Ir(111) and best linear fit to the data (full line). Modified from Ref. [46].

atoms of larger clusters prefer regular fcc sites [44]. This behavior is based on the smaller effective d-electron density experienced by adatoms and small clusters compared to the bulk. As pointed out by Papadia et al. [45], the d-electron filling of the transition metals is decisive for the stacking sequence: A lower filling results in hcp, a higher filling in fcc stacking.

Fig. 2.11 shows typical STM images of Ir islands grown at different temperatures. Due to the energetic preference, Iridium islands tend to form a triangular shape bound by {111} microfacets, and the shapes of regular islands and stacking fault islands point in different directions. The white triangles in the figure indicate the orientation of a regular island.

Previous works of Busse et al. [8, 46, 9, 44, 43] describe the growth of Ir/Ir(111) in the nucleation regime in great detail. To provide a basis for the following discussion, the main results are summarized here. Using additional field ion microscopy (FIM) data on Ir cluster diffusion from Wang and Ehrlich [47, 48, 7], Busse et al. were able to model the nucleation phase using rate equations and kinetic Monte Carlo simulations (KMC).

Fig. 2.12 shows an Arrhenius plot of the island density at different tem-

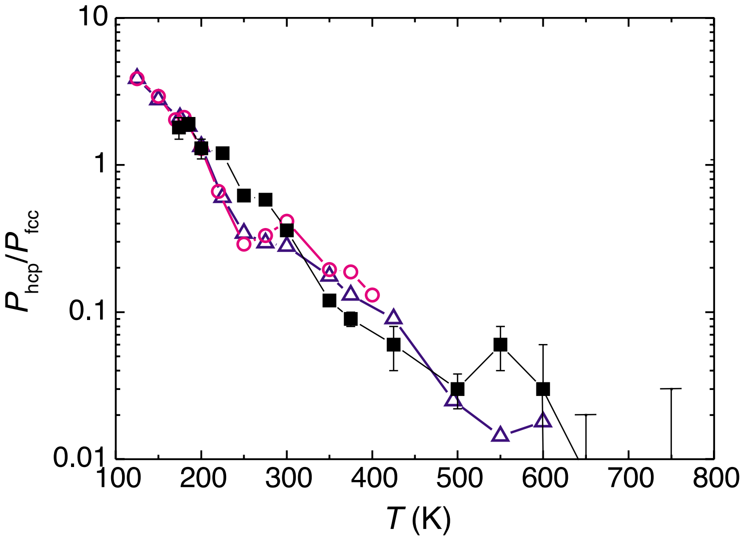

Figure 2.13: Relative stacking fault probability $\frac{P_{hcp}}{P_{fcc}}$ for Ir/Ir(111) in experiment and simulation: Full squares: experiment; open triangles: solution of rate equations; open circles: kinetic Monte Carlo simulation, both using parameters derived by FIM. Modified from Ref. [8].

peratures. Using the previous FIM measurements and this data, the binding and activation energies for diffusion have been calculated. Three different scaling regimes regimes can be distinguished, which are governed by the size of the largest mobile cluster and cluster stability: In the first regime at temperatures below 375 K, only monomers are mobile and dimers are stable clusters. The second regime is at temperatures in between 375 K and 615 K, where dimers are both mobile and stable. For temperatures larger than 615 K, dimers are eventually unstable and only trimers are stable nuclei.

Fig. 2.13 shows the results of the experimental as well as calculated relative stacking fault probability $\frac{P_{hcp}}{P_{fcc}}$ from Busse et al.: For temperatures below 235 K, more than 50% of the islands formed are stacking fault islands, which drops to 37.5% at 275 K and 3% after the onset of dimer dissociation at 600 K.

In the present work, most experiments were performed at 350 K. At 350 K, 11% of the islands formed are stacking fault islands.

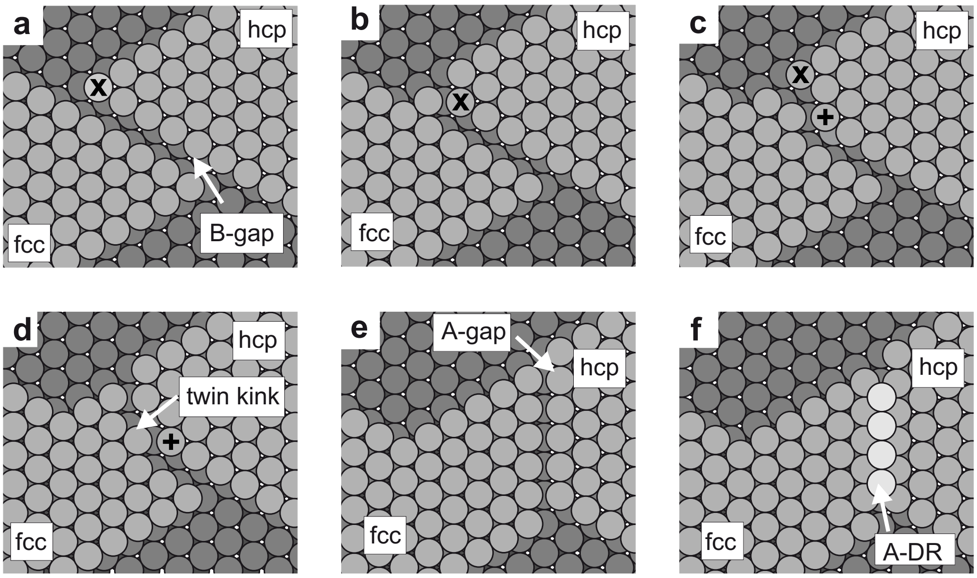

Figure 2.14: Ball model of the self-healing effect. A stacking fault island (hcp) is partly assimilated by a regular island (fcc). See text. Modified from Ref. [49].

2.5 Self-Healing of Stacking Faults in the System Ir/Ir(111)

Iridium has a negative Ehrlich-Schwoebel barrier, and therefore grows in layer-by-layer growth mode. Nucleation in the second layer becomes significant only after the closure of the first monolayer (ML). Upon closure of the first layer, Ir islands of the same stacking coalesce, whereas coalescence for islands of different stacking, i.e. of a regular and a stacking fault island, is not possible: A gap smaller than a lattice spacing remains. This is depicted in the ball model in Fig. 2.14 [49]. Fig. 2.14(a) shows a regular island (fcc) and a stacking fault island (hcp) as well as the remaining gap.

As an abbreviation, {100} and {111} microfacets are also referred to as type A and B. Respectively, the islands are bound by B-steps and a gap with B-steps on both sides is called a B-gap.

The atoms of the stacking fault island occupy slightly energetically inferior sites, but the atoms at the gap may reach the energetically favorable regular

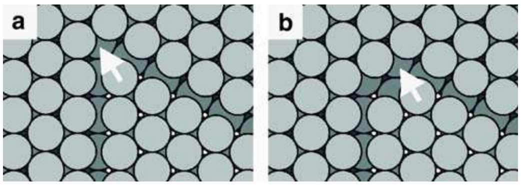

Figure 2.15: Self-healing effect at intersecting A-gaps. Although no self-healing is possible at A-gaps, a new B-gap can be generated at the intersection. From Ref. [49].

sites by detaching from the stacking fault island, overcome the bridge position between two neighboring sites, and attach to the regular island (2.14(a)-(b)). Thus the atoms can reach sites of the same coordination, but lower their potential energy by the stacking fault energy. By a repeated kink-flip process at the twin-kink (Fig. 2.14(c)-(d)), whole rows move from stacking fault to regular sites, and the size of the stacking fault island decreases.

At the same time, the length of the B-gap diminishes and gradually converts to an A-gap. The process comes to an end in situations, when no B-gap is present and the boundary between the remaining islands consist purely of an A-gap as shown in Fig. 2.14(e), where the kink-flip process is not possible for geometric reasons.

In a simple nearest-neighbor bond model, the onset temperature of the self-healing process can be estimated to be 200 K for a tip atom (5 bonds: 2 bonds in the surface plane and 3 in the lower layer), and 240 K for a kink atom (6 bonds) at a B-gap. Continuation of the self-healing process after formation of an A-gap is only possible by processes lowering the coordination of an atom from at least 6 to 5 bonds, a process with an activation temperature of 480 K.

Intersecting A-gaps offer the opportunity for a continuation of the self-healing process: The atom that forms the tip of the remaining stacking fault island can move to the regular area, thereby generating a new, two atom wide B-gap and initiate further self-healing (Fig. 2.15). As this process has an activation temperature of only 200 K, one would expect the self healing at room temperature to be complete.

A-gaps offer energetically favorable fourfold coordinated adsorption sites on top, which are rapidly occupied by a adatoms on continued deposition as shown in 2.14(e). These rows of single atoms decorate the boundary between the areas of different stacking, and hence are called decoration rows (DRs).

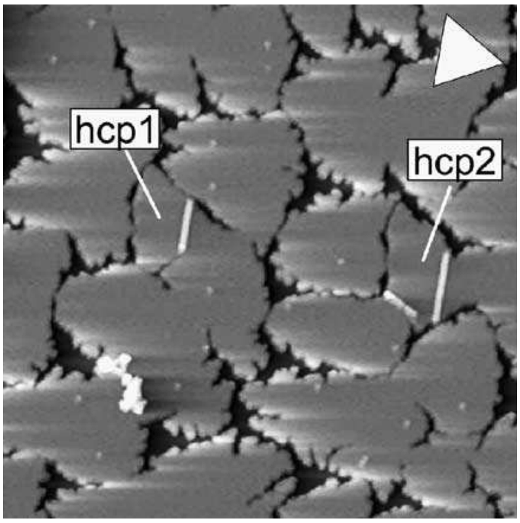

Figure 2.16: STM topograph after deposition of 0.91 ML Ir on Ir(111) at 350 K with 1.6×10^{-2} ML/2. The white lines next to the stacking fault islands marked as "hcp1" and "hcp2" are decoration rows. Image size 79 nm × 79 nm. The orientation of stacking fault islands is indicated by the white triangle. From Ref. [49].

Due to the fourfold coordination, atoms on top of A-gaps are stable up to at least 400 K, as jumping out of the gap requires a change in coordination from at least four to three bonds. Fig. 2.16 shows an STM image of Ir(111) after deposition of 0.91 ML at 350 K with two partially healed stacking fault islands (marked "hcp1" and "hcp2") and decoration rows.

Although mechanisms are possible in which self-healing of areas bound by decoration rows continues and decoration rows move [49], it is quite probable, that the self healing is slowed by the formation of decoration rows and even stopped by certain configurations. After the closure of the first layer, very stable stacking fault areas remain in films grown at 350 K, which are bound by decoration rows.

Within the scope of this work, the effects of these remaining defects on the growth of thin Ir films have been studied with special care, and strategies to promote the growth of defect free films have been developed.

3 Experimental Details and Methods

To study the mechanisms of growth and annealing uninfluenced and in its pure form, special care was taken in all experiments to assure sample cleanness, clean deposition conditions, and a low background pressure, especially during evaporation. All studies presented in this work were performed in ultra high vacuum (UHV).

The scanning tunneling microscopy (STM) and low energy electron diffraction (LEED) experiments presented in this work have been performed in the UHV chambers Tuma III and Athene at the Rheinisch-Westfälische Technische Hochschule Aachen in Aachen, Germany and the Universität zu Köln, Cologne, Germany. The surface X-ray diffraction (SXRD) experiments have been performed at the beamline BM32 of the European Synchrotron Radiation Facility (ESRF) in Grenoble, France.

In the following, the setups, experimental procedures and methods will be described in detail.

3.1 Experimental Setup for the STM and LEED Experiments: UHV Systems Tuma III and Athene

As both Athene and Tuma III are quite similar in design, only Athene will be described in detail while addressing the differences to Tuma III. Both systems differ mainly in the presence of a sample exchange and a reflection high energy electron diffraction (RHEED) system, which are exclusive to Athene, and little in the geometric arrangements.

Fig. 3.1 shows the UHV chamber Athene. Both systems are built around a manipulator, on which the sample in its sample holder, the sample heating, the cryostat and a Faraday cup for ion flux measurements are mounted. By movement of the manipulator, the sample is positioned in front of the

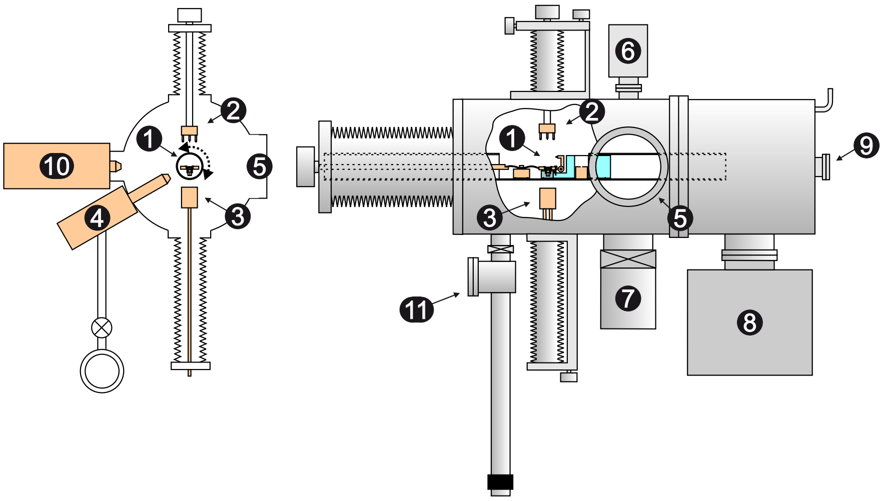

Figure 3.1: Sketch of vacuum chamber Athene: (1) Ir(111) sample mounted onto the manipulator, (2) STM, (3) evaporator, (4) ion gun, (5) LEED, (6) mass spectrometer, (7) turbomolecular pump, (8) ion pump, (9) cold trap and titanium sublimator, (10) RHEED, (11) sample transfer system. Modified from Ref. [50].

different instruments. Differentially pumped ion guns are used for sample cleaning. In Athene, the ion gun is mounted in plane with the evaporator with an angle of 60° in between the two devices, making ion beam assisted deposition (IBAD) possible. Ir is evaporated from a current heated wire. In order to minimize unnecessary heating of the inner part of the cell, the filament is shielded by a water cooled copper casing and mounted on a water cooled copper block. For analysis, the chambers are equipped with a home built, magnetically stabilized, inverted beetle type STM [51], a commercially available rearview camera LEED system, and a quadrupole mass spectrometer. A RHEED system is available at Athene. Two turbomolecular pumps (with primary pumps) are connected to the chamber and to the ion source, respectively. An ion pump ensures vibration-free pumping during STM measurements. Additionally, a cold trap and a titanium sublimator are used to support pumping especially during deposition.

The achieved background pressures are 6×10^{-11} mbar and 3×10^{-11} mbar for Athene and Tuma III, respectively. In both systems, the pressure during deposition is kept well below 1×10^{-10} mbar. During IBAD, the pressure in the main chamber is raised by the noble gas atoms used in the ion gun, but other species in the background pressure are hardly affected compared to deposition only.

The STM topographs in this work are presented in either greyscale or differentiated mode. Differentiated topographs appear as if illuminated from the left and allow better visual inspection of images with high dynamic range, e.g. images of rough surfaces.

3.2 Experimental Setup for the SXRD Experiments at the Beamline BM32 of the ESRF

The surface X-ray diffraction (SXRD) experiments have been performed at the beamline BM32 of the European Synchrotron Radiation Facility (ESRF) in a UHV system with a base pressure of 3×10^{-10} mbar. Fig. 3.2 shows the experimental setup.

The UHV chamber was equipped with the same evaporator as in Athene and Tuma III, an ion gun for sample preparation, and a RHEED system for pre-calibration of the evaporator without the need of the synchrotron radiation[1]. The sample was mounted on the goniometric head as shown in the bottom left image of Fig. 3.2, which is installed in the UHV system from the rear. The sample surface is aligned vertically with respect to the ground and parallel to the large flange on the right hands side in the upper image of Fig. 3.2. The X-ray beam enters and exits the UHV chamber through beryllium windows at the side. Measurements are taken using the different detectors mounted on the detector arm. The geometry of the diffractometer and the labeling of the axis used is shown schematically in Fig. 3.3. A detailed description of the system and the 4-circle diffractometer can be found in Ref. [52, 53].

For the measurements, a monochromatic 18 keV photon beam incident under an angle of $0.27° \pm 0.15°$ with respect to the surface was used. The corresponding $1/e$ X-ray penetration depth for Ir is 51 Å (23 ML) [54].

---

[1] The evaporation rate was measured in-situ during evaporation using X-ray intensity oscillations at an Anti-Bragg position.

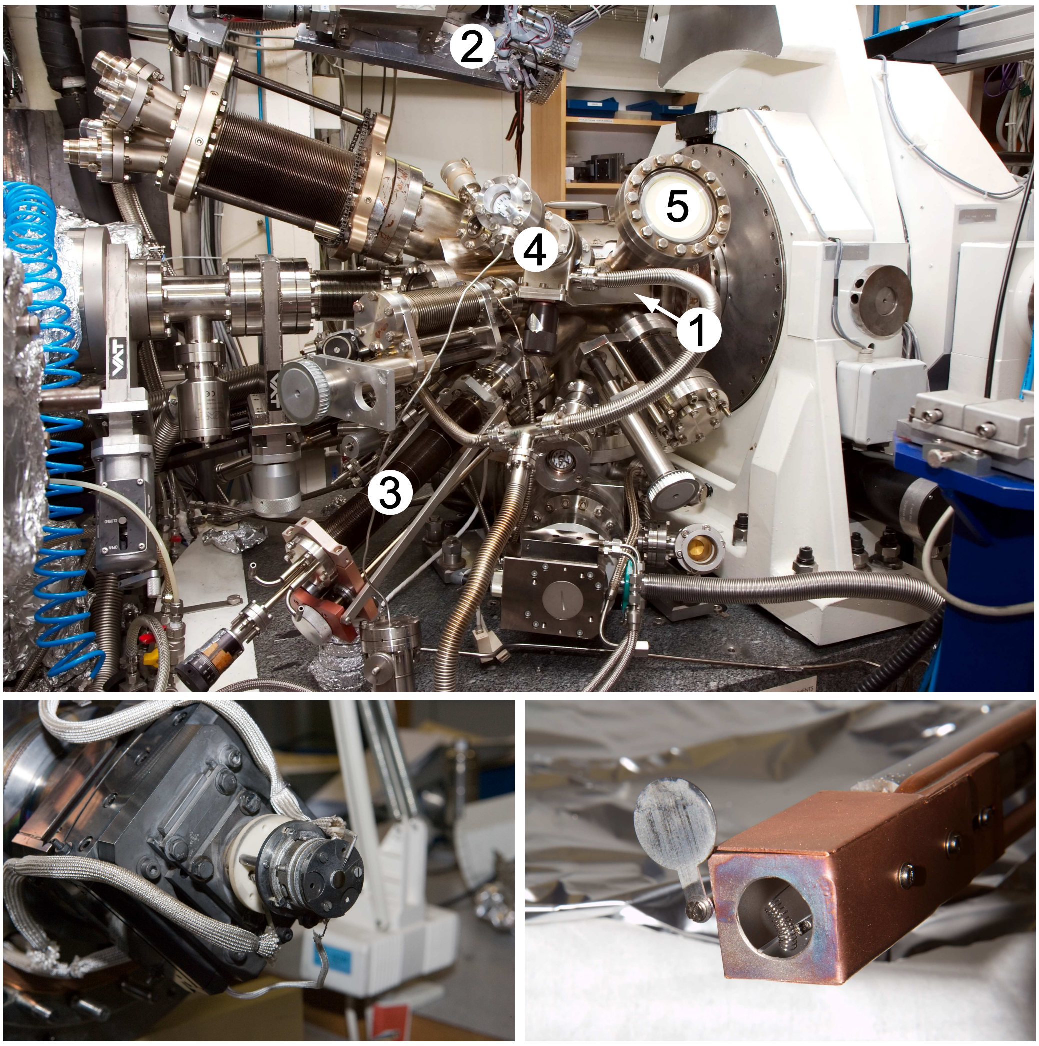

Figure 3.2: (top) Vacuum chamber at the beamline BM32 of the ESRF: (1) beryllium window for the incoming beam, (2) detector arm, (3) evaporator, (4) ion gun, (5) RHEED screen. (bottom left) Sample mounting. (bottom right) Evaporator.

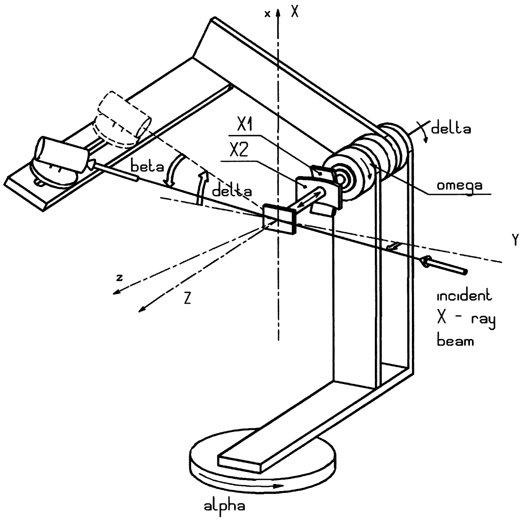

Figure 3.3: Scheme of the main movements of the diffractometer. From Ref. [52].

3.3 Experimental Procedure

The experimental procedure was identical in all experiments:

The sample was cleaned by annealing slowly to 1120 K and ion bombardment for 3 min at room temperature, followed by repeated cycles of sputtering with 1.5 keV Xe^+ or Ar^+ ions at 1100 K and annealing to 1600 K. Ion bombardment was repeated until an amount was sputtered, that exceeded the amount deposited in the last experiment by at least 20 ML, where 1 ML (monolayer) is the surface atomic density of Ir(111), or sample cleanness was confirmed by other means. After sample cleaning, the cooling trap was filled and the titanium sublimator was used once. Prior to deposition, the sample was flashed to a temperature ensuring desorption of all species that might have adsorbed from the background gas.

Iridium was deposited from a current heated Ir wire of 0.25 mm with a purity of 99.9% with a standard deposition rate of 1.3×10^{-2} ML/s.

3.4 SXRD

Matching typical interatomic distances in solids in wavelength, X-rays allow one structural investigations by diffraction experiments. X-ray diffraction

(XRD) is a non-destructive technique, and due to the weak interaction of X-rays with matter, a single scattering approach is often sufficient to analyze the experimental data and makes the data interpretation straight forward. XRD has become one of the standard techniques in modern solid state physics and is widely used.

Standard XRD is only suited for investigations of the bulk and not the surface. The scattered intensity of a typical surface is more than five orders of magnitude lower than from a bulk. For this reason, surface sensitivity does not only require very intense X-ray sources as e.g. synchrotrons, but limiting sensitivity to the surface must be achieved by further means.

An optimum of surface sensitivity can be achieved by using grazing incidence when the angle of incidence is equal to the critical angle of total reflection [55]. The beam is then totally reflected and strongly damped into the crystal surface as described by the Fresnel equations, thereby limiting the penetrations depth to a few nanometers. Interference effects of the incoming and reflected wave further enhance the intensity by up to a factor of two. The limitation of penetration depth leads to a restriction in periodicity in one dimension and to a two dimensional nature. This gives rise to rods of diffracted intensity instead of points, so called crystal truncation rods (CTRs) [56, 57, 58], which contain surface sensitive information.

3.4.1 Penetration Depth

The index of refraction for a given material is

$$n = 1 - \frac{e^2}{2\pi m_e c^2} \frac{\lambda^2}{V} F(0) \tag{3.1}$$

[55], where λ is the wavelength of the X-rays, c the speed of light, m_e and e the electron mass and charge, V the unit cell volume, and $F(0)$ the structure factor calculated at zero momentum transfer. To include absorption, the dispersion corrections f' and f'' must be included in the structure factor

$$F(0) = \sum_j \left(f_{0,j} + f'_j + i f''_j \right) , \tag{3.2}$$

where j denotes the atoms and $f_{0,j}$ the atomic charges in the unit cell. Introducing the linear absorption coefficient μ_a, this leads to

$$\begin{aligned} n &= 1-\delta-i\beta && (3.3)\\ \delta &= \frac{e^2}{2\pi m_e c^2}\frac{\lambda^2}{V}\sum_j\left(f_{0,j}+f_j'\right) && (3.4)\\ \beta &= \frac{e^2}{2\pi m_e c^2}\frac{\lambda^2}{V}\sum_j f_j'' = \frac{\mu_a}{4\pi}\lambda\,. && (3.5)\end{aligned}$$

Using these definitions, the critical angle for total reflection α_c can be expressed as

$$\delta = \frac{1}{2}\sin^2\alpha_c\,, \tag{3.6}$$

which leads for small angles to

$$\alpha_c \approx \sqrt{2\delta}\,. \tag{3.7}$$

The momentum transfer perpendicular to the surface q_z in vacuum is given by

$$\begin{aligned} q_z &= k_z^f - k_z^i && (3.8)\\ &= (2\pi/\lambda)(\sin\alpha_f+\sin\alpha_i)\,, && (3.9)\end{aligned}$$

where α_i and α_f are the angles between the incident beam and the surface and the diffracted beam and the surface, respectively. Since the index of refraction is complex, this quantity becomes within the sample

$$\begin{aligned} q_z^{'} &= k_z^{f'} - k_z^{i'} && (3.10)\\ &= (2\pi/\lambda)\left(\sqrt{\sin^2\alpha_f-2\delta-2i\beta}+\sqrt{\sin^2\alpha_i-2\delta-2i\beta}\right) && (3.11)\end{aligned}$$

[59] by application of Snell´s law. Primes denote quantities within the sample. The depth where the scattered intensity is reduced to $1/e$ is called the scattering, attenuation or penetration depth Λ, which equals

$$\Lambda = \frac{1}{|Im(q_z)|}\,. \tag{3.12}$$

Using the above, the penetration depth calculates to

$$\Lambda^{-1} = \sqrt{2}k\sqrt{(2\delta-\sin^2\alpha_{i,f})+\sqrt{(\sin^2\alpha_{i,f}-2\delta)^2+4\beta^2}}\,. \tag{3.13}$$

Fig. 3.4 shows the calculated X-ray penetration length for an 18 keV beam on Ir and different angles [54].

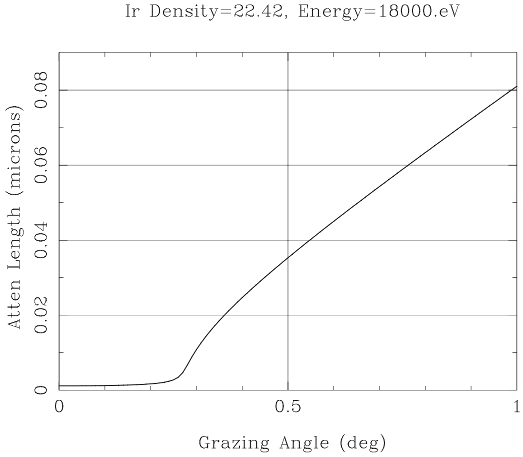

Figure 3.4: 1/e X-ray attenuation length for a beam energy of 18 keV on Ir. Calculated using Ref. [54].

3.4.2 Basics of Surface X-ray Scattering

The scattering of X-rays by a free electron is given by the Thompson scattering formula. The scattered field $\boldsymbol{E}_e$ has the amplitude

$$E_e = E_0 \frac{e^2}{m_e c^2 R} \sqrt{P} \,, \tag{3.14}$$

where E_0 is the amplitude of the incoming wave and R is the distance from the electron. The polarization factor P describes the dependence of E_e on the polarization of the incoming wave. $P = 1$ if E_0 is normal to the scattering plane spanned by $\boldsymbol{k}^i$ and $\boldsymbol{k}^f$, and $P = \cos^2 2\theta$, with 2θ being the angle between $\boldsymbol{k}^i$ and $\boldsymbol{k}^f$, when E_0 is in the scattering plane. Scattering from a free atom is then given by summing up the contributions of each electron:

$$E_a = E_0 \frac{e^2}{m_e c^2 R} \sqrt{P} \int \rho_a(\boldsymbol{r}) e^{i\boldsymbol{q}\cdot\boldsymbol{r}} dV \,, \tag{3.15}$$

where $\boldsymbol{q} = \boldsymbol{k}^f - \boldsymbol{k}^i$ and $\rho_a(\boldsymbol{r})$ the atomic electron density. The form factor f_0 is defined by

$$f_0 = \int \rho_a(\boldsymbol{r}) e^{i\boldsymbol{q}\cdot\boldsymbol{r}} dV \,. \tag{3.16}$$

If the incoming photons have an energy close to the absorption edge, the electron cannot be considered as free and resonance effects have to be included. This is done by adding dispersion corrections to the form factor.

Taking the dispersion corrections f' and f'' into account, the form factor is modified to

$$f = f_0 + f' + if'' . \tag{3.17}$$

In standard X-ray diffraction, the positions of atoms in a crystal lattice are described by multiples of the lattice vectors $\boldsymbol{a}_1$, $\boldsymbol{a}_2$ and $\boldsymbol{a}_3$ and the additional vectors $\boldsymbol{r}_j$, which define the positions of the atoms in the unit cell, as

$$\boldsymbol{R} = n_1\boldsymbol{a}_1 + n_2\boldsymbol{a}_2 + n_3\boldsymbol{a}_3 + \boldsymbol{r}_j . \tag{3.18}$$

The scattered wave of the crystal has then the amplitude E_c :

$$\begin{aligned}
E_c &= E_0 \frac{e^2}{m_e c^2 R} \sqrt{P} \sum_R f(\boldsymbol{q}) e^{i\boldsymbol{q}\cdot\boldsymbol{R}} && (3.19)\\
&= E_0 \frac{e^2}{m_e c^2 R} \sqrt{P} F(\boldsymbol{q}) \sum_{n_1=0}^{N_1-1} \sum_{n_2=0}^{N_2-1} \sum_{n_3=0}^{N_3-1} e^{i\boldsymbol{q}\cdot(n_1\boldsymbol{a}_1+n_2\boldsymbol{a}_2+n_3\boldsymbol{a}_3)} && (3.20)\\
F(\boldsymbol{q}) &= \sum_j f(\boldsymbol{q}) e^{i\boldsymbol{q}\cdot\boldsymbol{r}_j} . && (3.21)
\end{aligned}$$

$F(\boldsymbol{q})$ is called the structure factor. Thermal vibrations of the atoms are taken into account by adding the Debye-Waller factor

$$F(\boldsymbol{q}) = \sum_j f(\boldsymbol{q}) \exp\left(\frac{-B_j q^2}{16\pi^2}\right) e^{i\boldsymbol{q}\cdot\boldsymbol{r}_j} , \tag{3.22}$$

where B_j is the so called B-factor. The peak intensity for a fulfilled Laue condition is then [55]

$$I^{peak} = I_0 \frac{e^4}{m_e^2 c^4 R^2} P N_1^2 N_2^2 N_3^2 |F(\boldsymbol{q})|^2 . \tag{3.23}$$

In case of SXRD, the penetration depth is limited and the periodicity is reduced to two dimensions:

$$\boldsymbol{R} = n_1\boldsymbol{a}_1 + n_2\boldsymbol{a}_2 + \boldsymbol{r}_j . \tag{3.24}$$

Although the periodicity is reduced, layers in different depths still contribute to the scattered intensity. For this reason, the unit cell for the calculation of structure factors is infinite in the direction normal to the surface and different layers are weighted with respect to the depth. The exponential decay is expressed using the linear absorption coefficient μ_a.

Be $\boldsymbol{r}_j$ the position of an atom in the jth layer. Following the same approach as for the XRD case, the amplitude and the peak intensity of the scattered wave are [55]:

$$\begin{aligned}
E_c &= E_0 \frac{e^2}{m_e c^2 R} \sqrt{P} \sum_{n_1,n_2,j} f(\boldsymbol{q}) e^{i\boldsymbol{q}\cdot\boldsymbol{R}} e^{-j\mu_a} && (3.25)\\
&= E_0 \frac{e^2}{m_e c^2 R} \sqrt{P} F(\boldsymbol{q}) \sum_{n_1=0}^{N_1-1} \sum_{n_2=0}^{N_2-1} e^{i\boldsymbol{q}\cdot(n_1\boldsymbol{a}_1+n_2\boldsymbol{a}_2)} && (3.26)\\
F(\boldsymbol{q}) &= \sum_j f(\boldsymbol{q}) e^{i\boldsymbol{q}\cdot\boldsymbol{r}_j} e^{-j\mu_a} && (3.27)\\
I^{peak} &= I_0 \frac{e^4}{m_e^2 c^4 R^2} P N_1^2 N_2^2 |F(\boldsymbol{q})|^2 \,. && (3.28)
\end{aligned}$$

Layers in a crystal are not randomly distributed, but shifted over each other by a constant translation vector $\boldsymbol{r}_{shift}$. Assuming a one atomic basis, $\boldsymbol{r}_j$ can be expressed by $\boldsymbol{r}_j = j\boldsymbol{r}_{shift}$:

$$\boldsymbol{R} = n_1\boldsymbol{a}_1 + n_2\boldsymbol{a}_2 + j\boldsymbol{r}_{shift} \,. \tag{3.29}$$

The structure factor then calculates to

$$\begin{aligned}
F(\boldsymbol{q}) &= \sum_{j=-\infty}^{0} f(\boldsymbol{q}) \exp\left(ij\boldsymbol{q}\cdot\boldsymbol{r}_{shift}\right) \exp\left(j\mu_a\right) && (3.30)\\
&= \frac{f(\boldsymbol{q})}{1-\exp\left(-i\boldsymbol{q}\cdot\boldsymbol{r}_{shift}\right)\exp\left(-\mu_a\right)} \,. && (3.31)
\end{aligned}$$

Adding the Debye-Weller factor, the structure factor is

$$F(\boldsymbol{q}) = \exp\left(\frac{-Bq^2}{16\pi^2}\right) \frac{f(\boldsymbol{q})}{1-\exp\left(-i\boldsymbol{q}\cdot\boldsymbol{r}_{shift}\right)\exp\left(-\mu_a\right)} \,. \tag{3.32}$$

3.4.3 Application to Ir(111)

Being an fcc crystal, Ir has a stacking sequence of ABCABC in [111] direction. Each layer is shifted towards the previous by a constant vector. To account for the stacking sequence, a hexagonal unit cell is employed for the description of the crystal truncation rods.

In the present work, the upper index *hex* is used to denote the hexagonal system, whereas no upper index refers to the standard cubic system. The hexagonal system is used for the description of CTRs only. For the general description of planes and directions, the standard cubic system is maintained.

The hexagonal lattice vectors $\{\boldsymbol{a}_i^{hex}\}$ are expressed in terms of the conventional cubic lattice vectors $\{\boldsymbol{a}_i^{cubic}\}$ by

$$\boldsymbol{a}_1^{hex} = \tfrac{1}{2}\ [10\bar{1}]^{cubic} \tag{3.33}$$

$$\boldsymbol{a}_2^{hex} = \tfrac{1}{2}\ [\bar{1}10]^{cubic} \tag{3.34}$$

$$\boldsymbol{a}_3^{hex} = [111]^{cubic}, \tag{3.35}$$

i.e. the two first vectors point into the direction of nearest neighbors in the surface plane and the third is normal to the surface. In the respective reciprocal coordinates the CTRs are described by the h and k Miller indices while l is the perpendicular momentum transfer. The corresponding reciprocal lattice vectors $\{\boldsymbol{b}_i^{hex}\}$ are defined by

$$\boldsymbol{a}_i^{hex} \cdot \boldsymbol{b}_j^{hex} = 2\pi\delta_{ij}\,. \tag{3.36}$$

The momentum transfer $\boldsymbol{q}$ is then denoted in reciprocal space as

$$\boldsymbol{q} = h\boldsymbol{b}_1^{hex} + k\boldsymbol{b}_2^{hex} + l\boldsymbol{b}_3^{hex}\,. \tag{3.37}$$

Using the hexagonal coordinate system, the shift between layers is

$$\boldsymbol{r}_{shift} = \frac{2}{3}a_1^{hex} + \frac{1}{3}a_2^{hex} + \frac{1}{3}a_3^{hex}\,, \tag{3.38}$$

and the structure factor calculates to

$$F(\boldsymbol{q}) \propto \frac{1}{1 - \exp\left(-i\boldsymbol{q}\cdot\boldsymbol{r}_{shift}\right)\exp\left(-\mu_a\right)} \tag{3.39}$$

[60] with

$$\boldsymbol{q}\cdot\boldsymbol{r}_{shift} = \frac{2}{3}h + \frac{1}{3}k + \frac{1}{3}l\,. \tag{3.40}$$

Intensity peaks can be expected for positions on the CTRs where

$$\exp\left(\boldsymbol{q}\cdot\boldsymbol{r}_{shift}\right) = 1\,. \tag{3.41}$$

Fig. 3.5 shows exemplarily maps of the expected intensity peaks on the $(H0)$, $(0K)$ and (HH) CTRs.

Positions exactly in between two intensity maxima on a CTR are very sensitive to the growth mode: At these so called anti-Bragg positions, the scattered intensity from an island is out of phase with the scattered intensity from the bulk, and growth oscillations can be observed for layer-by-layer growth mode.

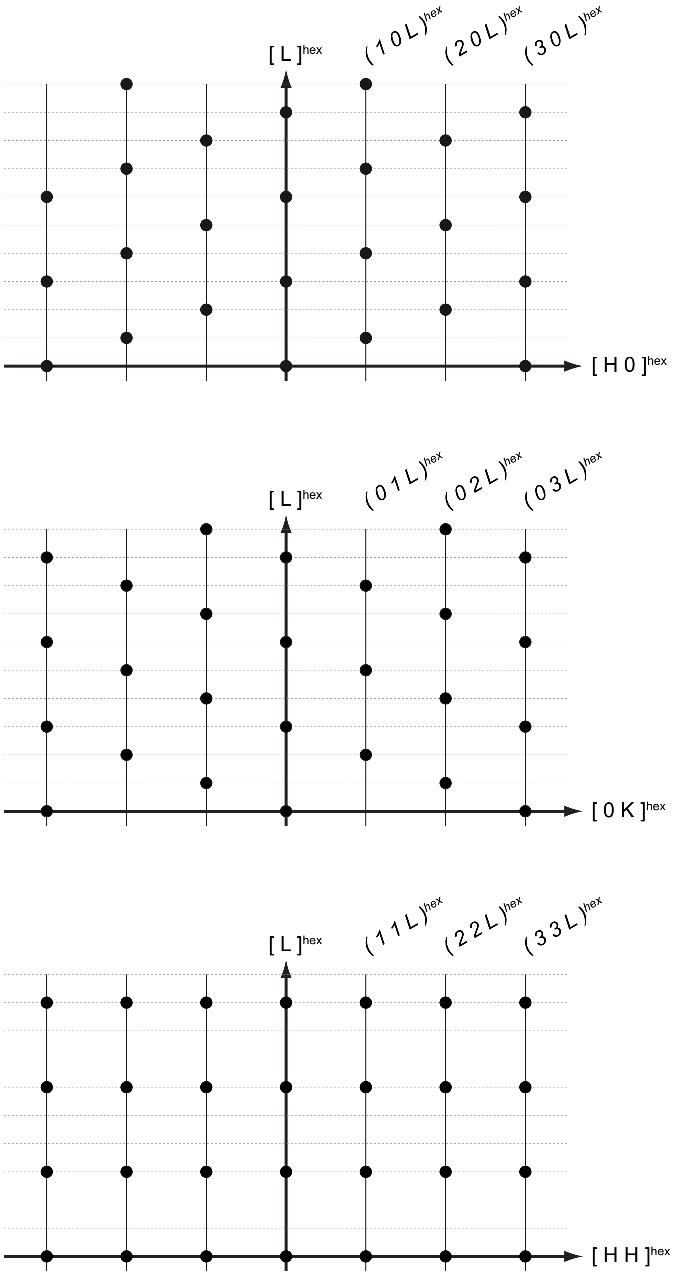
[L]hex
(1 0 L)hex
(2 0 L)hex
(3 0 L)hex
[H 0]hex
[L]hex
(0 1 L)hex
(0 2 L)hex
(0 3 L)hex
[0 K]hex
[L]hex
(1 1 L)hex
(2 2 L)hex
(3 3 L)hex
[H H]hex

Figure 3.5: Expected peak intensities on CTRs for fcc crystals using the hexagonal coordinate system explained in the text.

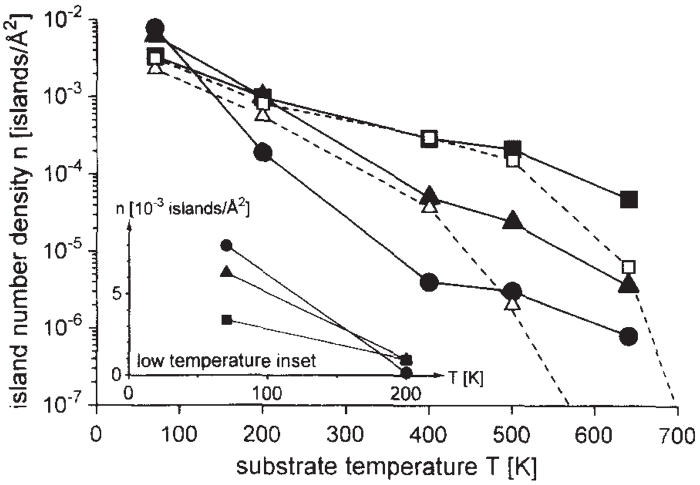

Figure 3.6: Plot of the island number densities n versus the temperature T after conventional vapor phase deposition (solid circles), after IBAD with $R = 0.1$ for 400 eV Ar^+ (solid triangles) and for 4 keV Ar^+ (solid squares), and after ion bombardment alone with 400 eV Ar^+ (open triangles) and with 4 keV Ar^+ (open squares), with an ion fluence of 3×10^{17} ions/m^2 in all cases. From Ref. [64].

3.5 Ion Beam Assisted Deposition

Ion beam assisted deposition (IBAD) is a commonly used technique in thin film deposition to efficiently manipulate film properties. IBAD has already proved in a variety of instances to be an efficient tool to manipulate film properties. IBAD may induce textured growth on non-epitaxial substrates [61, 62], improve the sharpness of interfaces of Cr/Sc metal multilayers for X-ray optics [63], or reduce the roughness of films in metal homoepitaxy [64].

Multiple observations have been made for the effects of IBAD on the nucleation phase. Most commonly, a change in the island number densities was observed for films grown using IBAD. The change was attributed to surface point defect creation [65], to the removal of adatoms from islands [66], to adatom [67] and surface vacancy island creation [68], to ion bombardment enhanced mobility [69] or to preferential sputtering [70]. Using IBAD, the nucleation of three dimensional islands could be suppressed during growth of GaAs on Si(100) [66].

With respect to these different results, the effects of IBAD on the atomic processes on the nucleation phase and during the growth of the first layers of Pt/Pt(111) have been studied by Esch et al. [64]. Due to the similarity of Ir to Pt, a similar behavior can be expected. For this reason, the main results for Pt shall be summarized here.

The island number densities for Pt/Pt(111) deposited using conventional physical vapor deposition, IBAD with 400 eV Ar^+ and an ion to atom arrival ratio of $R = 0.1$ and IBAD with 4 keV Ar^+ and $R = 0.1$ are shown in Fig. 3.6. For temperatures below 200 K, adatoms are already immobile on the surface. Adatoms created by ion bombardment could be expected to form stable nuclei and increase the island number density. Opposed to this assumption, the island number densities of the IBAD experiments are decreased compared to the PVD experiments. This can be attributed to the simultaneous energy deposition by the ion bombardment. An impinging ion locally heats an area of some nanometers and thus allows residing adatoms to move. Agglomeration to clusters or recombination with vacancies then decreases the island number density. For temperatures above 200 K, the island number density is increased in the IBAD experiments. The increased temperature reduces the influence of the local heating, as small clusters are already mobile, while at the same time it increases the effect of the adatom clusters created by ion bombardment. The increased density of adatom clusters on the surface in the IBAD experiment leads to the nucleation of an increased number of islands, and thus an increase in the island number density. The recombination of adatoms with vacancies does not play an important role on the timescale relevant for nucleation events. It was shown by ion bombardment experiments without deposition, that the increase in island number density is mostly linked to the creation of adatom clusters by ion bombardment. The density of adatom clusters created by ion bombardment is close to the island number density in the respective IBAD experiments, but by a factor of 5 to 60 higher than in PVD. For temperatures above 400 K, cluster dissociation becomes important and the island number density drops. In the absence of vacancies, atoms exchange between clusters and larger clusters grow at the expense of smaller ones and thereby decrease the island number densities moderately. In contrast, for the ion bombarded surface the adatoms recombine with vacancies and the island number density drops significantly as seen in Fig. 3.6.

To summarize, the important effects are local heating and adatom creation by ion bombardment. As discussed in the previous chapter, the formation of stacking faults is strongly depending on size of the largest mobile cluster. Local heating by ion bombardment might increase cluster mobility and thereby influence stacking fault formation, as well as promote self-healing of stacking fault islands.

4 Evolution of Stacking Faults and Twinned Areas in Thin Films

In this chapter, the results of the study on the evolution of stacking faults and twinned areas in thin films are presented. Scanning tunneling microscopy and low energy electron diffraction were used to investigate the growth of partly twinned Ir thin films on Ir(111). A transition from the expected layer-by-layer to a defect dominated growth mode with a fixed lateral length scale and increasing roughness is observed. During growth, the majority of the film is stably transformed to twinned stacking. This transition is initiated by the energetic avoidance of the formation of intrinsic stacking faults compared to two independent twin faults. The atomistic details of the defect kinetics are outlined.

The results presented in this chapter have been also published as separate publications in *Physical Review Letters* [71] and *Physical Review B* [72].

4.1 Growth at 350 K

Thin films of Ir/Ir(111) were grown in the UHV chamber Tuma III as described in chapter 3 with a standard deposition rate of 1.3×10^{-2} ML/s and investigated by STM and LEED.

Figure 4.1 shows snapshots of the surface morphological evolution up to 5 ML deposited. After deposition of an amount of $\Theta = 1.05$ ML (Fig. 4.1(c)) the first layer is almost perfectly closed as in layer-by-layer growth. Indeed, layer-by-layer growth is expected for homoepitaxy on Ir(111) due to the absence of a step edge barrier [37]. Even after 5 ML deposited (compare Fig. 4.1(f)) the fifth layer is almost perfectly closed with only small areas of grooves and islands and a very small area fraction (a few 10^{-3}) on top of islands. From the images an initial layer-by-layer growth of Ir on Ir(111) is obvious.

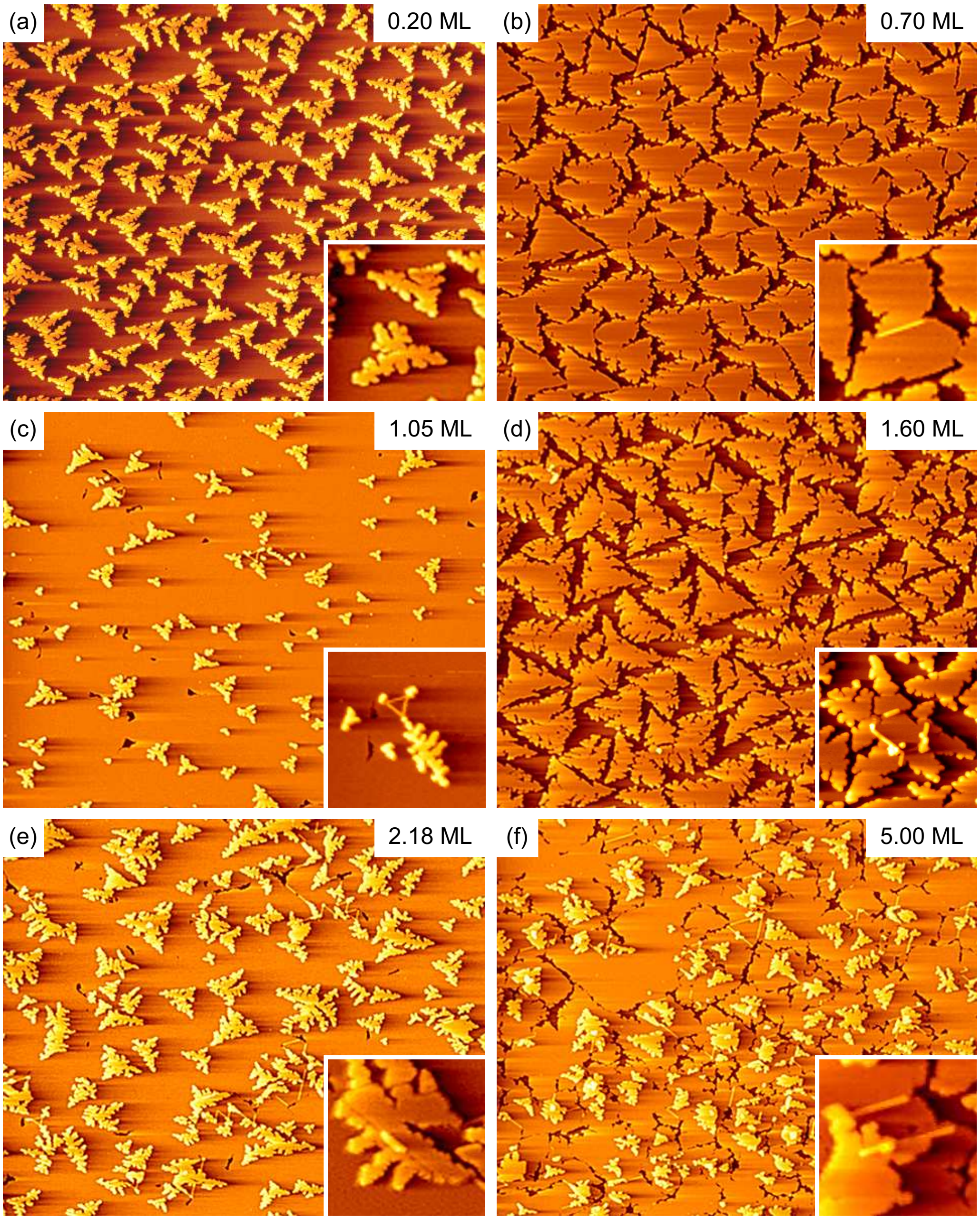
(a)
0.20 ML
(b)
0.70 ML
(c)
1.05 ML
(d)
1.60 ML
(e)
2.18 ML
(f)
5.00 ML

Figure 4.1: STM topographs after deposition of (a) 0.20 ML, (b) 0.70 ML, (c) 1.05 ML, (d) 1.60 ML (e) 2.18 ML and (f) 5.00 ML of Ir on Ir(111) at 350 K. The image size is always 240 nm × 198 nm. Insets: Characteristic morphological features and defects in magnified view. See text.

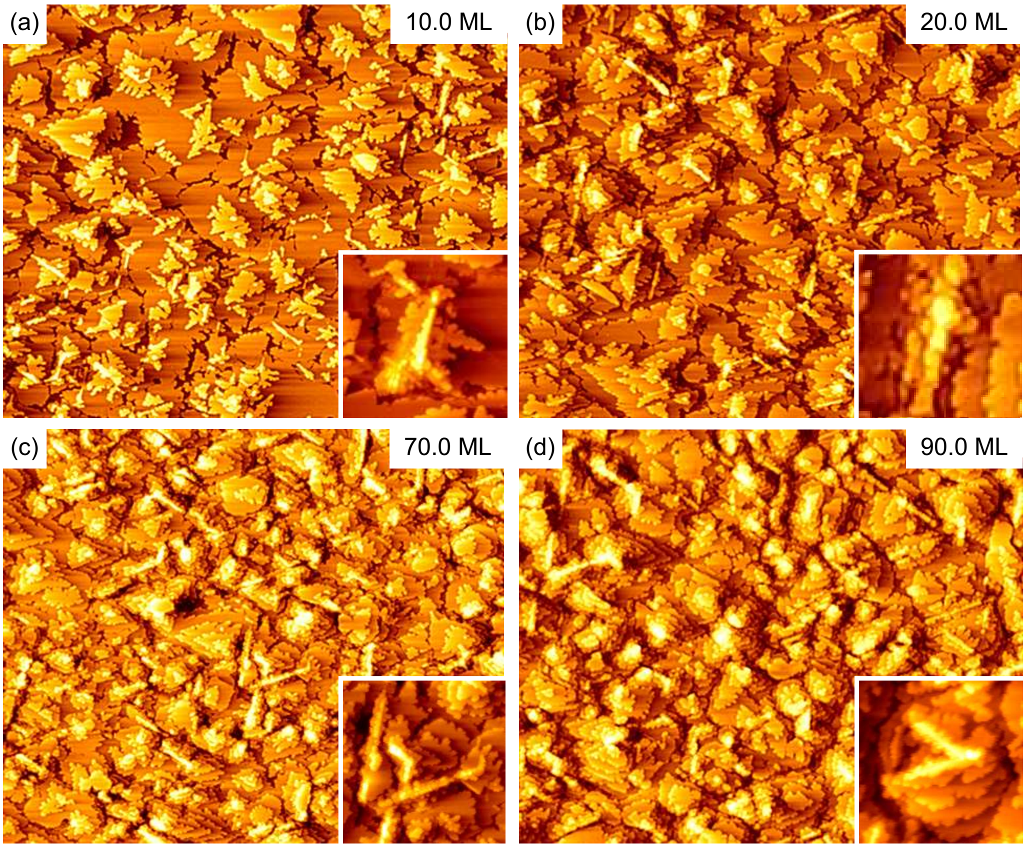

Figure 4.2: STM topographs after deposition of (a) 10 ML, (b) 20 ML, (c) 70 ML and (d) 90 ML of Ir on Ir(111) at 350 K. Image size is 240 nm × 198 nm. Insets: Characteristic morphological features and defects in magnified view. See text.

Shortly after nucleation the adatom islands display threefold symmetric fractal-dendritic island shapes (compare Figs. 4.1(a), (c), (e) and (f)), which become fatter and more compact when the islands approach coalescence (compare Figs. 4.1(b) and (d)). The dendritic island shapes can be well reproduced by kinetic Monte Carlo simulations using atomistic input parameters based on field ion microscopy measurements [9]. The more compact island shapes prior to coalescence are due to enhanced supply of atoms descending from the islands filling preferentially the island fjords.

However, on Ir(111) small mobile Ir-clusters (dimers, trimers, etc.) occupy also faulted surface sites [7], which give rise to the homogeneous nucleation

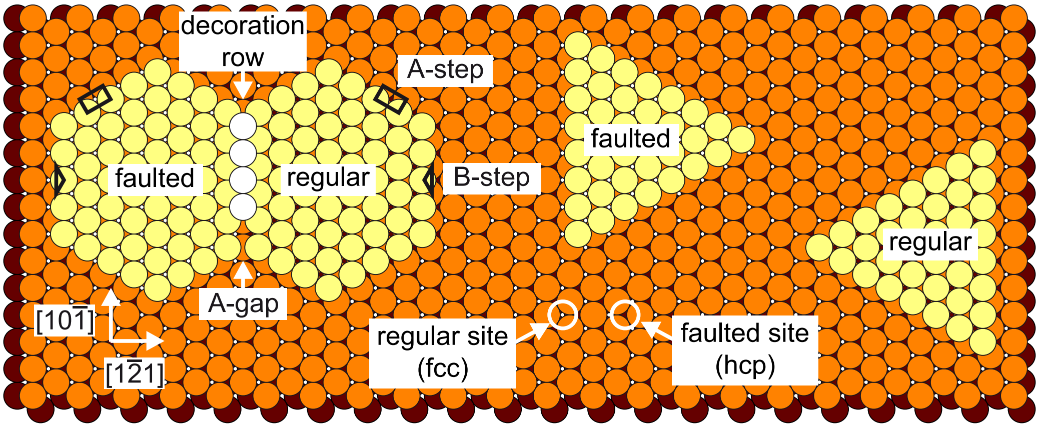

Figure 4.3: Ball model. The Ir(111) surface displays regular (fcc-) and faulted (hcp-) threefold coordinated adsorption sites. Dense packed steps of Ir(111) are {100}-microfacetted (A-step) or {111}-mirofacetted (B-step), indicated in the ball model by a square or triangle in the step. The preference for B-steps in growth causes regular islands and faulted islands to appear rotated by 180°. Regular areas and faulted areas in close encounter may form A-gaps, two A-steps separated by a narrow gap. A-gaps display stable fourfold coordinated adsorption sites. They adsorb Ir atoms to form decoration rows, rows of atoms along ⟨110⟩-directions.

of fault islands [8]. For all topographs in Fig. 4.1 not one, but two different roughly threefold symmetric island shapes are visible, which are rotated by 180° with respect to each other (compare inset of Fig. 4.1(a)). The majority islands with one triangle tip pointing downwards are regular islands while the minority species with one triangle tip pointing upwards are stacking faults islands as will be discussed below.

Although at the beginning of deposition ≈ 11% of all islands formed were fault islands (compare Fig. 1 of [49]), most of the faulted island area is transformed to regular stacking upon close encounter of regular and faulted islands during layer completion through an atom-by-atom transfer from the faulted to the regular phase [49]. This self-healing mechanism comes only to rest if intersecting straight lines of fourfold-coordinated adsorption sites along ⟨110⟩-directions are formed (named A-gaps, see Fig. 4.3), which separate regular and faulted stacking. Upon subsequent deposition atoms are stably adsorbed into these fourfold-coordinated gap-sites, thereby forming strings of monoatomic width (named thin decoration rows, tDR's).The insets of Figs.

4.1(b)-(f) all highlight characteristic defect structures in the film. These lines of atoms oriented along the dense-packed $\langle 110\rangle$-directions are decoration rows, which are for the smaller deposited amounts (Figs. 4.1(b) and (c)) only one atom wide, but become occasionally also two or more atoms wide (named fat decoration rows, fDR's) for larger deposited amounts (compare Figs. 4.1(c)-(f)). The inset of Fig. 4.1(a) displays a triangular stacking fault area bounded by tDR's. On the large coalesced terrace of the first layer a new sequence of island nucleation has taken place and regular as well as faulted nucleated in the second layer. These decoration rows separate areas of different stacking sequence. The decoration rows tend to start or end in grooves, indicating that phase boundaries of differently stacked areas are frequently hidden in these grooves.

In Fig. 4.1(f) with $\Theta = 5\,\mathrm{ML}$ the STM-topograph still indicates layer-by-layer growth. The fifth layer is nearly closed and islands of considerable size in the sixth layer are visible. A close inspection reveals now the presence of a large number of tDR's. They often terminate in grooves and islands are frequently attached to them. Their shape is influenced by the presence of tDR's and their shapes and sizes are extremely heterogeneous. Figure 4.2 shows snapshots of the surface morphological evolution for $\Theta = 10\,\mathrm{ML}$ up to $\Theta = 90\,\mathrm{ML}$. Apparently for these thicker films the layer-by-layer growth is lost. The morphology becomes rather heterogeneous. It is dominated by mounds, which are frequently elongated along one of the $\langle 110\rangle$-directions and are of needle-like shape. Also deep grooves are apparent. The insets highlight that these structures are essentially wide decorations rows, from which partly materials starts to grow away. Apparently DRs act as a preferential nucleation sites for adatom islands and replicate themselves on top of each such newly formed adatom island, giving rise to the onset of three dimensional mound formation.

Although the overall roughness is not large, it is clearly increasing with the deposited amount and even for the largest deposited amounts far from saturation. Based on the visual impression given by the STM topographs one would state a growth mode transition from layer-by-layer growth to a heterogeneous mound growth for Θ somewhere around $10\,\mathrm{ML}$. The quantitative roughness evaluation shown in Fig. 4.4 suggests this transition to take place already at $5\,\mathrm{ML}$. It displays a power law for the increase of roughness with coverage for deposited amounts $\geq 5\,\mathrm{ML}$ with a growth exponent $\beta = (0.31 \pm 0.01)$. Only for smaller Θ the roughness shows a slower increase.

Although the neighboring 5d transition metals Ir and Pt are quite similar in their chemical properties, the observed Ir growth behavior on Ir(111) is

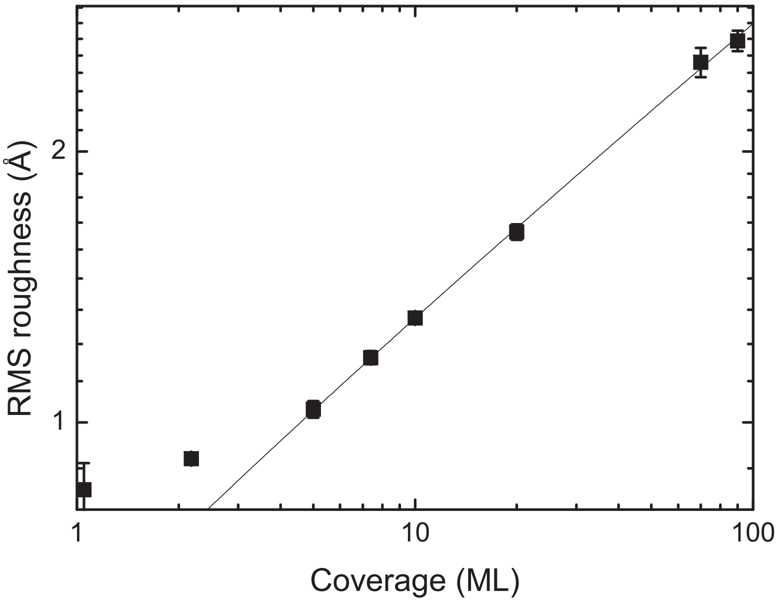

Figure 4.4: RMS roughness for coverages up to 90 ML. The line represents a fit to a power law with an exponent $\beta = (0.31 \pm 0.01)$.

in marked difference to the one of Pt on Pt(111). At the same temperature - scaled with respect to the corresponding cohesive energies - Pt on Pt(111) displays the growth of mesa mounds separated by grooves of several layer depth [35]. Generally, for 5 ML deposited and temperatures up to 650 K the roughness for the same scaled temperature is always significantly lower on Ir(111) compared to Pt(111) [73]. While for Pt homoepitaxy on Pt(111) a significant - though temperature dependent - effective step edge barrier is operative [35], this is not the case for Ir(111). In contrary, once Ir adatoms reach a descending step they are trapped, unable to return to the terrace and eventually descent [37]. Thus, while the step edge barrier on Pt(111) enhances the nucleation probability on top of islands and thereby makes growth rough, the efficient incorporation of adatoms into descending steps on Ir(111) keeps the surface smooth. The observed roughening for Ir on Ir(111) is thus solely attributed to the defect dominated, heterogeneous nucleation.

Unlike for many other homoepitaxial growth systems, inspection of Figs. 4.1 and 4.2 indicates no or very little coarsening. The quantitative analysis of the evolution of the lateral length scale is based on the height-height correlation function $G(\boldsymbol{r})$ for representative topographs [74, 75]. As a measure for

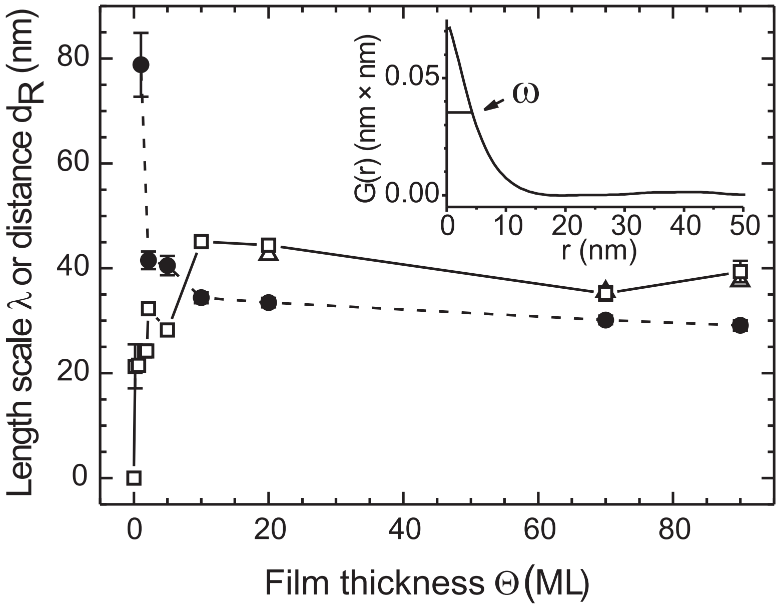

Figure 4.5: Average lateral length scale $\lambda = 8\omega$ as obtained from $G(r)$ (open squares) and from the radially averaged power spectral density (for $\Theta \geq 20\,\mathrm{ML}$, open triangles) as well as the average distance of decoration rows d_R (full circles) as function of Θ. Lines are only a guide to the eye. Inset: $G(r)$ of a typical image with $\Theta = 70\,\mathrm{ML}$.

the average length scale $\lambda = 8\omega$ is used with ω being the width at half maximum of the radially averaged $G(r) = \langle G(\boldsymbol{r})\rangle_{|\boldsymbol{r}|=r}$, i.e. $G(\omega) = 1/2G(0)$. In the radially averaged power spectral densities for deposited amounts larger than 20 ML a single peak develops indicating the dominant wavelength in the morphology and is thus another estimate for λ. As visible in Fig. 4.5 after some initial scatter (related to the phase of growth in the layer-by-layer regime) around 10 ML a fixed length scale of about 40 nm establishes. For the same $\Theta \approx 10\,\mathrm{ML}$ also the decoration row density reaches a saturation value. In Fig. 4.5 the square root of the inverse decoration row density - the average decoration row separation d_R - is plotted. The remarkable coincidence of the saturation of λ and d_R as well as their rough agreement in their saturation magnitude are strong hints for a link between these two quantities. With the observation of Fig. 4.2 that eventually most mounds contain a DR this link is evident. Structure formation is dominated by the presence of DR's. Indeed, they are sites of heterogeneous nucleation for

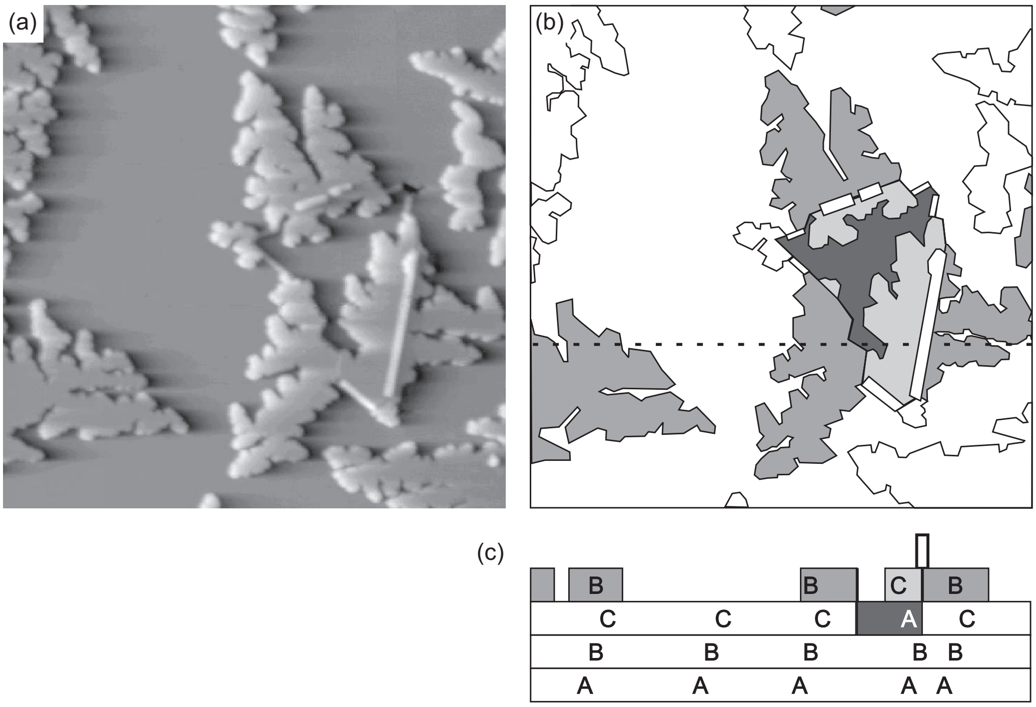

Figure 4.6: (a) STM topograph of a stacking fault area with decoration rows. Image size 56 nm × 56 nm. (b) Schematic drawing of the situation of (a). Shading according to the stacking sequence (see (c)). All area other than white is twinned surface area with a single buried stacking fault. (c) Cross section of (b) along the dotted line. Labeling of the layers with A, B, and C indicates the stacking sequence in the usual notation (compare e.g. [76]). See also text.

adatom islands, thereby eliminating homogeneous island nucleation together with layer-by-layer growth.

4.2 The Proliferation Effect

A key to understand the morphological evolution may be found in Fig. 4.6. Fig. 4.6(a) displays a STM topograph of a stacking fault area with DR's, which is analyzed in Figs. 4.6(b) and 4.6(c). In the layer below the island level, a triangular stacking fault area bounded by tDR's had been formed during growth (see also Fig. 4.6(c)). Compared to the terrace, the tDR's offer sites of larger coordination and thus are binding sites for the attachment of

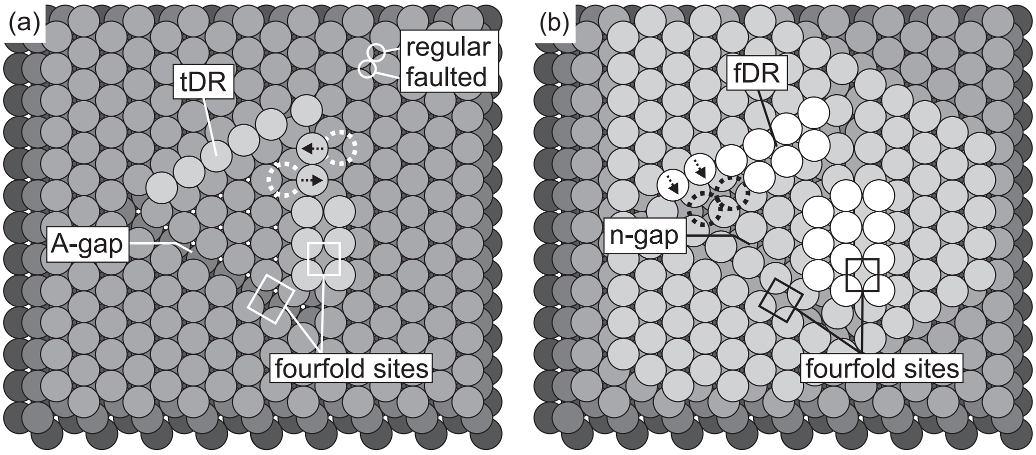

Figure 4.7: (a) Ball model displaying a triangular stacking fault area surrounded by A-gaps. The fourfold coordinated adsorption sites offered by the A-gaps are partly filled by atoms forming thin decoration rows (tDR's). Attachment of an atom at one of the locations indicated by the dashed circles causes a tDR atom to relax slightly away from its fourfold coordinated adsorption site, either inward or outward. Inward relaxation of a tDR by a few atoms attached at the outside of the triangle is shown. Thereby new fourfold adsorption sites are created in the next higher layer. b) Situation in the next higher layer. If the inner area is filled with atoms, a narrow gap (n-gap) between the tDR and the next row of atoms is formed. A fat decoration row (fDR) is created by occupying sites on the n-gap (dashed circles) next to a tDR and the inward relaxation of the tDR. Attaching further atoms leads to new fourfold sites.

additional atoms. In consequence and as visible in Fig. 4.6(a), heterogeneous nucleation of island branches took place at the tDR's. Attachment of atoms and subsequent growth will cause the positions of the fourfold coordinated tDR atoms to relax a little from their ideal positions. As indicated by the arrows in Fig. 4.7(a), a tDR atom may in principle relax in both directions normal to the tDR. If the tDR's relax outwards, an intrinsic stacking fault (two faults on subsequent planes) is formed *inside* the triangular area, while no fault is induced outside of it. As two faults cancel each other, without additional faults in subsequent growth the area would be detected as regular. If the tdR's relax inwards, towards the center of the triangular faulted area, *outside* new stacking faults are induced, while inside no new fault is formed. If no additional faults are placed during subsequent growth, the triangular area *and* its surrounding would be detected as twinned.

Many situations similar to the one depicted in Fig. 4.6 were analyzed and one invariably finds that the latter situation is realized, i.e. no intrinsic faults are formed. This may be concluded with certainty from the analysis of the preferential growth directions of the islands growing away from the tDR's. For example, the islands which heterogeneously nucleated at the tDR's of the central faulted area in Fig. 4.6(a) exhibit only growth directions characteristic for faulted growth (compare with Fig. 4.1(a)). Density functional theory calculations [76] for faults on Ir(111) net planes yield $0.086\,\mathrm{eV/atom}$ for a single fault (a twin), but $0.112\,\mathrm{eV/atom}$ to form a second fault immediately above an existing one, i.e. to complete the formation of an intrinsic fault. In the presence of sufficient mobility of atoms attaching to tDR's, it is this energy difference of about $0.026\,\mathrm{eV/atom}$ which causes the avoidance of intrinsic faults and the preference for the creation of new faults outside the already faulted triangular area. Thus tDR's couple fault probabilities in two layers, prevent cancellation of existing faults by second ones and cause rapid lateral fault proliferation.

The effect of tDR's alone, however, would neither be sufficient to explain the observed growth mode. There are two more effects to consider: (i) An initial tDR gives rise to the formation of an fDR in the layer above, which replicates itself over and over again in higher layers. (ii) These fDR's prevent the introduction of further stacking faults adjacent to their both sides.

The self-replication of DR's is based on the fact that a DR always induces the formation of fourfold coordinated, "sticky" sites one layer above. Fig. 4.7(b) depicts the transition from tDR's to fDR's. After the tDR has been incorporated into the layer, there are two adjacent rows of preferred adsorption sites: the fourfold coordinated ones and next to them those which are above the narrow gap in the layer below. Growth causes therefore first the formation of a new decoration row of double atomic width or fDR (as also visible in Fig. 4.6(a) *on* the central island structure) and then subsequent attachment of atoms to both sides (i.e. heterogeneous island nucleation and growth). The attachment on both sides of the fDR is only possible on regular sites (see Fig. 4.7(b)) and induces the new formation of fourfold adsorption sites (see Fig. 4.7(b)) for atoms of the next higher layer which in turn initiates again decoration row formation (and so forth).

4.3 Methods of Stacking Fault and Twin Detection

In order to characterize the evolution of stacking faults and their influence on the thin film morphological evolution the fraction of surface area in faulted stacking θ_F is used. The meaning of θ_F and how it is measured will be come evident in this section.

4.3.1 Direct Observation of Stacking Faults in the First Monolayer by STM

As already pointed out and visualized in the inset of Fig. 4.1(a), islands in the first monolayer point in two opposing directions rotated by 180°. The reason for the two triangle orientations is as follows. Due to the potential energy landscape at the step edge Ir islands on Ir(111) are predominantly bounded by $\{111\}$-microfacetted steps [9] (B-steps) along the $\langle 110 \rangle$-directions. As visualized in Fig. 4.3 the preference for B-steps implies immediately the apparent 180° rotation of faulted islands. For a given Θ prior to island coalescence, faulted and regular islands have the same average island size. Determining the probability P_F for a stacking fault island – the fraction of faulted islands – yields the surface area in faulted stacking as $\theta_\mathrm{F} = P_\mathrm{F}\Theta$. The stacking fault probability for nucleation on the substrate layer is simply obtained by evaluating the fraction of islands in fault island orientation (apparent rotation by 180°). On the substrate layer – layer zero – is $P_{\mathrm{F},0} = 11\,\%$ for 350 K (compare Ref. [8]).

When islands coalescence, an efficient self-healing effect mechanism as described in detail in reference [49] sets in which largely transforms faulted islands to regular stacking. This process takes place when a regular and faulted island have approached such that they are only separated by a gap of subatomic width formed by two A-steps (compare Fig. 4.3). Then through atomic jumps of atoms over the gap at kink positions within A-gaps from a faulted to a regular position, the size of the faulted area decreases. This process comes to a rest, if the sticky A-gap displaying fourfold coordinated adsorption sites becomes decorated by atoms. Thus in a partly coalesced island with a fault island envelope, the position of a decoration row marks the part of the island that has been transformed already to regular stacking as visible in the inset of Fig. 4.1(b).

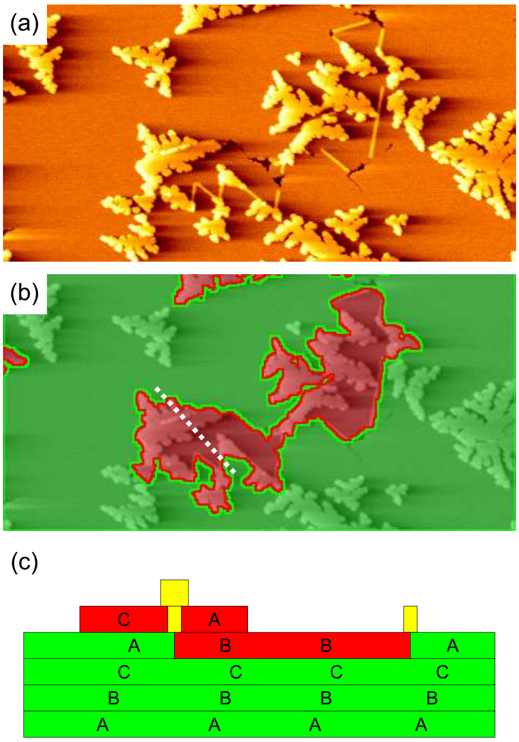

Figure 4.8: (a) STM topograph after deposition of 2.18 ML at 350 K. (b) STM topograph as in (a) but with faulted areas colored in red and unfaulted area in green. (c) Schematic intersection of the crystal along the dotted white line in (b) indicating the stacking sequence.

4.3.2 Stacking Fault Detection after Deposition of a Few Monolayers by STM

After completion of the first layer the self healing mechanism leaves only small patches in faulted stacking sequence. Such patches are bounded by decoration rows. Partly the boundary of such patches may also consist in grooves reaching down to the substrate layer. Taking into account these patches and the amount of faulted area due to fault islands on the upmost connected layer yields again θ_{F}.

For island nucleation in subsequent layers surprisingly a clear increase of P_{F} was found. Taking into account only islands not attached to decoration row structures, $P_{\mathrm{F},1} = 33\,\%$ for nucleation on the first deposited monolayer and $P_{\mathrm{F},2} = 41\,\%$ for nucleation on the second deposited monolayer. Both values are much larger than $P_{\mathrm{F},0} = 11\,\%$ obtained for nucleation on the substrate layer. The increased P_{F} in higher layers must be assumed to cause an increase of the maxima of θ_{F} prior to the onset of self-healing by island coalescence. Indeed, the maximum value for θ_{F} increases from $\theta_{\mathrm{F}} = 7\,\%$ for $\Theta = 0.7\,\mathrm{ML}$ to $\theta_{\mathrm{F}} = 21\,\%$ for $\Theta = 1.6\,\mathrm{ML}$. It will be shown below that steps play a crucial role for this increase.

An example for the determination of θ_{F} is shown in Fig. 4.8 after deposition of 2.18 ML. Figure 4.8(a) displays an area with a large number of decoration rows and islands attached to them. The associated fault island area is identified in Fig. 4.8(b) and color coded in red. The faulted area is bounded by decoration rows, grooves and islands in the top layer. The islands in the top layer in this area possess all the characteristic fault island orientation. The interpretation is as follows. At the location of the islands initially only decoration rows were present. Attachment of additional atoms to the decoration rows results in island growth. As described in the previously, stacking faults in two subsequent layers (intrinsic stacking faults) are energetically avoided. Thus the material is attached in such a way, that the adatom islands growing towards the inside of the area with the fault located in the first layer does not introduce an additional fault in the second layer. This implies that the islands growing towards the outside are in fact fault islands. Thereby the faulted area increases and fault proliferation takes place. One of the larger second layer islands carries already again a decoration row, but of two atom width. The schematic sketch of the layer stacking along the dotted black line in Fig. 4.8(c) clarifies the stacking sequence. It should be mentioned that the two atom wide decoration row (a fat decoration row) now separates two faulted areas with faults in different levels rather than a faulted and a regular area as for the thin one atom wide decoration rows. As will be discussed below, in general a fat decoration row separates two faulted areas with faults in different layers and the width of the decoration row increases with the depth of the faults.

Here is also the place for a remark on terminology. For stacking fault areas thicker than one atomic layer it is more common to talk of twin crystallites. The substrate layer, a faulted layer and a third layer on top – not introducing a new fault with respect to fcc-stacking – are a three layer system defining again an fcc-stacking sequence. This sequence defines a twin crystallite, which becomes indistinguishable from the original crystal in symmetry if rotated by 180° through an axis normal to the plane of the stacking fault. This implies that an additional stacking fault several layers above the initial one will cancel its effect and a buried twin crystallite results. In top view the surface area will appear free of faults. However, once fat decoration rows are formed, they pin the stacking sequence in their neighborhood and fault cancellation does not take place. The plane of the stacking fault is usually termed coherent twin boundary [1]. It is the grain boundary with the lowest energy, about 0.09 eV per atom for Ir [8, 44, 77], and displays no change of atom coordination (and thus density) or distance over the boundary. The boundary laterally separating grains twinned in different layers or twinned grains from untwinned ones is named incoherent twin boundary [1]. For the case of Ir(111) the incoherent twin boundaries are boundaries of reduced density, giving rise to the observable decoration row structures (see also below).

4.3.3 Measuring the Surface Area of Twin Crystallites by LEED

With increasing Θ the STM method for determination of θ_F becomes more and more ambiguous and for $\Theta > 5\,\mathrm{ML}$ the method is not more applicable.

If one considers the surface to be formed by regular and twin crystallites, defined in each case by three properly stacked layers, LEED appears to be the ideal method for the determination of θ_F. LEED is surface sensitive and the diffracted intensity results to a very good approximation from the topmost three layers. Thus for an entirely twinned crystal of at least three layer thickness the intensity I versus electron energy E curves (I/V curves) are identical to those of an untwinned crystal, but with the I/V curves of the (10) and (01) diffraction spots interchanged. With $I_{10}(0, E)$ and $I_{01}(0, E)$ being the I/V curves of the (10) and (01) spots of the clean surface, respectively, the intensity $I_{10}(\Theta, E)$ of a (10) spot of a partly twinned surface may be expressed as follows:

$$I_{10}(\Theta, E) = (1 - \theta_\mathrm{F})\, I_{10}(0, E) + \theta_\mathrm{F}\, I_{01}(0, E) \tag{4.1}$$

$$I_{01}(\Theta, E) = \theta_\mathrm{F}\, I_{10}(0, E) + (1 - \theta_\mathrm{F})\, I_{01}(0, E) \tag{4.2}$$

The method described relies on the assumption of a surface composed of twin crystallites and regular crystallites, i.e. on the assumption that the stacking faults are two or more layers underneath the surface. While this assumption is evidently not fulfilled for only a few monolayers deposited, in the regime where the surface morphological evolution is dominated by heterogeneous nucleation at the defect structures, i.e. for $\Theta > 10\,\mathrm{ML}$, it is fulfilled to a good approximation. As then homogeneous nucleation is largely

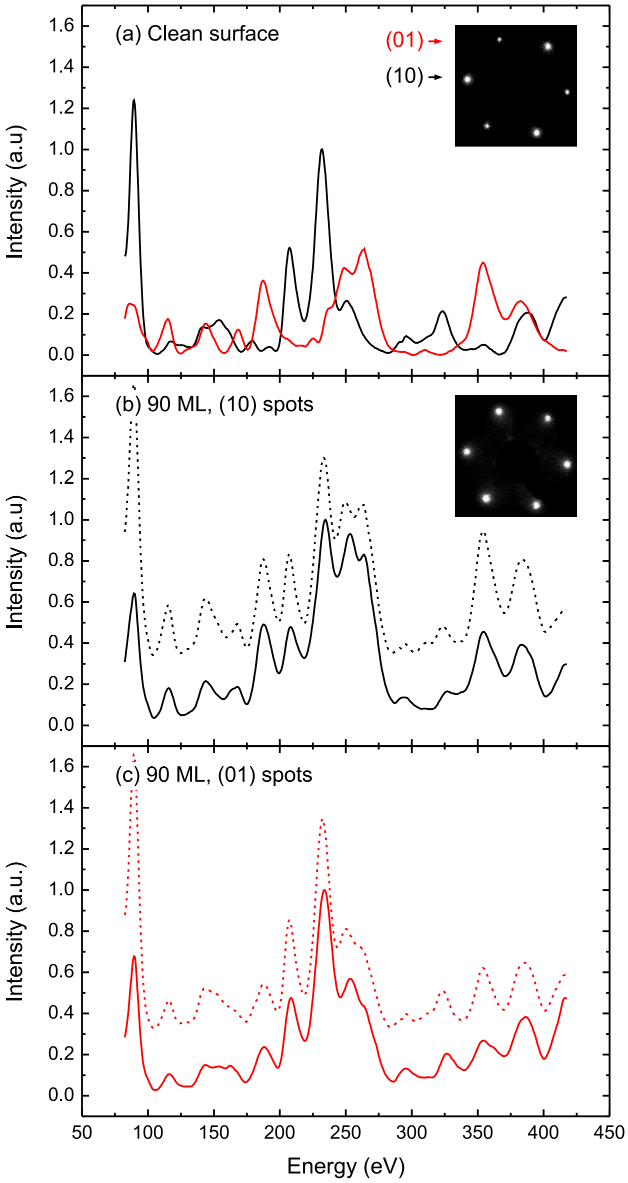

Figure 4.9: (a) LEED intensity I versus electron energy E curves $I_{01}(0, E)$ and $I_{10}(0, E)$ of the clean surface (0 ML deposited) for the (10) (black) and (01) (red) spots, respectively. (b) Measured (full line) and fitted (dotted line) intensity $I_{10}(90\,\mathrm{ML}, E)$ after deposition of 90 ML at 350 K. (c) Measured (full line) and fitted (dotted line) intensity $I_{01}(90\,\mathrm{ML}, E)$ after deposition of 90 ML at 350 K. In (b) and (c) measured and calculated curves are offset with respect to each other for clarity. Insets: LEED images at 235 eV.

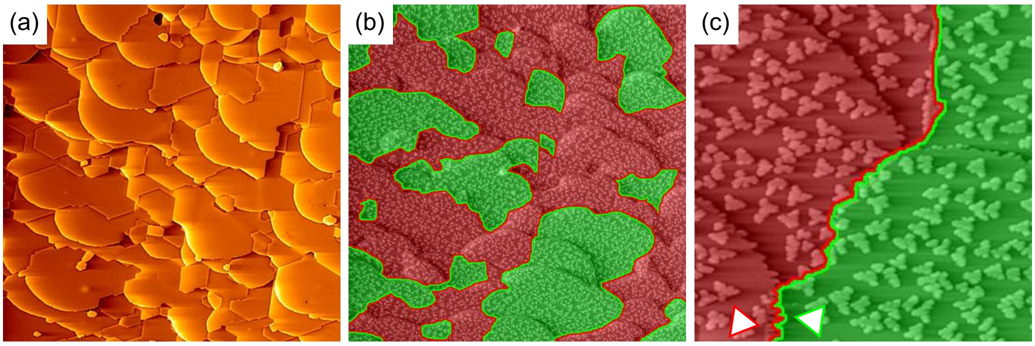

Figure 4.10: Illustration of the post decoration method for the detection of twinned surface areas. (a) Surface after deposition of 90 ML at 350 K and additional annealing to 1200 K for 180 s. (b),(c) Surface after decoration through approximately 0.2 ML Ir at room temperature. Twinned areas are colored red, untwinned areas are colored green. The areas are identified by the predominant orientation of the triangular envelope of the decorating islands indicated in (c) through white triangles. Image sizes 500 nm × 500 nm for (a) and (b), 105 nm × 105 nm for (c).

absent, no new faults are introduced in the top layer. The change of θ_F is then largely due to the lateral shifts of boundaries between regular and twin crystallites and is a slowly varying function of Θ.

Figure 4.9 displays an example for the application of this method. For a 90 ML thick film grown at 350 K both $I_{10}(90\,\mathrm{ML}, E)$ and $I_{01}(90\,\mathrm{ML}, E)$ are fitted with the single parameter θ_F on the basis of the measured $I_{10}(0, E)$ and $I_{01}(0, E)$. As visible in Figs. 4.9(b) and (c) the measured and fitted spectra coincide with high perfection with a Pendry R-Factor of 0.12[78, 79]. It should be noted that slightly annealed films show unchanged θ_F but a considerably reduced Pendry R-Factor (e.g. $R = 0.07$ after annealing to 850 K), most likely due to reorganization of the atoms in extended defect structures to lattice positions, either of regular or faulted crystallites (see below).

4.3.4 Twin Crystallite Identification in Annealed Films by STM through Post Decoration

The high stability of the twin crystallites formed during Ir homoepitaxy against thermal healing offers a unique possibility to apply a post decoration method previously used in TEM studies of epitaxial growth [5]. The method requires sufficiently large terraces, such that homogeneous nucleation of new islands upon Ir deposition takes place. During annealing to 850 K surface diffusion is efficient enough to smoothen the surface to an extent such that upon room temperature deposition new Ir islands nucleate on the terraces formed. While in regular areas the triangular envelope of the newly formed islands will point downwards with a probability of about 90 %, in the faulted areas they will point upwards with the same probability. The differing predominant orientations of the islands together with the finding that twinned and untwinned areas are separated by steps (not necessarily of monatomic height) allows straightforward determination of θ_{F}.

Figure 4.10 displays an example for the application of the post decoration method after annealing a 90 ML film to 1200 K.

4.3.5 Quantitative Comparison of LEED and STM Methods Applied to Annealed Films

For smooth annealed films the results for θ_{F} obtained by the STM post decoration method and from fitting LEED I/V curves may be compared to each other. The comparison is exemplified in Fig. 4.11 for an annealing sequence of a 90 ML thick film grown at 350 K. According to the LEED measurements $\theta_{\mathrm{F}} \approx 0.6 - 0.65$ up 1050 K, after annealing to 1200 K it is still above 0.5 and does not vanish at all after annealing to 1350 K, the highest temperature applied in this sequence. For the films annealed to 850 K and higher temperatures the STM post decoration method could be applied. The results agree within the limits of error with the LEED I/V curve method. The larger error margins for the STM post decoration method after annealing to high temperatures are caused by the large domain sizes which cause within the limited number of topographs analyzed significant fluctuations in θ_{F}.

The LEED I/V curve and the STM post decoration methods for annealing sequences of several films were compared and the values for θ_{F} were found to agree always better than 10 %. However, there is a clear tendency for the STM post decoration method to yield slightly larger values for θ_{F} which is also visible in Fig. 4.11. The origin of this difference is traced back to the different surface area sampling by LEED and STM. For the STM analysis large scale topographs are needed. Such topographs are usually taken in relatively smooth surface areas with a limited number of preexisting steps. In regions where the initial step distribution formed step bundles (such regions

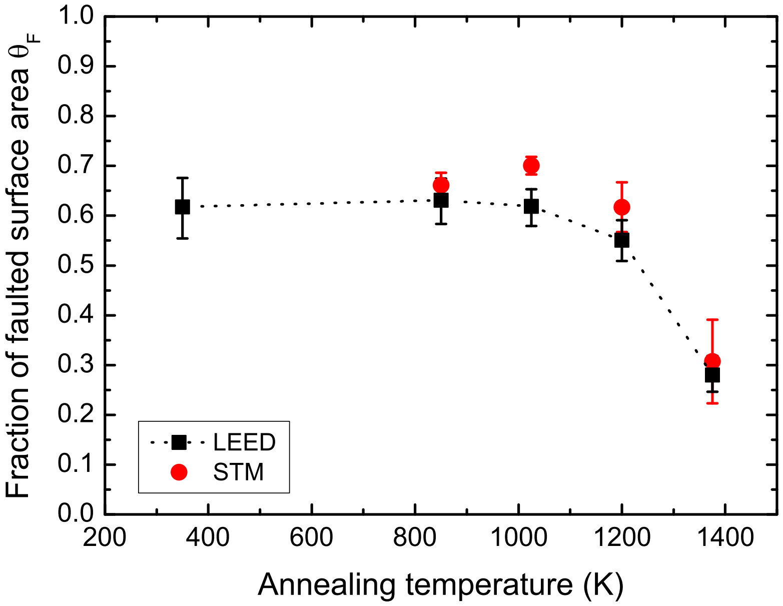

Figure 4.11: Comparison of θ_F for a 90 ML Ir film measured by LEED (full black squares) and STM (full red circles) after subsequent annealing steps of 180 s to the temperatures indicated. Lines are only a guide to the eye.

always exist) large scale topographs are hardly taken due to the large height variations which make imaging difficult. In such regions with small initial terrace sizes step flow growth is prevalent even at 350 K. Due to the growth away from steps in regular stacking sequence, twin crystallite formation is absent or at least rare. While STM sampling excludes such areas, LEED as a macroscopically averaging method includes the intensity contribution from the step bundle areas and thus obtains a smaller value for θ_F.

4.4 Influence of Stacking Faults and Twinning on the Growth Beyond the First Monolayer

A summary of the measurements for θ_F with the different methods discussed in the previous section is shown in Fig. 4.12. Different amounts of Iridium were deposited at 350 K without subsequent annealing. The quantity θ_F

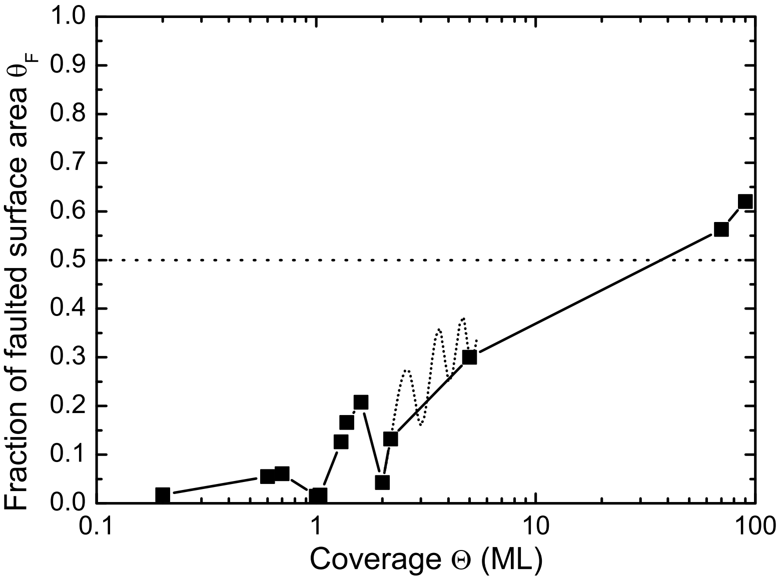

Figure 4.12: Fraction of surface area covered by stacking faults θ_F versus Θ. Full black squares: Experimental data. The lines are only a guide to the eye. Dotted line: Probable behavior of θ_F between experimental data points. Data below $\Theta = 10\,\mathrm{ML}$ measured by STM and above by LEED. All films grown at 350 K without annealing.

shows in the range of a few layers clear oscillations and then increases to values considerably larger than 50%.

In a toy model for twinning, a fixed, layer independent, stacking fault probability P_F during thin film growth is assumed. For simplicity it is assumed to be identical to the fraction of area changing its character (from regular to twinned or from twinned to regular). Then, in the layer $N+1$ the area of regular stacking $A_{N+1,reg}$ and the twinned area $A_{N+1,twin}$ are:

$$A_{N+1,twin} = P_\mathrm{F} A_{N,reg} + (1-P_\mathrm{F}) A_{N,twin} \tag{4.3}$$

$$A_{N+1,reg} = (1-P_\mathrm{F}) A_{N,reg} + P_\mathrm{F} A_{N,twin} \tag{4.4}$$

Independent of the starting conditions and for nonzero P_F, this model yields equal amounts of twinned and regular surface area for sufficiently large N. As this contradicts the experimental results, apparently there must be some correlation between the introduction of stacking faults in different layers.

In contrast to the experiments at 350 K, experiments at low temperatures, where self-healing and as a consequence the proliferation effect is suppressed,

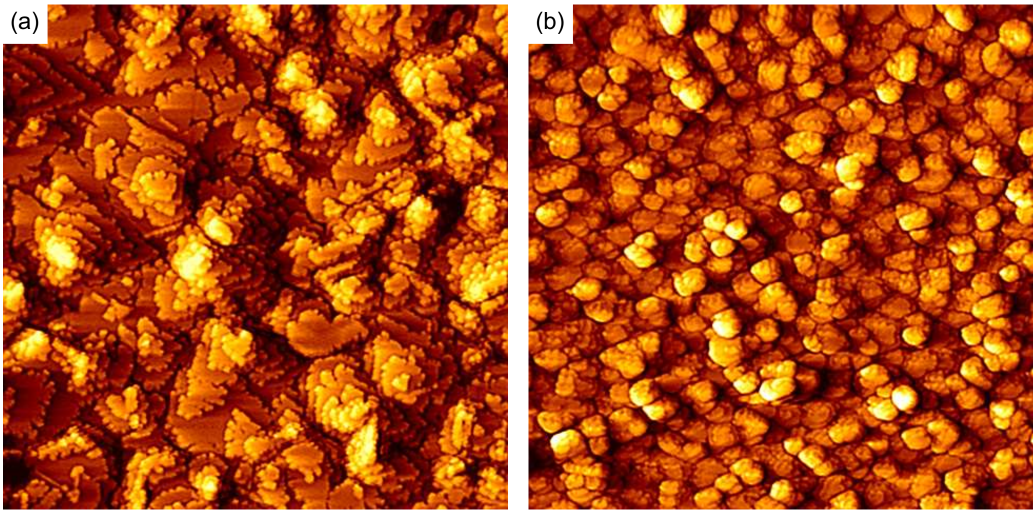

Figure 4.13: STM topographs of (a) 90 ML Ir/Ir(111) deposited at 350 K and (b) 50 ML Ir/Ir(111) deposited below 210 K. Image size 120 nm × 120 nm.

show the expected behavior. After deposition of 50 ML at temperatures below 210 K (Fig. 4.13(b)), the surface exhibits – within the limits of error of the LEED analysis – 50% twinned stacking. For this reason, a link between the proliferation effect and the twinning behavior appears evident.

4.4.1 Layer Dependence of P_{F} and θ_{F}

In the initial phase of growth θ_{F} is oscillatory with monolayer period. The first two oscillations for θ_{F} are visible Fig. 4.12. Based on the fact that layer-by-layer growth is still present at 5 ML, it is likely that the oscillations continue at least up to 5 ML deposited. This reasonable speculation is indicated by the dotted line in Fig. 4.12. Note that the full straight lines in Fig. 4.12 just connect the data points. The origin of the oscillations is the self-healing mechanism mentioned already above which removes in a growing layer most of the newly formed stacking fault upon layer closure. The value of θ_{F} in the oscillation minima is increasing with Θ. Note that if the oscillations persist up to 5 ML, the data point at $\Theta = 5$ ML is a minimum value, since Fig. 4.1(f) displays a situation at layer closure. The amplitude of the second oscillation in Fig. 4.12 is much larger than the amplitude of the first oscillation. Based on the argumentation below the third oscillation might have an even larger amplitude. This effect is not caused by defect structures, which only define the position of the minima in Fig. 4.12. The increase of amplitude is caused by the increase of the stacking fault probability which was found to be $P_{\mathrm{F},0} = 11\,\%$, $P_{\mathrm{F},1} = 33\,\%$ and $P_{\mathrm{F},2} = 41\,\%$ for the substrate, first layer and second layer. Assuming perfect layer-by-layer growth and absence of coalescence (and consequently self-healing) up to a layer coverage of 0.65 ML this yields maxima values for θ_{F} of 7 %, 21 %, and 27 %. The first two numbers are in decent agreement with experiment.

This rises the obvious question to why θ_{F} should be layer dependent. It is not remote to consider the possible effects of codeposited impurities. In homoepitaxy on Pt(111) it was proven that minute amounts of CO coadsorbed during evaporation give rise to drastic changes in the growth morphology [80]. In epitaxial growth of Co on Ru(0001) the nucleation probability for islands in two different stacking sequences was found to depend critically on the background pressure during deposition [81]. To test the possible influence of coadsorbed CO on stacking fault nucleation 1.4 ML were deposited in an additional CO partial pressure of 4×10^{-4} mbar. No effect on $P_{\mathrm{F},1}$ was found.

In distinction to the situation on the substrate, nucleation on the first or higher layers takes place in the presence of the step edges of trenches and holes not yet closed to the lower layer (compare Fig. 4.1(c) and (e)). As adatoms are known to be trapped on the upper terrace at the step edge [37], one could speculate that such adatoms or small clusters trapped at the step edge – trapped possibly even on stacking fault sites – could influence θ_{F}. To test this assumption the sample was first sputtered at 1000 K and about 0.3 ML were removed from the topmost layer. Under these temperature conditions the surface vacancies created due to sputtering nucleate on large terraces and form hexagonal vacancy islands while they anneal to descending step edges on terraces with a width below about 100 nm. After sputtering 0.6 ML Ir was deposited at 350 K. On the large terraces the vacancy islands were almost filled and subsequently nucleation of adatom islands took place in the presence of step edges. In these areas it was found $P_{\mathrm{F}} = 0.17$. On the narrow terraces for the evaluation of P_{F} only islands not attached to step edges were analyzed and one finds $P_{\mathrm{F}} = 0.10$. Although, due to the different growth situation the enhancement effect is not as strong as in pure homoepitaxy, this test experiment shows the decisive influence of step edges on the nucleation of stacking fault islands.

The trapping of adatoms or small clusters at step edges in stacking fault sites can be considered to be a likely origin of the enhancement effect. This

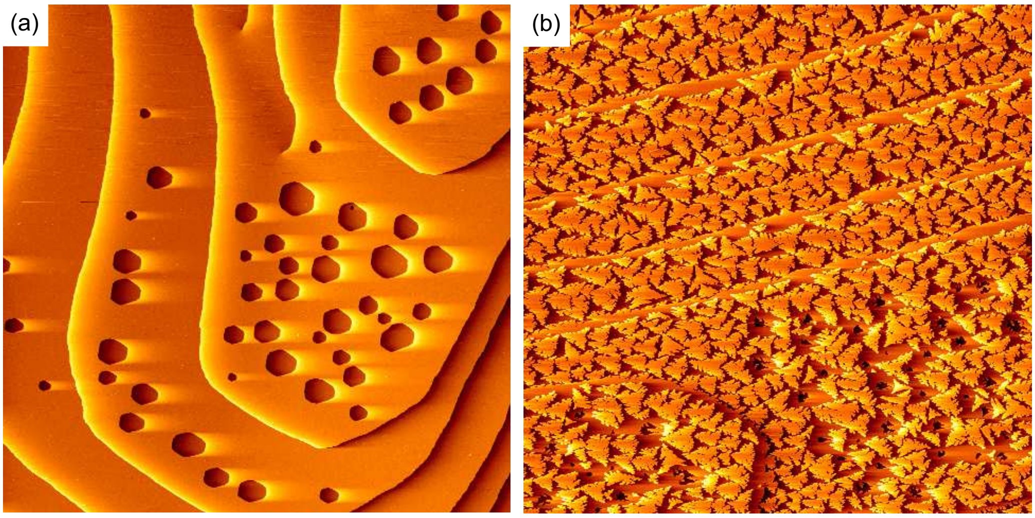

Figure 4.14: (a) Ir(111) after sputtering at 1000 K. (b) Topograph after additional deposition of 0.65 ML Ir at 350 K on the surface prepared in (a). See text. Image size 540 nm × 540 nm.

assertion is consistent with the explanation for Ir adatoms and dimers to populate preferentially faulted sites [45]. For transition metals with increasing d-band filling a change from hcp to fcc stacking takes place. Ir has just a sufficient filling to obtain fcc stacking. Small cluster at the surface, however, experience through their reduced coordination a smaller effective d-electron density and thus are preferentially on hcp sites. Adatoms and dimers at step edges would experience an even lower effective d-electron density and could populate hcp sites with an even stronger preference. Step related surface strain was also postulated to influence P_{F} distant from steps in homoepitaxy on Cu(111) [4]. To pinpoint the step related enhancement effect additional dedicated experiments are necessary.

4.4.2 Influence of the Proliferation Effect

While the enhanced P_{F} in higher layers increases the maxima in θ_{F}, this effect alone is not what eventually causes the majority of the surface to become twinned. This transformation is brought about by the processes increasing the level of the minima in θ_{F} and damping out the oscillations. Stacking fault areas are protected against self-healing through decoration row formation and form twin crystallite seeds. Once decoration rows are formed, they induce in higher layers stacking faults in the surrounding of the initial fault area by the proliferation effect and stabilize the new stacking sequence resulting in stable twins. As such twin seeds may be formed in each new layer, the amount of twinned surface area increases. As during growth the surface roughens and nucleation is eventually almost exclusively at defects and defect structures preserving the stacking sequence, oscillations die out and the majority of the surface transforms to the twinned state.

The ball model cartoons of Fig. 4.15 sketch the evolution of a twin crystallite, illustrate the general statements above and extend the previous model for higher layers.

Upon close encounter a faulted area to the left of Fig. 4.15(a) (stacking sequence ABA) forms an A-gap with an unfaulted area (stacking sequence ABC) on the right. The A-gap becomes decorated through a thin decoration row in Fig. 4.15 (b). Through the energetic avoidance of intrinsic stacking faults (two faults in subsequent layers) atoms attaching to the decoration row will shift the decoration row atoms slightly to the left, thereby creating new fourfold coordinated adsorption sites. Further attachment under the constraint of optimum coordination of the attaching atoms results in the formation of an fcc twin crystallite (stacking sequence ABAC) on the left and the introduction of a new fault on the right (stacking sequence ABCB) (compare Fig. 4.15(c)). This introduction of the new fault to the right enlarges θ_{F} and is the key process for proliferation of twins. Note that a small gap remains to the left of the fourfold coordinated adsorption sites in Fig. 4.15(c).

In the fifth layer again first the strongly bonding fourfold coordinated adsorption sites are filled (compare Fig. 4.15(d)). Next, atoms cover the small gap formed by undercoordinated atoms right to the fourfold adsorption sites. After these two rows of atoms are adsorbed - forming a fat decoration row - further addition of atoms under the constraint of optimum coordination of the attaching atoms results in preserved stacking sequence on both sides of the defect structure: On the left the stacking sequence is ABACB and on the right it is ABCBA (compare Fig. 4.15(e)). Note that left to the fourfold coordinated adsorption sites a small gap in the layer remains. In the sixth layer again the fourfold coordinated adsorption sites are filled first and then the two rows left of them next to cover the small gap in the layer below. Now a three atom wide fat decoration row is formed (compare Fig. 4.15(f)). Filling the sixth layer again under the constraint of optimum coordination of the attaching atoms results in the situation depicted in Fig. 4.15(g). No new stacking faults are introduced and the stacking sequences are ABACBA

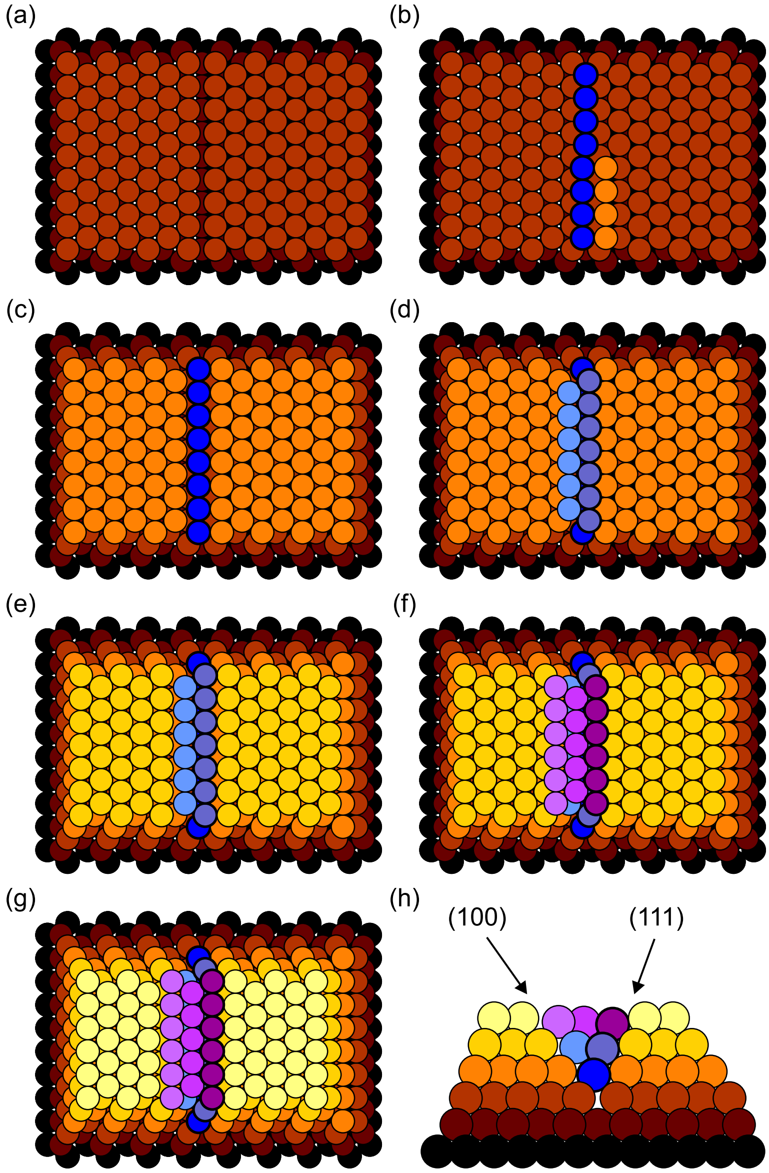

Figure 4.15: (a)-(g) Top view ball model cartoons on growth after introduction of a stacking fault on the left hand side in (a). (h) Cross section through (g). See text.

to the left and ABCBAC to the right.

Note that during the sequence of cartoons Fig. 4.15(a)-(g) the fourfold coordinated adsorptions sites move to the right while the gap moved to the left, creating an expanding defective area in between. The cross section in Fig. 4.15(h) shows that the defective area between the two twins is bounded by a (100) plane to the left and a (111) plane to the right. The central defective area has a lower atomic density (in each layer 1/3 of an atom row is missing) and is depressed. Continued growth will preserve the stacking sequence and extend the defective area which is initially bounded by (111) and (100) planes between the two twin crystallites[1]. Thus the twinned surface area will remain twinned during growth.

Based on this description, one might expect the entire surface to transform to the twinned state. At least up to 90 ML this is not the case. The STM investigations do not allow one to obtain a clue on the nature of incoherent twin boundaries separating a twinned crystal from an untwinned crystal, which could explain why not the entire surface becomes twinned. In thick films, adjacent to elongated mounds resulting from decoration row defect structures frequently deep grooves can be seen which could be such boundaries.

The structure of the incoherent twin boundaries will be also subject of the SXRD investigations presented in the next chapter, which allow one to gain insight in the structures below the surface.

4.5 Conclusion

In conclusion a transition from layer-by-layer growth to a defect dominated growth with a fixed length scale was observed in homoepitaxy on Ir(111). During this transition, the majority of the surface area becomes twinned. At the beginning of this transition, the formation of thin, monoatomic decorations rows on the phase boundary between regular and faulted surface areas takes place. Next the energetic avoidance of the formation of intrinsic stacking faults causes the spread of these initial fault areas into their surroundings. Replication of decoration rows in higher layers acting as nucleation centers and suppression of new fault formation next to them completes this transition. A step-influenced enhancement of the stacking fault probability initially supports the effect.

---

[1] While it is likely that the (111) plane defined by the locations of the fourfold coordinated adsorption sites remains a boundary of one twin crystallite, this is not obvious for the other twin crystallite boundary starting out as a (100) plane. From the STM topographs it appears that the width of the defective area between the two crystallites stays limited to several nm even for the thickest deposited films. Therefore, the initial (100) facet probably does not stay in this orientation for thicker films.

5 Annealing Behavior and Stability of Twinned Films

Based on the previous results, the growth and annealing behavior of strongly twinned homoepitaxial films on Ir(111) has been investigated by scanning tunneling microscopy, low energy electron diffraction and surface X-ray diffraction. It is found that the stacking faults in Ir thin films on Ir(111) give rise to fractional steps marking the locations of incoherent boundaries. The healing of twinned areas takes place in a two step process, in which first the length and area of incoherent boundaries is reduced through a coarsening process before eventually the twin crystallites are removed themselves. The nature of the incoherent boundaries is uncovered by the SXRD measurements. A model for the structure of the incoherent twin boundaries is proposed which is consistent with the available scanning tunneling microscopy and surface X-ray diffraction data[1].

5.1 Results

The results will be presented in three parts: First the results of the STM experiments will be shown, which also act as reference for the following experiments. With respect to these results, the system was investigated using SXRD. The results of the SXRD experiments are presented second, followed by a comparison between both.

---

[1] The SXRD experiments and simulations have been performed in cooperation with Johann Coraux, present address Institut Néel, CNRS-UJF, 25 rue des Martyrs, BP166, F-38042 Grenoble Cedex 9, France, and Gilles Renaud and Odile Robach, Commissariat à l'Energie Atomique, Institut Nanosciences et Cryogénie, 17 Avenue des Martyrs, F-38054 Grenoble, Cedex 9, France.

5.1.1 STM Experiments

Fig. 5.1(a)-(d) displays characteristic elements of a homoepitaxial growth sequence on Ir(111) already discussed in more detail in the previous chapter. After deposition of 0.2 ML as in Fig. 5.1(a) dendritic islands are visible. They display a triangular envelope due to the preferred formation of {111}-microfacetted step edges. The island in the image center is mirrored (or rotated by 180°) in orientation. This mirrored orientation marks stacking fault islands with the atoms residing in the threefold coordinated hollow sites corresponding to an hcp rather than an fcc stacking sequence. Continued deposition gives rise to island coalescence and most stacking faults islands switch to regular stacking during this process [49] as visible in Fig. 5.1(b). However, occasionally at the boundary between regular and faulted areas narrow stripes of subatomic width remain, which offer fourfold coordinated adsorption sites. This gap and thus also the faulted area bounding one of its sides becomes stabilized by adatoms forming a monatomic width decoration row oriented along $\langle 1\bar{1}0 \rangle$ (Fig. 5.1(b)). Continued growth takes place preferentially by heterogeneous nucleation at these decoration rows. It causes the formation of additional faults (fault proliferation, see section 4.2), stabilizes existing ones and leads to the embedding of twins. In Fig. 5.1(c) the situation after 10 ML deposited is shown, where overgrown decoration rows mark the separation of differently stacked surface areas. Eventually, further deposition gives rise to an irregular rough surface dominated by mounds. They result from heterogeneous nucleation at the boundaries between differently stacked areas of the films (compare Fig. 5.1(d)).

The same film is shown in Fig. 5.1(e) in a demagnified view. Each of the bright features marks a boundary boundary between areas of different

Figure 5.1 : (facing page) (a)-(d) STM topographs illustrating characteristic features at different stages of homoepitaxy on Ir(111) after deposition of (a) 0.2 ML, (b) 0.9 ML, (c) 10 ML, (d) 90 ML at 350 K. Image size in (a)-(d) is 64 nm × 64 nm. (e) STM topograph of a 90 ML film grown at 350 K. (f)-(i) STM topographs of the film shown in (e) after additional 180 s isochronal annealing steps at (f) 850 K, (g) 1025 K, (h) 1200 K, (i) 1375 K. Image size in (e)-(i) is 480 nm × 480 nm. Inset size in (f) and (g) is 120 nm × 120 nm. Small white arrows in (h) and (i) indicate emerging screw dislocation lines (junctions between up and down steps).

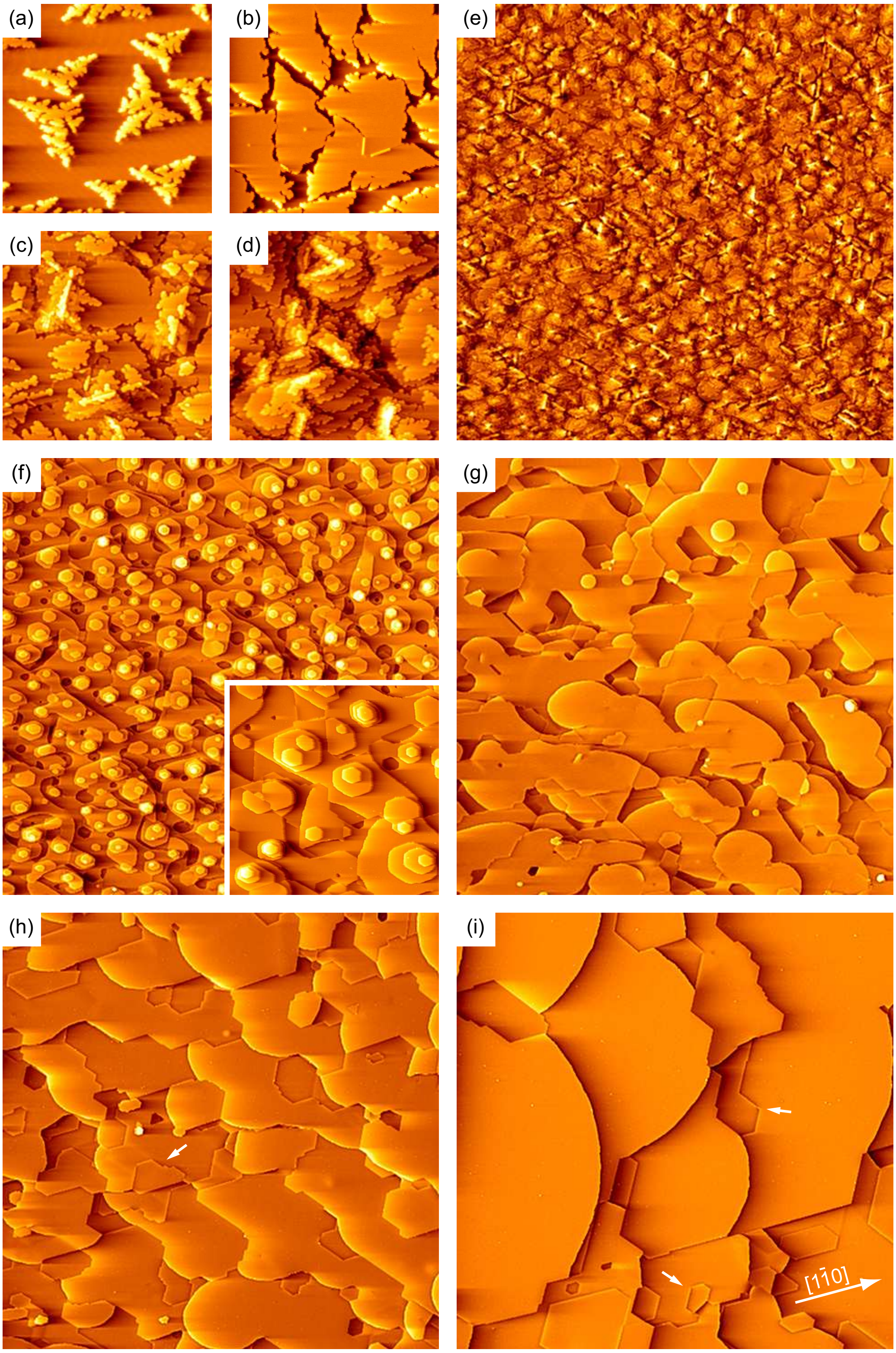
(a)
(b)
(c)
(d)
(e)
(f)
(g)
(h)
(i)
[1$\bar{1}$0]

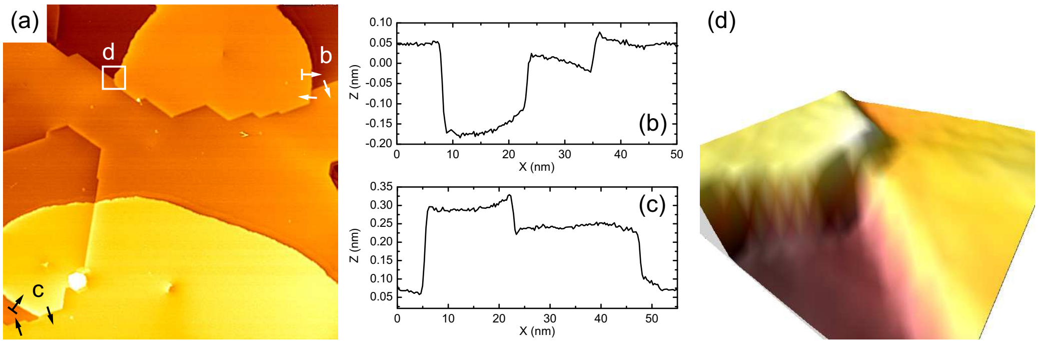

Figure 5.2: (a) Greyscale STM topograph after deposition of 90 ML film at 350 K and additional annealing t 1025 K for 180 s. Image size is 128 nm × 128 nm. (b), (c) Linescans along paths indicated in (a) illustrating full and fractional step heights as well as strain fields associated with fractional steps. (d) 3D-visualization of the junction marked in (a).

stacking[2]. In an isochronal annealing sequence with annealing intervals of 180 s this rough and heavily twinned film is subsequently heated to higher temperatures. In Fig. 5.1(f) after annealing to 850 K the film has become much smoother and the typical structure size has increased. Decoration rows or bright features oriented along $\langle 1\bar{1}0\rangle$ are now absent. After annealing to 1025 K (Fig. 5.1(g)) the film is very flat and the characteristic structure size is further increased. Straight steps precisely oriented along the $\langle 1\bar{1}0\rangle$ directions are visible. These straight steps have heights of only a fraction of a regular monatomic step. In addition, curved steps of monatomic height are visible. They are pinned where they touch fractional steps. The monatomic steps are invariably curved outward towards the downhill side. The outward curvature appears to imply an enhanced surface chemical potential, which for the case of Fig. 5.1(g) may be traced back to decaying adatom islands also visible. The last two annealing steps to 1200 K (Fig. 5.1(h)) and 1375 K (Fig. 5.1(i)) increase the typical structure size further, i.e. the step density decreases. The distinction between rounded monatomic steps and straight steps of fractional height is obvious. As indicated by arrows in Fig. 5.1(h) and (i) certain areas bounded by fractional steps are misoriented with respect to the global [111] orientation. This is apparent through twisted steps being partly up and

---

[2] Note that there are four possible stacking fcc stacking sequences, three with a fault underneath.

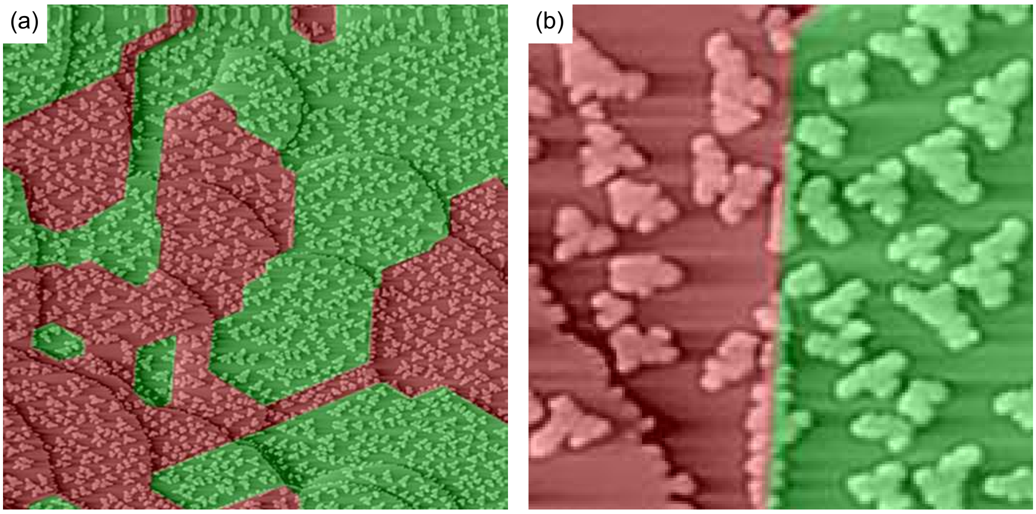

Figure 5.3: STM topographs after deposition of 90 ML at 350 K, subsequent annealing to 1200 K for 180 s and final 0.2 ML Ir deposition at room temperature. The predominant orientation of the triangular envelope of the small dendritic islands allows one to identify the stacking sequence of the underlying film. Regular stacked areas are shaded green, faulted areas are shaded red. Image sizes are (a) 255 nm × 255 nm and (b) 44 nm × 44 nm.

partly down steps which indicates the presence of dislocations in the film. The fact that even in Fig. 5.1(i), after the decay of all adatom islands, pinned monatomic steps are invariably curved outwards is possibly caused by less strongly bound atoms in the defect structures associated with the fractional steps. The defect structures define an enhanced chemical potential visible through the step curvature.

Fig. 5.2(a) shows a height image (not differentiated) of an area with straight (fractional) and curved (monatomic) steps in detail. Example line scans around the junction points marked with the arrows in (a) are shown in Fig. 5.2(b) and (c). The situation at a typical triple junction is depicted in a three dimensional view of Fig. 5.2(d). Neglecting for the moment heavily distorted areas, only three different kinds of steps are found: (i) steps with a height of 2.22 Å ± 0.17 Å, i.e steps with a height corresponding to the (111) layer distance of 2.22 Å; (ii) steps with a height of 0.74 Å ± 0.09 Å i.e. steps which display within the limits of error a fractional height of 1/3 of a monatomic step; (iii) steps with a height of 1.49 Å ± 0.24 Å i.e. steps which display within the limits of error a fractional height of 2/3 of a monatomic step (compare Fig. 5.2(b) and (c)). The measured step heights do not depend on tunneling voltage and are thus a topographic effect. Evidently, fractional steps cannot be present on the (111) surface of a perfect Ir crystal and their occurrence proves the presence of extended defect structures in the Ir film even after annealing to 1375 K (compare Fig. 5.1(i)). In the vicinity of the fractional steps, typically an upward (downward) bending of the upper (lower) terrace perpendicular to the step direction takes places. It extends over a distance of about 9 nm with a significant scatter and indicates the presence of strain next to the fractional steps.

A post decoration technique was employed to access the stacking of the surface areas of the Ir films after annealing [5]. 0.1-0.2 ML Ir were deposited on the annealed film surface at room temperature. Dendritic Ir islands with the characteristic triangular envelope grow, which display the same orientation in an area of uniform stacking with a preference of about 90%. Two areas of different stacking display consequently mirrored preferences of the triangular island envelopes. Application of the post decoration method to the surface after annealing at 1200 K is exemplified in Fig. 5.3. The areas have been marked depending on the stacking sequence identified. Using the post decoration method it is found that even after annealing to 1200 K more than 50% of the surface area of the 90 ML films is twinned with respect to the bulk crystal. This result is backed up by quantitative LEED I/V analysis.

As illustrated in Fig. 5.3(b), fractional steps separate areas of different stacking sequence. In fact, for an annealed film adjacent areas of different stacking are always separated by a fractional step. Thus fractional steps mark the lateral border of the differently stacked grains normal to the twin plane, i.e. they indicate the positions of incoherent twin boundaries. The orientation of the separating steps along the $\langle 1\bar{1}0\rangle$ direction together with their fractional height is important information to uncover the nature of the incoherent twin boundaries underneath the surface. One might speculate that {111} planes inclined by 70.51° to the (111) surface are involved in the formation of the incoherent twin boundaries, as the $\langle 1\bar{1}0\rangle$ directions are defined by the intersection of the surface (111) plane and a {111} side-facet. However, to understand the incoherent boundaries, more information is required by a method able to look underneath the surface.

5.1.2 SXRD Experiments

For the description of the crystal truncation rods (CTRs), the hexagonal coordinate system described in section 3.4.3 with h and k denoting the CTRs

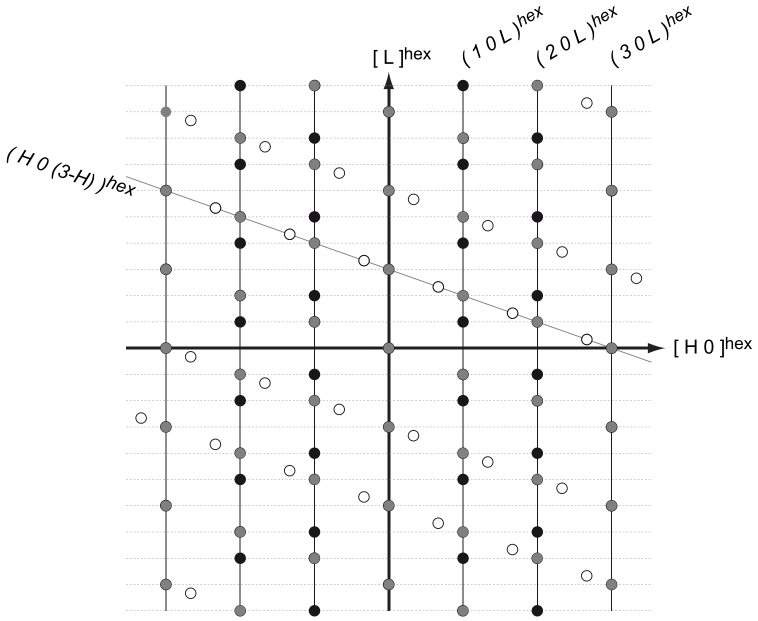

Figure 5.4: Map of the calculated peak positions at crystal truncation rods (CTR's) in the $[H0]^{hex}$ direction. Full circles: peak positions of regular stacked film patches. Grey circles: peak positions of twinned film patches. Open circles: peak positions resulting from twin on a {111} side-facet of a twinned crystallite.

in reciprocal coordinates and l being the momentum transfer perpendicular to the surface is used.

Figure. 5.4 displays a crystal truncation rod map along the $[H0]^{hex}$ direction. As indicated, the $(10L)^{hex}$ rod is expected to show intensity maxima at $L = \{1, 4, 7, ...\}$ for a regular crystallite and at $L = \{2, 5, 8, ...\}$ for a twin. Similar (not shown in the map), the $(01L)^{hex}$ rod is expected to display intensity maxima at $L = \{2, 5, 8, ...\}$ for a regular crystallite and at $L = \{1, 4, 7, ...\}$ for a twin. Therefore scans along these rods are well suited to measure the evolution of the stacking sequence, as has been previously reported by Camarero et al. for homoepitaxy on Cu(111) [3].

The $(10L)^{hex}$ and $(01L)^{hex}$ CTRs before and after deposition of 68 ML Ir at 350 K are shown in Fig. 5.5. The deposited amount was calibrated through the initial intensity oscillations at the anti-Bragg position $(11\frac{3}{2})^{hex}$. As expected, before Ir deposition a perfect single crystal is present without a trace of twinning. After deposition the peaks characteristic for twinning are

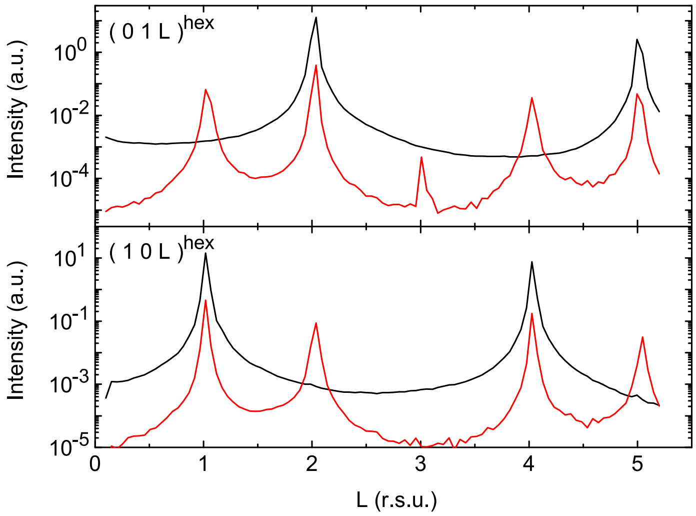

Figure 5.5: Scans of the $(10L)^{hex}$ and the $(01L)^{hex}$ CTRs on a {111} side-facet of a twinned crystallite before (black line) and after (red line) deposition of 68 ML Ir on Ir(111) at 350 K.

comparable in intensity to those of the untwinned crystal. In addition, for the $(01L)^{hex}$ CTR a new weak peak at $L = 3$ evolves. This peak at $L = 3$ is also present for other CTRs, though occasionally due to small intensities hard to observe. Its origin is not obvious and will be discussed below.

Fig. 5.6 displays the evolution of the integrated intensity of the $(01L)^{hex}$ CTR at $L = 1$, a position sensitive to twinning at the (111) plane. After deposition of about 10 ML the signal strongly rises. From STM experiments it is known, that after 10 ML the growth mode changes from layer-by-layer growth to rough growth dominated by heterogeneous nucleation at decoration rows (compare Fig. 5.1(c)) with rapid proliferation of stacking faults.

As speculated above, {111} planes inclined with respect to the surface (111) plane might be involved in the formation of the incoherent twin boundaries. These planes are oriented in the $\langle 111 \rangle$ directions and $\langle 115 \rangle$ directions for untwinned and twinned crystallites, respectively. These planes result from a rotation of $\pm 70.51°$ around the $< 1\bar{1}0 >$ directions. Translated into the hexagonal coordinate system for the SXRD measurements, one expects their first order CTRs to lie on e.g. $(\,H\,0\,(3-H)\,)^{hex}$, $(\,H\,0\,(3+H)\,)^{hex}$, $(\,0\,K\,(3-K)\,)^{hex}$, $(\,0\,K\,(3+K)\,)^{hex}$ or equivalent rods. This has been illustrated in Fig. 5.4 for one direction: The rotation transforms the $(10L)^{hex}$

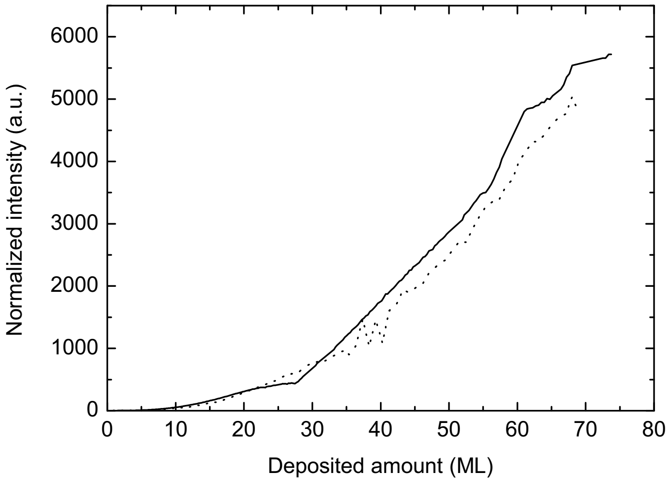

Figure 5.6: Integrated intensity at the $(011)^{hex}$ position of the $(01L)^{hex}$ CTR as a function of deposited amount for two growth runs. The intensity measures twinning with respect to the (111) plane. The intensity is normalized to the value prior to deposition.

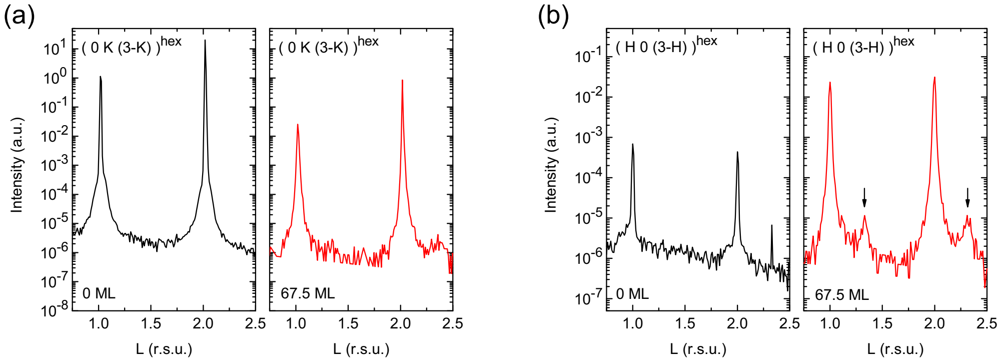

Figure 5.7: Scans along the (a) $(\,0\,K\,(3-K)\,)^{hex}$ and (b) $(\,H\,0\,(3-H)\,)^{hex}$ CTRs before (black line) and after (red line) deposition of 67.5 ML Ir on Ir(111) at 350 K. Arrows in (b) indicate new peaks (see text).

CTR into a $(\,H\,0\,(3-H)\,)^{hex}$.

In Fig. 5.7(a) scans along the $(\,0\,K\,(3-K)\,)^{hex}$ and in Fig. 5.7(b) along the $(\,H\,0\,(3-H)\,)^{hex}$ rods are shown. While only faint changes are measured in the $(\,0\,K\,(3-K)\,)^{hex}$ scan due to deposition, the $(\,H\,0\,(3-H)\,)^{hex}$ scan exhibits new peaks at $L=\frac{5}{3}$ and $L=\frac{7}{3}$ after deposition. The new peaks are indicated by arrows in Fig. 5.7(b). They appear at positions attributed to material twinned at the $\{111\}$ side-facets of twin crystallites, i.e. $\{111\}$ planes normal to $\langle 115\rangle$ directions. They do not appear at positions attributed to material twinned at the $\{111\}$ planes of regular crystallites, i.e. $\{111\}$ planes normal to $\langle 111\rangle$ directions.

5.1.3 Comparison

Fig. 5.8 compares the annealing temperature dependence of quantitative measures obtained from LEED and STM data with SXRD intensities. The black squares in Fig. 5.8(a) display the fraction of twinned surface area as a function of annealing temperature measured by LEED. It is around 0.6 up to 1025 K, then gradually drops but does not vanish even for the highest annealing temperature of 1400 K. The integrated intensity at $(011)^{hex}$ measured by SXRD and shown in Fig. 5.8(b) as black squares is also indicative of twinning with respect to the (111) surface plane, but measures not only the surface area but the amount of twinning in the film volume underneath the surface due to the finite integration depth of SXRD. The amount of twinning apparently does not change up to annealing temperatures of 1200 K and only then gradually decreases. Roughly, both data sets agree that (i) twins start to decay in the temperature range of 1000 K to 1200 K and that (ii) even the highest annealing temperature used is not sufficient to remove them entirely. The shift is attributed in the onset of twin annealing towards higher temperature in the SXRD data to the higher background pressure during Ir thin film deposition. In LEED annealing sequences it was noticed that this onset depends sensitively on the pressure during deposition. Most likely it is related to the incorporation of carbidic species from the background pressure which subsequently hinders annealing at higher temperatures.

The full dots (red) in Fig. 5.8(a) measure the length of the borders separating surface areas of different stacking sequence as obtained by STM. This length decreases rapidly upon annealing at temperatures well below the onset of healing of the twinned surface area (full black squares in Fig. 5.8(a)). Apparently both, twinned and untwinned areas become more compact (reducing side twin boundaries), and probably even grow in size through coalescence

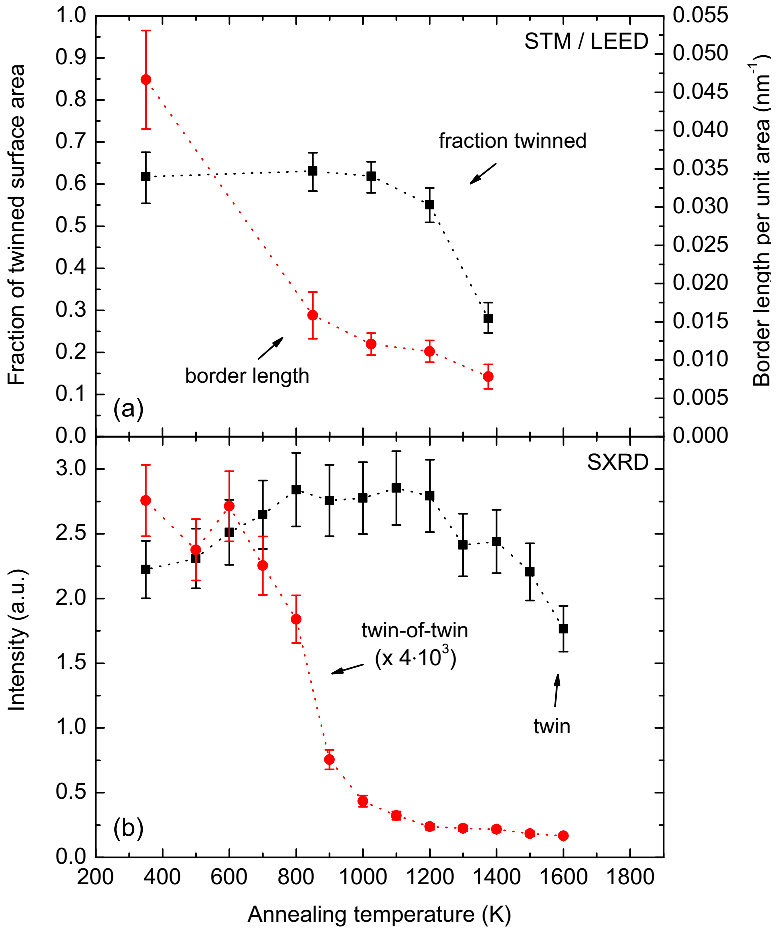

Figure 5.8: (a) Fraction of twinned surface area measured by LEED (black squares) and border length between differently stacked surface areas measured by STM (red circles) for a 90 ML Ir film grown on Ir(111) at 350 K. (b) Intensities at $(011)^{hex}$ (black squares) and $(\,2/3\,0\,7/3\,)^{hex}$ (red circles) as indicators for twinning with respect to the (111) surface plane and twinning on {111} side-facets of crystallites twinned with respect to the (111) surface plane, respectively. The 74 ML Ir film was grown at 350 K on Ir(111).

processes or preferential disappearance of small domains. Note that these processes take place without affecting the relative fractions of twinned and untwinned surface area. This is plausible, as the driving force to remove incoherent twin boundaries (separating laterally areas of different stacking) is much larger than the driving force to remove the coherent twin boundaries: grain boundary energies are much higher than stacking fault energies. The full red dots in Fig. 5.8(b) measure the SXRD intensity at $(\frac{2}{3}0\frac{7}{3})^{hex}$ during annealing. As discussed above, at this position in reciprocal space the twins on a $\{111\}$ side-facet of a twinned crystallite ("twin-of-twin") create intensity. The measured SXRD intensity displays a similar temperature dependence as the border length measured by STM. It decreases already around 700 K, at much lower temperatures than the twin intensity itself. It can therefore be concluded, that this intensity is linked to the incoherent twin boundaries separating patches of different stacking.

5.2 Discussion

The remaining task is to develop a picture of the twinned film consistent with the experimental results. It needs to account for the following facts: (i) The boundaries between areas of different stacking sequence are aligned along the $\langle 1\bar{1}0\rangle$ directions; (ii) They are separated by fractional steps of 1/3 or 2/3 height; (iii) Twins with respect to the $\{111\}$ side-facets of twin crystallites are linked to the boundaries between differently stacked regions, as the SXRD intensity at $(\frac{2}{3}0\frac{7}{3})^{hex}$ decreases with the boundary length between differently stacked surface areas; (iv) The weak peak at $L = 3$ evolving for the $(01L)^{hex}$ CTR during growth is explained by the proposed picture for film structure.

Key to such a picture is the nature of the incoherent twin boundaries. To discuss possible arrangements for such boundaries Fig. 5.9 is considered first. Fig. 5.9(a) displays a regular and a twinned crystallite bounded by (111) top facets and $\{111\}$ as well as $\{100\}$ side-facets. A cross section through the crystallites indicating the facets and their directions is shown in Fig. 5.9(b). Note that the directions given refer to the directions within the crystalline (untwinned) matrix. Therefore, the $[\bar{1}22]$ direction is not only normal to a $\{\bar{1}22\}$ side-facet of a regular crystallite, but also to a $\{100\}$ side-facet of a twinned crystallite. Figs. 5.9(c) and (d) sketch possible crystal plane combinations with low index planes forming incoherent twin boundaries. To embed a twin crystallite into a regular matrix (or a regular crystallite into a twinned matrix) one of the boundaries sketched in Fig. 5.9(c) and one

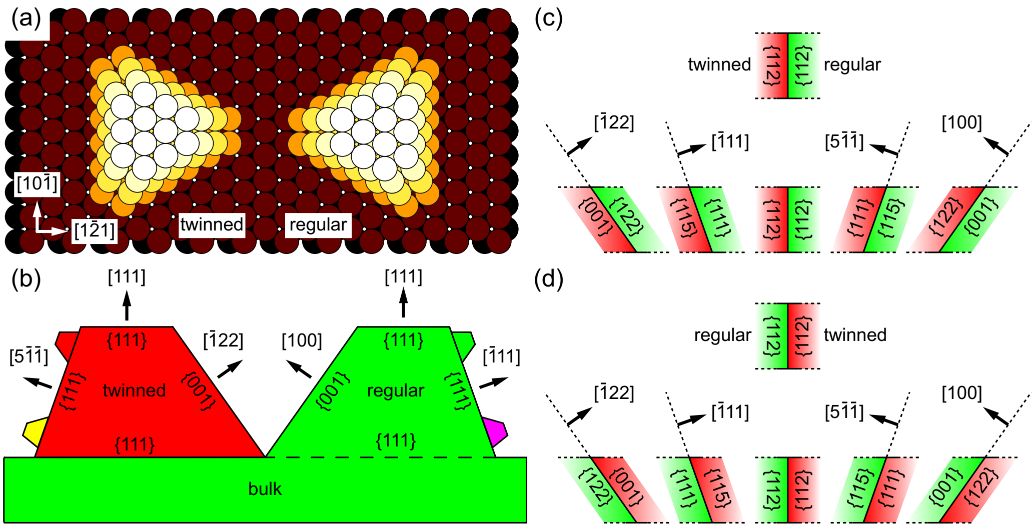
(a)
$[10\bar{1}]$
$[1\bar{2}1]$
twinned
regular
(b)
[111]
[111]
{111}
$[5\bar{1}\bar{1}]$
{111}
twinned
{001}
$[\bar{1}22]$
{111}
[100]
{001}
regular
{111}
$[\bar{1}11]$
{111}
bulk
(c)
twinned
{112}
{112}
regular
$[\bar{1}22]$
$[\bar{1}11]$
$[5\bar{1}\bar{1}]$
[100]
{001}
{122}
{115}
{111}
{112}
{112}
{111}
{115}
{122}
{001}
(d)
regular
{112}
{112}
twinned
$[\bar{1}22]$
$[\bar{1}11]$
$[5\bar{1}\bar{1}]$
[100]
{122}
{001}
{111}
{115}
{112}
{112}
{115}
{111}
{001}
{122}

Figure 5.9: (a) Ball model of a regular and a twinned crystallite bounded by (111) top facets and {111} as well as {100} side-facets. (b) Cross section depicting the facets and the corresponding orientations with respect to the regular crystal matrix. The purple and the yellow objects depict twins on the {111} side-facets of regular and twinned crystallites. (c),(d) Models of possible incoherent twin boundaries involving low index planes.

sketched in in Fig. 5.9(d) is necessary. The principal plane combinations are of the types {112}/{112}, {001}/{122} and {111}/{115}.

The {112}/{112} twin boundary is normal to the sample surface. As known from TEM investigations of other fcc metals, e.g. from Au [82], the {112}/{112} boundary leads to a partial dislocation of 1/2 [111] as shown in Fig. 5.10(b). This would result in a fractional step height of 1/2 monolayer in contradiction to the STM observation of 1/3 and 2/3 fractional steps.

In a {001}/{122} boundary, every third atom of the {122} facet is in contact with the {001} facet and rests in the fourfold coordinated sites formed by the atoms of the {001} facet (Fig. 5.10(c)). To make this possible, only a dislocation of $1/2 < 1\bar{1}0 >$, i.e. a dislocation along the surface plane, is necessary. The surfaces of the regular and twinned parts stay at the same height and thus this type of boundary is inconsistent with the observed partial step heights.

The {111}/{115} boundary (Fig. 5.10(d)) has one third of the atoms of the {115} plane in contact with the {111} facet. A slight dislocation along the

{111} facet makes the atoms in contact sit in threefold coordinated fault sites of the {111} facet and increases the density of this boundary considerably. This configuration involves characteristic steps of 1/3 or 2/3 of a monolayer step height. It is possible for the regular as well as the twinned {111} side-facets. The respective partial dislocations are, depending on the orientation of the boundary, of the type of $1/3 < 211 >$ or $1/3 < 255 >$, respectively.

The SXRD intensity for a {111}/{115} boundary with the {111} side-facet on the twinned side has been simulated[3]. The resulting intensity maps for a situation without and with an additional dislocation of type $1/3 < 211 >$ are shown in Fig. 5.11(a) and Fig. 5.11(b), respectively. If the twinned and untwinned crystal are displaced in height by 1/3 or 2/3 fractional steps, for all $(0KL)^{hex}$ and $(H0L)^{hex}$ CTRs a new peak at $L = 3$ appears due to the shift as observed in the experiments.

However, the {111}/{115} boundary does not cause new peaks in the $(H\,0\,(3-H))^{hex}$ or $(0\,K\,(3-K))^{hex}$ scans. These peaks can neither be explained by regular nor by twinned stacking or a combination of the two. They result from a third kind of structure which is be generated by rotating a part of a twinned crystal 70.51° around a $\langle 1\bar{1}0 \rangle$ axis. This stacking is equivalent to twinning a part of a crystal that has its coherent twin plane on (111) a second time on one of its own {111} side-facets, as shown in Fig. 5.10(e).

Although the structure shown in Fig. 5.10(e) explains the SXRD signal, the (111) facet of such a twinned domain would have a large inclination of 39° degrees with respect to the (111) facet of twinned and untwinned crystallites and thus the surface imaged in the STM topographs. Although the line scans over the fractional steps in the STM topographs show distortions, these distortions are small and inconsistent with large inclinations on the surface.

A solution consistent with the experimental data is the dissociation of the {111}/{115} boundary into {111}/{111} and {112}/{552} boundaries with a short {113}/{335} boundary at the bottom as sketched in Fig. 5.10(f).

Indeed, it is well documented that the {111}/{115} boundary is unstable and easily dissociates [83], often in {111}/{112} and {111}/{111} boundaries with the latter in the plane of the former {111}/{115} boundary. Energetically, the dissociation proposed is consistent with the available literature data. Wolf et al.[84] calculated for Cu the energy of a {111}/{111} bound-

---

[3] The simulations have been performed by Johann Coraux, present address Institut Néel, CNRS-UJF, 25 rue des Martyrs, BP166, F-38042 Grenoble Cedex 9, France.

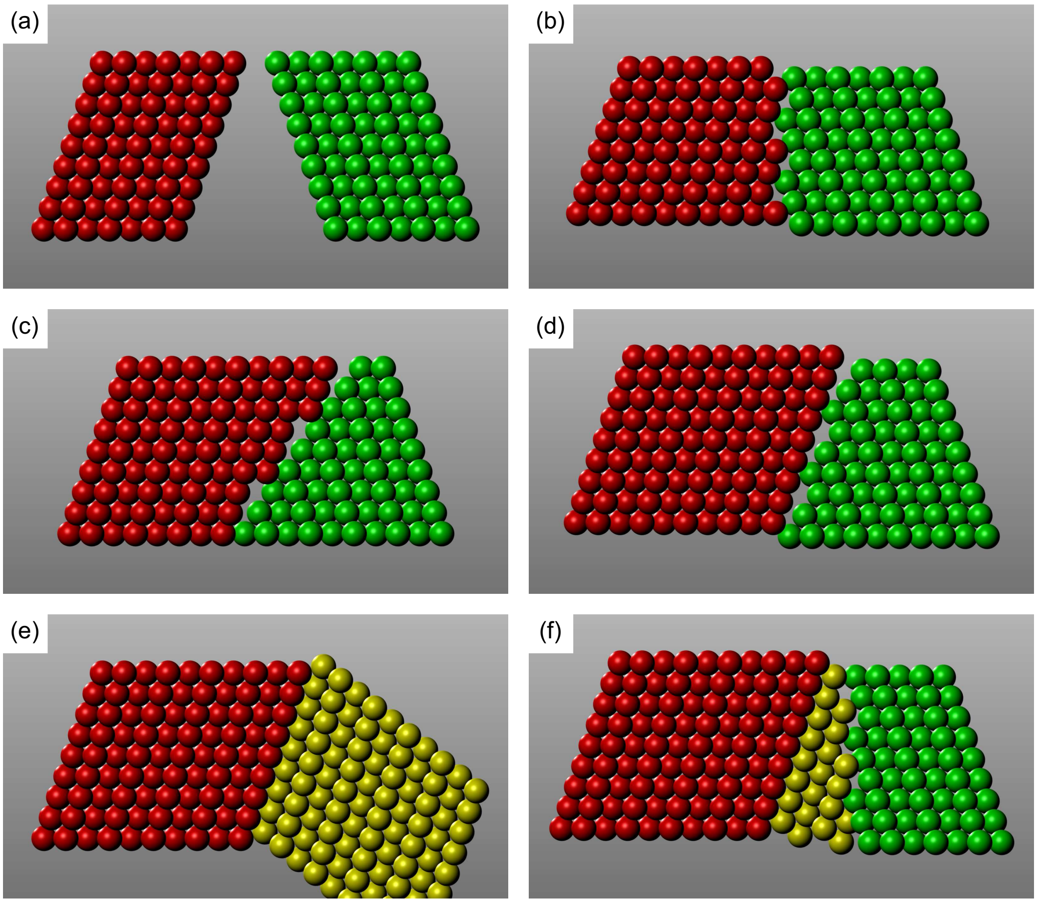

Figure 5.10: Ball models for incoherent high symmetry twin boundaries. (a) Orientation of the crystallites: (red/left) twinned, (green/right) untwinned. (b) Model of a {112} twin boundary with a partial dislocation 1/2 [111]. (c) Model of a {001}/{122} boundary with a partial dislocation of 1/2 $[1\bar{1}0]$. (d) Model of a {111}/{115} boundary with a partial dislocation of 1/3 [255]. (e) Model of a crystal (yellow) twinned to a twin crystal (red) at a {111} facet. (f) Final model for the incoherent twin boundary (see text).

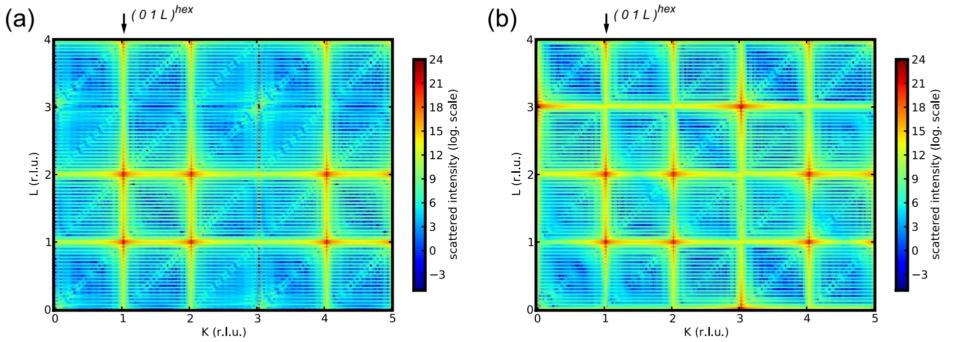

Figure 5.11: Intensity map for a {111}/{115} boundary between a regular and a twinned crystal of the same size, (a) without and (b) with a shift on the $\{11\bar{1}\}$ side-facet resulting in a height difference of 1/3 monolayers (see text).

ary to be 0.01 Jm^{-2}, of a {111}/{115} boundary to be 0.61 Jm^{-2} and of a {112}/{552} boundary to be 0.26 Jm^{-2}.

For the energy of the {113}/{335} an estimate on the basis of the data Fullman is possible [85, 86, 87]. The energy of a {113}/{335} boundary can be estimated to be about from 4-20 times the energy of a {111}/{111} boundary. Due to the energy gain by the formation of the {111}/{111} boundary and the short length of the {113}/{335} boundary energetically the entire dissociation still appears to be favorable.

Although the dissociated {111}/{115} structure is energetically more favorable than the undissociated one, it is still strongly inferior compared to the coherent (111) twin boundary. Therefore upon annealing the driving force to remove the dissociated {111}/{115} boundaries is much larger than the one for the removal of the coherent twin planes. Thus first the length and extension of the {111}/{115} boundaries diminishes through coarsening as observed by STM and SXRD, and only then, at higher temperature the twins are eventually removed. It stands to reason, that the removal of the twins taking place at about half of the melting temperature is itself linked to the onset of bulk diffusion through the onset of vacancy generation[4].

---

[4] No values are available for Ir bulk vacancy formation. The Pt bulk vacancy formation energy was determined to be $1.54 \pm 0.07\,\mathrm{eV}$ [88]. To give an estimate, scaling with respect to the cohesive energies ($E_{coh}^{Pt} = 5.86\,\mathrm{eV}$, $E_{coh}^{Ir} = 6.90\,\mathrm{eV}$ [89]) yields a value of 1.81 eV, i.e. bulk vacancy formation can be expected for temperatures above 1100 K.

5.3 Conclusion

During annealing of heavily twinned thin Ir films of Ir(111) first the length and extension of the boundaries separating areas of different stacking diminishes through coarsening at temperatures in the range of 800-1000 K. Only at much higher temperatures beyond 1200 K also the twins themselves heal. The two step annealing process is traced back to a difference in the driving force for healing: the boundaries between different stacking areas are energetically more costly than the coherent twin areas. The boundaries between different stacking areas are identified to consist of $\{111\}/\{115\}$ boundaries dissociated into coherent $\{111\}/\{111\}$ and $\{112\}/\{552\}$ boundaries. This transformation takes place on the $\{111\}$ side-facets. It involves the formation of a volume twinned with respect to twin crystallites. The proposed structure of the dissociated boundaries is consistent with the observed additional peaks in the the SXRD data and the observation of fraction step heights of 1/3 and 2/3 of a monolayer along $\langle 1\bar{1}0 \rangle$.

6 Suppression of Twin Crystallite Formation by Ion Beam Assisted Deposition

In chapter 4, it was shown that in homoepitaxial growth on Ir(111) at 350 K or below stacking fault islands develop in large number, displaying the Boltzmann distribution of the largest mobile cluster on regular and faulted sites. Through a number of additional mechanisms these faults are stabilized and even propagate during growth of multilayer thick films. Stacking faults and twin crystallites in thin films are highly undesirable, and kinetic strategies to suppress stacking fault nucleation and twin crystallite formation already during growth are needed.

In this chapter, homoepitaxy on Ir(111) at 350 K through physical vapor deposition without and with ion assistance is compared in a scanning tunneling microscopy study. Ion assistance with 100 eV Ar^+ at normal incidence as well as with 500 eV Ar^+ at grazing incidence both effectively suppress stacking fault formation and twinning in the growing film. The mechanisms of twin suppression are identified.

The results of this study have been also published in *Thin Solid Films* [90].

6.1 IBAD Strategies to Suppress Twinning

As in Ir(111) homoepitaxy twins form evidently for kinetic reasons this system appears ideally suited to test kinetic strategies for twin suppression and avoidance.

In a previous study, the influence of cluster mobility and stacking fault energy on the fault formation in homoepitaxy was investigated using a rate equation approach [44]. Not surprisingly, it was found that a large stacking fault energy per atom ΔE tends to diminish the formation of fault islands. However, equally important for the suppression of stacking faults is a large cluster mobility, i.e. the larger the size i in atoms of the largest mobile cluster at a given temperature, the smaller the ratio P of stacking fault islands to regular islands. The reason is simply that the ratio $\frac{P_{hcp}}{P_{fcc}}$ is to first approximation the Boltzmann distribution of the largest mobile cluster - with a total fault energy $i\Delta E$ - over the two types of adsorption sites:

$$\frac{P_{hcp}}{P_{fcc}} \approx e^{i\Delta E/k_B T} \tag{6.1}$$

This distribution is frozen during subsequent growth by addition of atoms to the mobile clusters becoming thereby immobile. The supply of additional energy to a growing film may be assumed to increase the mobility of small clusters athermally. Therefore energetic deposition or ion assistance appear to be methods with the potential to suppress stacking fault formation and ensuing twinning in thin film growth.

In this study, 100 eV Ar^+ ions at normal incidence with an ion to atom arrival ratio $R = 1:2$ and 500 eV Ar^+ ions at grazing incidence with an angle $\vartheta = 85°$ with respect to the surface normal and with $R = 1:10$ were used for ion assistance during deposition, thereby supplying the additional energy uniformly over the surface or especially at protruding objects, respectively.

Through ion erosion experiments (no simultaneous deposition) and subsequent scanning tunneling microscopy (STM) imaging the sputtering yield Y of 100 eV Ar^+ on Ir(111) at normal incidence was determined to be $Y = 0.1 \pm 0.01$ (see Fig. 6.1). In grazing incidence ion erosion it is necessary to distinguish between the terrace yield Y^{terr} and the step edge yield Y^{step} [91]. For 500 eV Ar^+ with $\vartheta = 85°$ the normal component of the kinetic energy $E_{\perp} = 3.8\,\text{eV}$ is not sufficient to induce damage or sputtering on terraces. The ions are specularly reflected. If, however, an ion hits directly or after a terrace reflection a step edge or a defect feature, a large angle scattering event with significant energy deposition takes place. To first order the corresponding Y^{step} is identical to the normal incidence yield [92], which is measured to be 1.2 ± 0.1. It should be emphasized here that in grazing incidence ion assistance energy is deposited only to illuminated steps or similarly protruding surface features.

6.2 Results

Figure 6.2 displays an overview of growth sequences obtained by physical vapor deposition (PVD) (Figs. 6.2(a)-6.2(d)), by IBAD with 100 eV Ar^+

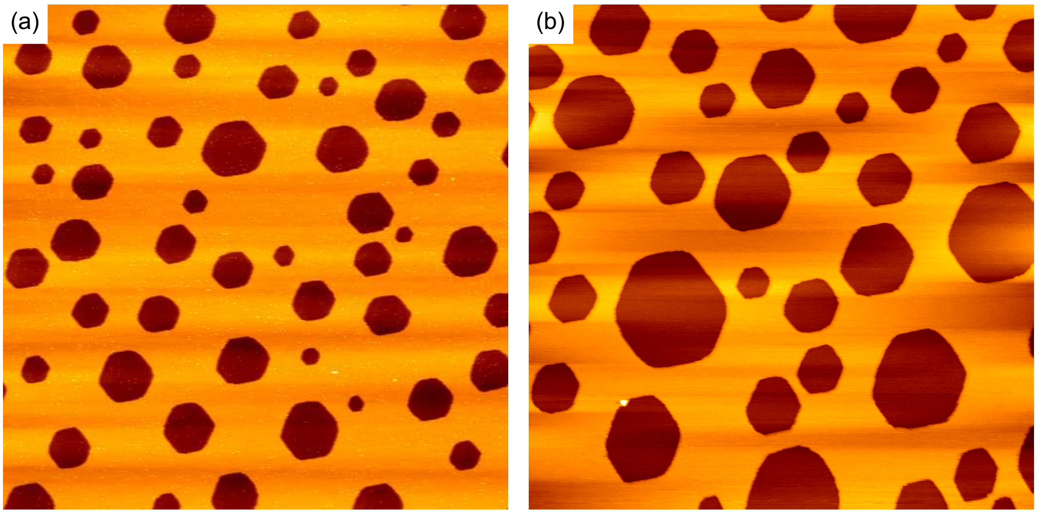

Figure 6.1: STM topographs of Ir(111) after sputtering of (a) 2 ML equivalents with 100 eV Ar^+ and (b) 0.3 ML equivalents with 500 eV Ar^+ at normal incidence and 350 K and subsequent annealing to 1100 K for 30s. Image size 325 nm × 325 nm.

ions at normal incidence (Figs. 6.2(e)-6.2(h)) and by IBAD with 500 eV Ar^+ at $\vartheta = 85°$ (Figs. 6.2(i)-6.2(k)).

The evolution of surface morphology for the PVD growth sequence is described in some detail first as a reference for the IBAD induced changes. Fig. 6.2(a) exhibits monolayer islands with a triangular envelope just before coalescence. While most of the island envelopes are oriented as indicated by the small white triangle in Fig. 1(a), some display an orientation rotated by 180° (or mirror orientation). These 11% of all islands are stacking fault islands as explained previously in the ball model of Fig. 4.3. The preference of Ir islands to develop {111}-microfacetted steps (or B-steps) implies the triangular island shape, which is rotated by 180° for islands nucleated on fault sites. Fig. 6.2(b) after 5 ML deposited displays four uncovered layers. Still growth appears to proceed close to layer-by-layer. However, a large number of thin white stripes - decoration rows - oriented along $\langle 110 \rangle$ is present, as also highlighted in magnified view in Fig. 6.2(l). When regular and fault islands come into close encounter, atoms move from the faulted area to the regular area, thereby diminishing the faulted area (self-healing, [8]). Self-healing terminates, however, when eventually faulted and unfaulted areas are separated by a gap consisting of {100}-microfacetted steps (an A gap, a gap formed by A-steps). As displayed in Fig. 4.3, such a gap displays fourfold coordinated stable adsorption sites and becomes decorated by Ir atoms forming a decoration row. While most of the decoration rows in Fig. 6.2(b) are of monatomic width, some are wider. In Fig. 6.2(c) after deposition of 20 ML layer-by-layer growth is clearly lost. A large number of wide decoration row features (significantly wider than an atomic row) are visible, many of them sit at the top of little mounds. A magnified view of such decoration row feature is shown in Fig. 6.2(m). Monatomic width decoration rows stabilize fault areas against healing in subsequent growth. They reappear in higher layers and become two and more layers wide. Decorations rows stabilize fault areas against unfaulting, induce new faults in the unfaulted surrounding and are sites of heterogeneous island nucleation (compare chapter 4). Eventually, after deposition of 90 ML as shown in Fig. 6.2(d) a rough, heterogenous surface develops. Mounds are present, which are mostly elongated along ⟨110⟩-directions with elongated broad decoration row features at their top. They are found at the mountain tops, as the disturbed elongated areas related to decoration rows are sites of heterogenous top layer island nucleation. These broad decoration rows not necessarily mark the separation between twinned and untwinned areas, but also the separation between areas with twins in different depth and thus with different stacking sequences. As shown in Fig. 6.3 in Ir PVD on Ir(111), after an initial delay the roughness σ increases rapidly with the deposited amount. Based on LEED and STM analysis, Fig. 6.4 displays the fraction θ_F of faulted surface area as a function of Θ. The initial oscillatory behavior of θ_F is due to stacking fault island nucleation and partial healing and thus due to faults underneath monolayer

Figure 6.2 : (facing page) (a)-(k) STM topographs of Ir(111) after deposition at 350 K. Left column: PVD; middle column: IBAD with 100 eV Ar^+ at normal incidence and $R = 1:2$; right column: IBAD with 500 eV Ar^+ at $\vartheta = 85°$ and $R = 1:10$. In the rows from top to bottom the deposited amount Θ increases from approx. 0.5 ML, 5 ML, 20 ML to 90 ML. The triangle in (a) indicates the orientation of a regular island and the arrow in (i) the direction of the ion beam. (l) Decoration row in magnified view after deposition 0.7 ML. (m) Decoration row derived elongated feature on a mound after deposition of 20 ML in magnified view. (n),(o) Mound grown by heterogeneous nucleation at decoration row structures after deposition of 70 ML and 90 ML. Image size in (a)-(k) 162 nm × 162 nm.

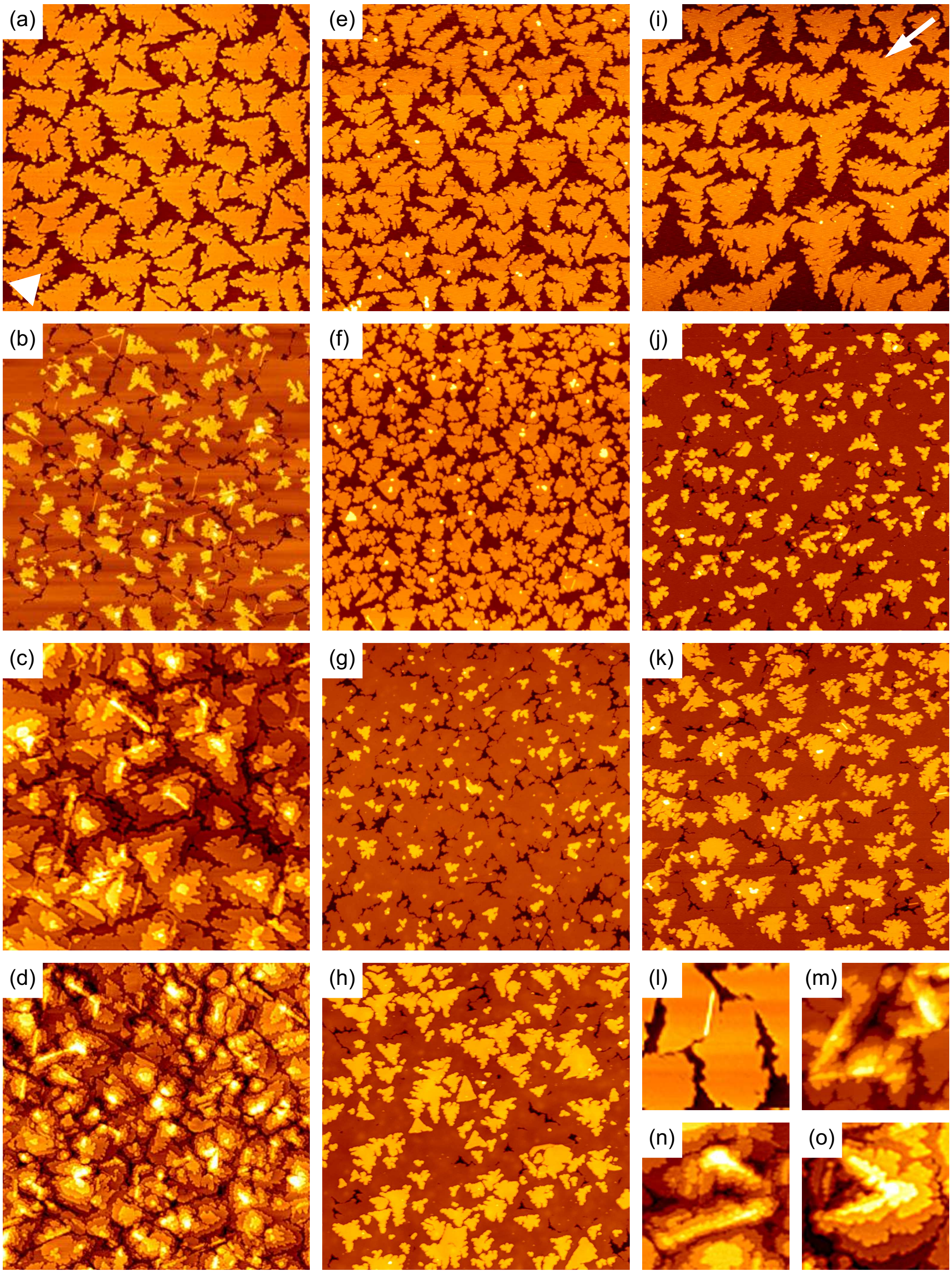
(a)
(e)
(i)
(b)
(f)
(j)
(c)
(g)
(k)
(d)
(h)
(l)
(m)
(n)
(o)

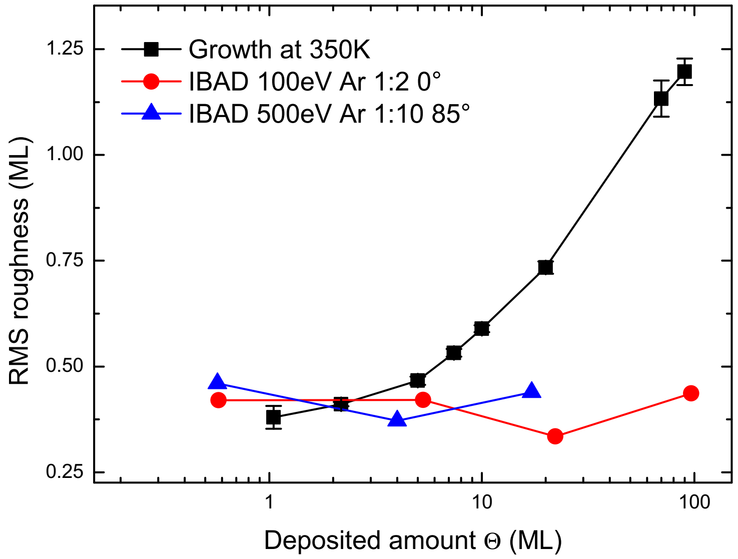

Figure 6.3: RMS roughness σ of PVD and IBAD films as function of deposited amount Θ.

islands. For the thick films, the faults are exclusively in deeper layer (i.e. due to twins), as heterogenous nucleation dominates, which is unable to change the stacking sequence.

Next, the IBAD growth sequence with 100 eV Ar^+ ions at normal incidence (Figs. 6.2(e)-6.2(h)) is considered. Figure 6.2(e) displays monolayer islands in slightly higher density as compared to Fig. 6.2(a). Compared to Fig. 6.2(a) the nucleation probability for a stacking fault island P_F has decreased from 11% to about 7% as shown in Fig. 6.4(b). Figure 6.2(f) after approximately 5 ML deposited displays only three layers uncovered and is therefore much closer to a layer-by-layer growth as the corresponding PVD morphology of Fig. 6.2(b). Compared to the PVD case number and length of decoration rows are considerably reduced. The total decoration row length per unit area λ_{DR} is marginal if compared to Fig. 6.2(b) and quantified in 6.5(a). After 20 ML deposited in Fig. 6.2(g) the morphological difference between PVD and IBAD is already remarkable. The IBAD morphology still displays only three uncovered layers characteristic for layer-by-layer growth with a very small roughness (compare Fig. 6.3). The quantities θ_F, P_F and λ_{DR} are all marginal compared to the PVD case (Fig. 6.4 and Fig. 6.5(a)). During the description of PVD it was pointed out that thicker decoration

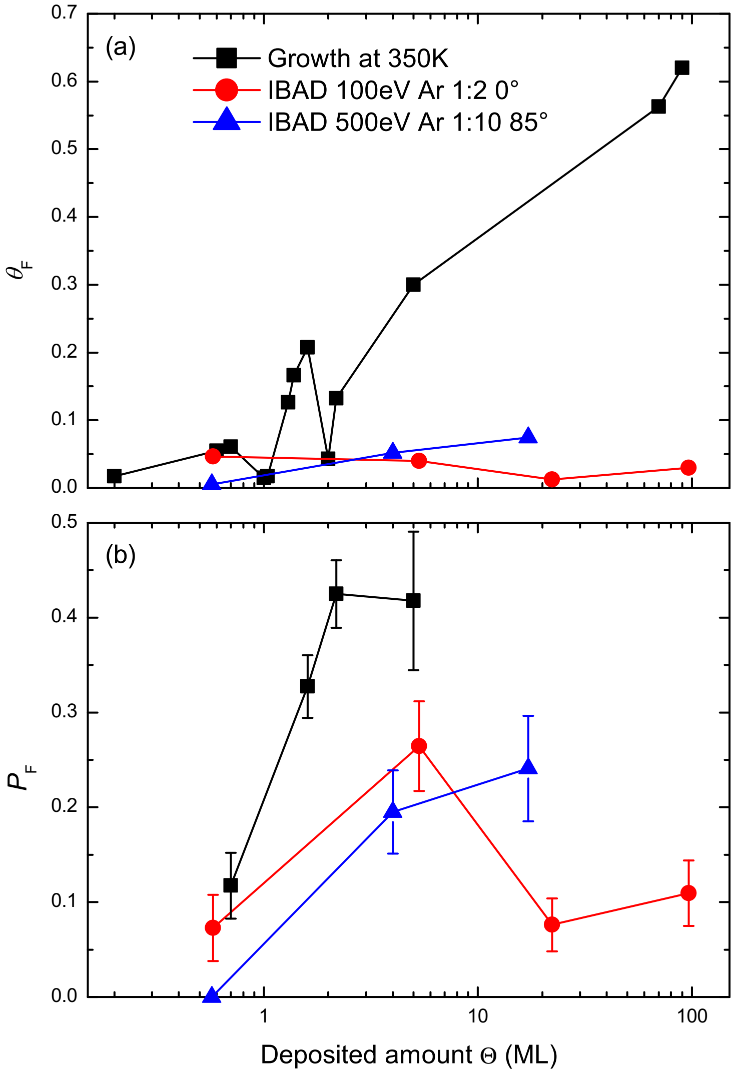

Figure 6.4: (a) Fraction of faulted surface area θ_F as function of deposited amount Θ. (b) Probability P_F for homogeneous nucleation of islands in stacking fault position as function of Θ. Note that no data are available for PVD with $\Theta > 10$ ML, as then nucleation is not more homogeneous.

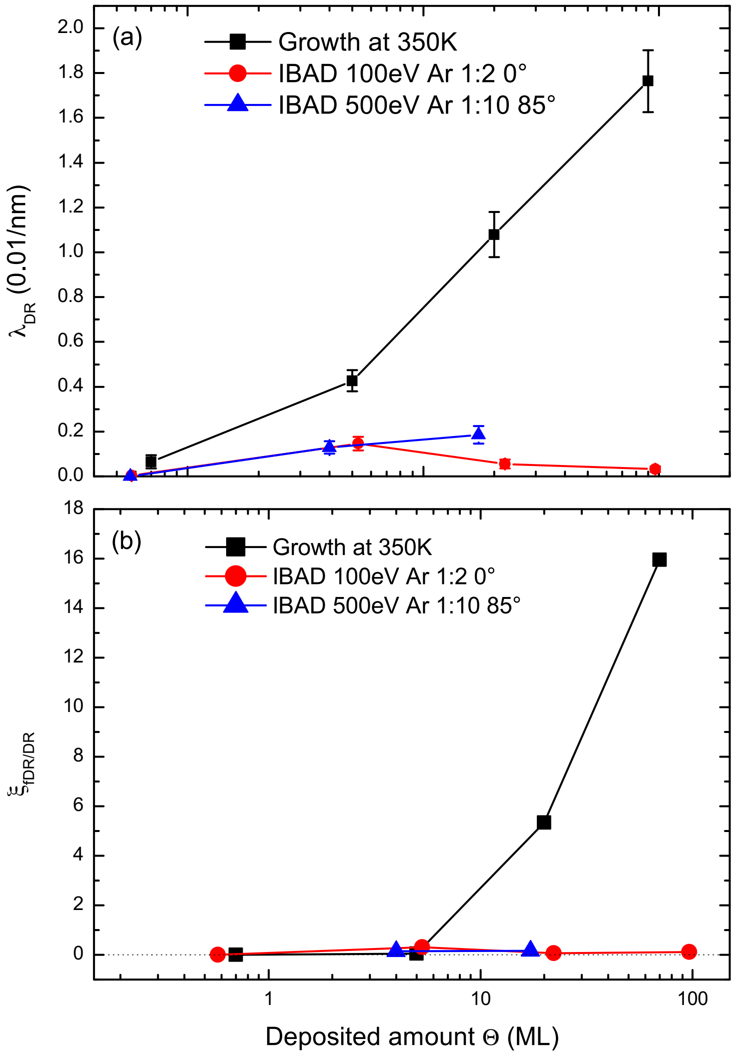

Figure 6.5: (a) Decoration row length per unit area λ_{DR} as a function of Θ. (b) Ratio $\xi_{\mathrm{fDR/DR}}$ of fat decoration rows and derived elongated structures to thin monoatomic width decoration rows.

rows or decoration row derived features are signatures of buried faults and thus of twins, i.e. of fault planes at least two layers below the surface[1]. Fig. 6.5(b) plots the ratio $\xi_{\mathrm{fDR/DR}}$ of fat decoration rows and derived elongated structures to thin monoatomic width decoration rows. While in PVD after 20 ML $\xi_{\mathrm{fDR/DR}}$ becomes appreciable, it is zero for IBAD after 20 ML. The evident conclusion is the absence of stacking faults in layers other than the topmost layer, i.e. the absence of twins. After IBAD of about 90 ML exemplified by Fig. 6.2(h), all key parameters remain similar to the 20 ML situation. Growth is stationary layer-by-layer with the indicators for faults and twinning σ, P_{F}, λ_{DR} and $\xi_{\mathrm{fDR/DR}}$ being small or zero (Figs. 6.3-6.5). However, as visible in Fig. 6.2(h), still monolayer stacking fault islands nucleate. P_{F} is about 11% even after 90 ML deposited. As conclusion it should be noted that although 100 eV Ar^+ IBAD at normal incidence is unable to hinder fault island formation, all faults formed are effectively removed through ion assistance before they become buried under the growing film.

Finally growth under influence of grazing incidence 500 eV Ar^+ ions visualized in the last column of Fig. 6.2 through (i)-(k) is discussed. Interestingly, while 100 eV Ar^+ IBAD enhanced the island density in the first layer, grazing 500 eV Ar^+ IBAD *decreases* the island number density significantly as visible in Fig. 1(i). Even more interesting is the complete absence of stacking fault islands in Fig. 6.2(i). However, after deposition of 5 ML and 20 ML in Figs. 6.2(j) and 6.2(k), respectively, stacking fault islands are present. Figs. 6.2(j) and 6.2(k) both display layer-by-layer growth, though after 20 ML deposited 4 layer are uncovered leading to a slightly larger roughness compared to IBAD with 100 eV Ar^+ (compare Fig. 6.3). Also the parameters θ_{F}, P_{F} and λ_{DR} are slightly inferior compared to the 100 eV Ar^+ case.

Consistent with the analysis above, the annealing behavior of the PVD and IBAD 90 ML films is very different. For the PVD grown 90 ML film represented by Fig. 6.2(d) and annealed for 180 s to 1025 K LEED and STM yield $\theta_{\mathrm{F}} = 0.62$ and $\theta_{\mathrm{F}} = 0.70$, respectively (compare Chapter 4). To the contrary, for the IBAD grown 90 ML film represented by Fig. 1(h) $\theta_{\mathrm{F}} = 0.03$. Fig. 6.6 visualizes the two annealed films in identical scale side by side. The hallmark of the presence of twin crystallites in the PVD film shown in Fig. 6.6(a) are the straight in $\langle 110 \rangle$-direction oriented steps, which are of only one third or two third fractional monostep height and separate regions of different stacking. The IBAD grown annealed film in Fig. 6.6(b) displays

---

[1] One talks of twins, if at least two layers above a stacking fault are properly stacked. The three topmost layers then define the stacking sequence of a twin crystallite.

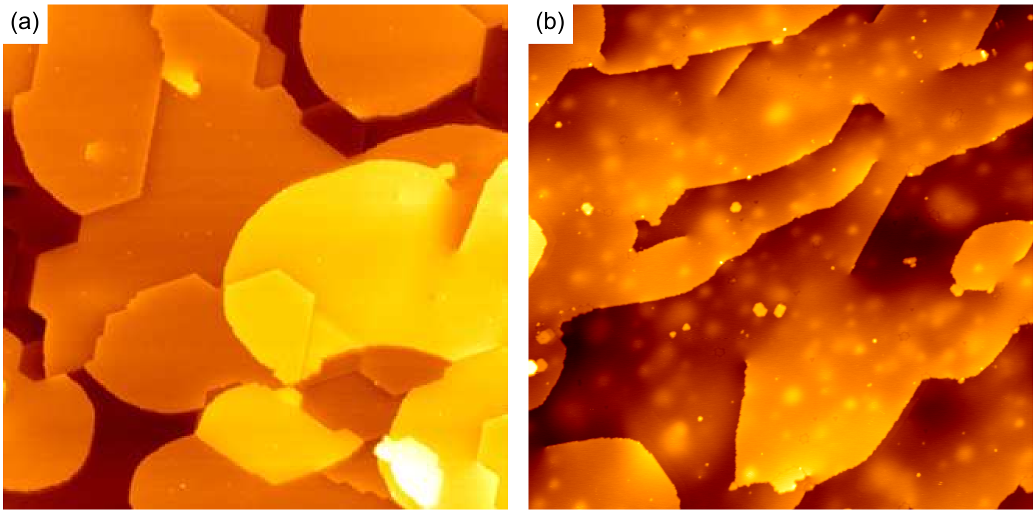

Figure 6.6: (a) 90 ML PVD grown Ir-film of Fig. 1(d) annealed for 180 s to 1025 K. (b) 90 ML IBAD grown Ir-film of Fig. 1(h) annealed for 180 s to 1025 K (see text). Image size is 162 x 162 nm.

only monolayer steps characteristic of an untwinned morphology. However, a significant number of intersection points of screw dislocations with the surface are visible together with bright bumps of subatomic height.

6.3 Discussion

Although the measurements largely confirm the concept that supply of additional energy during deposition suppresses fault and twin crystallite formation, still a number of issues need to be addressed here.

First the characteristic differences in the supply of energy to the surface for the two IBAD scenarios applied are considered. In grazing incidence IBAD with 500 eV Ar^+ very little energy is deposited to atoms in terraces. The normal component of the kinetic energy amounts to $E_\perp = 3.8$ eV and is insufficient to induce any damage. Normalized with $R = 1 : 10$, only 0.38 eV are supplied per arriving atom. However, this view is not appropriate for step atoms. An illuminated step atom may be hit either directly or after reflection by the terrace in front of the step atom. According to this geometrical model an illuminated step atom [91] receives a flux of atoms enhanced by a factor of $2\tan(\vartheta)$ compared to the terrace. The flux enhancement for $\vartheta = 85°$ amounts to a factor of 23. Moreover, as primary ions hit a step atom with a small impact parameter, large angle scattering events take place resulting in significant energy deposition and sputtering, comparable to normal incidence events with the same energy ($Y = 1.2$). Other illuminated, protruding surface features like decoration rows or adatoms are also subject to strongly enhanced flux and energy deposition. However, descending steps - if viewed in direction of the moving ion - are neither subject to flux enhancement nor enhanced energy deposition. Also ascending steps shadowed from the ion exposure (e.g. by islands and mounds) do not receive enhanced flux and energy deposition. Thus energy deposition in grazing incidence IBAD is anisotropic and highly localized to illuminated step atoms. In contrast, normal incidence IBAD with 100 eV Ar^+ dissipates isotropic and uniformly a supply of 50 eV energy per arriving atom.

Let us consider now the consequences of energy deposition for the nucleation stage. In the nucleation stage and for grazing incidence IBAD, nearly all deposited atoms (being adatoms or small adatom clusters) are illuminated by the ion beam. Taking into account the flux enhancement factor of 23 and the ion to atom arrival ratio of $R = 1 : 10$ in this early stage, the deposited atoms will be exposed to an average of 2.3 ions each carrying an energy of 500 eV. Evidently nucleation will be diminished by sputtering and every cluster that eventually survives will have been destroyed and reassembled many times. Thus even if a small cluster nucleated as a stacking fault one, during subsequent growth it will be energized many times allowing it to switch to regular sites. As clusters of size seven already prefer regular sites by 0.2 eV, only regular islands will be formed. These considerations explain the absence of fault islands in Fig. 6.2(i). If one considers now normal incidence 100 eV IBAD, as the energy deposition is uniform over the entire surface and not focused to the protruding adatoms and adatom clusters, a much smaller amount of energy per deposited atom is delivered: taking the estimates above it is a factor of 23 less. Thus small adatom clusters may be formed on fault sites. As the probability for a hit by an ion is much smaller and additionally a single hit delivers much less energy, chances are high that fault clusters manage to grow to large metastable sizes. Therefore Fig. 6.2(e) still displays a sizable fraction of fault islands. A 100 eV ion has sufficient energy to create adatom vacancy pairs and even adatom dimers, thereby enhancing the rate of island formation [64]. This ion beam induced adatom and adatom cluster production results in the enhanced island number density observed in Fig. 6.2(e).

A second phenomenon to be discussed is the increase of P_{F} with the deposited amount as visible in Fig. 6.4(b). This increase is observed for PVD and both IBAD methods. For PVD there is evidence that the presence of step edges dramatically enhances P_{F}. One likely scenario is the trapping of adatoms or small adatom clusters at step edges with strong energetic preference for fault sites. Possibly this step effect is strong enough to survive even under IBAD conditions. For the grazing incidence IBAD scenario one also has to take into account that the nucleation phase at the beginning of the growth of each layer is more dephased in higher layers, making shadowing of fault clusters possible.

Third it needs to be discussed why no faults are incorporated into the growing film to form twins although fault islands nucleate. The situation is most striking for IBAD with 100 eV Ar^+ normal incidence ions, which exhibits even after 90 ML deposited $P_{\mathrm{F}} = 11\%$ (compare Fig. 4(b)) but zero twins, i.e. buried stacking faults. It was already pointed out during the discussion of PVD growth that during layer closure upon close encounter of faulted and unfaulted areas a large amount of the faulted area transforms to regular area by motion of atoms over the little separating gap [49]. This self-healing terminates only through the formation of stabilizing decoration rows. In 100 eV normal incidence IBAD terrace atoms are subject to a high density of ion hits with significant energy deposition. Stabilizing decoration rows are therefore many times disturbed and destroyed, such that self-healing will become much more efficient. This is consistent with the normalized decoration row density λ_{DR} being smaller by about a factor of 55 for normal incidence 100 eV Ar^+ IBAD. Even if a fault would be overgrown and become buried two layers below the surface, still the hammering action of the 100 eV ions hitting the surface with high density would likely lift the fault. Energy deposition in grazing incidence IBAD is less homogeneous. Although illuminated decoration rows will be efficiently removed by flux enhancement and large angle scattering events with significant energy deposition, decoration rows in the shadow of islands are hardly affected. This makes it plausible that grazing incidence IBAD is slightly less efficient in twin suppression.

Finally the striking morphology of Fig. 6.6(b) observed after annealing a 100 eV Ar^+ normal incidence IBAD film exhibiting screw dislocations and bumps needs to be addressed. The same features were observed already after He^+ ion implantation [93]. Implanted noble gas is insoluble in metals and thereby precipitates in the form of small overpressurized gas bubbles. Annealing causes the gas bubbles to coalesce, grow in size and deform the lattice giving rise to step dipoles. Apparently also during 100 eV normal incidence IBAD Ar is incorporated in large amount into the growing film. For practical applications the energy supplied to the growing film should therefore come with the depositing particles themselves, thereby avoiding incorporation of foreign particles into the growing film. Based on the experiments an average Ir atom energy of 50 eV should be high enough to grow completely untwinned films of high structural quality.

6.4 Conclusion

Stacking fault and twin formation due to limitations in growth kinetics of Ir on Ir(111) can be effectively lifted by supply of additional energy of the order of 50 eV per deposited atom to the growing film. It must be assumed that the same beneficial suppression of twinning by the additional energy is also realized in other growth systems. Low energy normal incidence IBAD has been shown to lead to superior results compared to grazing incidence IBAD. However, for normal incidence IBAD noble gas implantation takes place, potentially degrading the structural quality of the films. Therefore energizing the depositing particles themselves must be assumed to be the method of choice to obtain structurally perfect films free of twins and precipitates.

7 Effect of Adsorbates on Twin Crystallite Formation

Adsorbates and surfactants are known to influence the various processes of diffusion, and thus have a major impact on the growth. Adsorbates usually decrease the mobility on the surface and lead to an increase in the island number density during growth [94]. By increasing the interlayer transport, layer-by-layer growth was induced using oxygen as adsorbate in homoepitaxy of Pt/Pt(111) [95] and Sb as surfactant in Ag/Ag(111) [96]. Surfactants have also shown their ability to suppress twin formation. Using In as surfactant in homoepitaxy of Cu/Cu(111) [2] and Pb in the growth of Co/Cu superlattices on Cu(111) [10], the formation of twins was effectively suppressed.

In this chapter, the results of the investigations on the influence of carbon monoxide and oxygen during the growth of Ir/Ir(111) are presented. CO is commonly found as contamination in vacuum systems, especially during deposition, and can have a severe influence on the growth. Oxygen is known to react with and remove CO during deposition [95], and might offer possibilities to counter CO contamination. As oxygen prefers to bind to only one kind of adsorption sites, namely the fcc sites, it might also be able to influence the formation of stacking faults.

7.1 Adsorbates Used and Their Adsorption Sites

CO is at room temperature mobile on the surface. The diffusion barrier is 0.43 eV [97]. On Ir(111), CO is bound to on-top positions [98] and forms at 1.5 L-2.5 L a $(\sqrt{3} \times \sqrt{3})$R30° superstructure with 30% of a ML coverage [99]. At room temperature, CO has a sticking probability of 60% [99]. At 620 K, CO is completely desorbed.

Atomic oxygen is created by exposure of the Ir surface to O_2, as O_2 adsorbs dissociatively at the Ir surface [100, 101]. O is at room temperature mobile

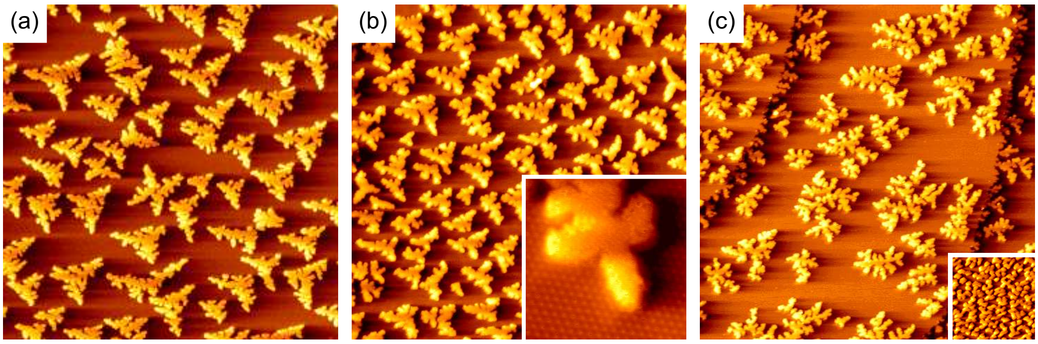

Figure 7.1: STM topographs after deposition of 0.2 ML Ir on Ir(111) at 350 K with and without adsorbates. (a) Without adsorbates. (b) With 6 L CO. Inset: CO superstructure (magnified). (c) After exposure to $1.1 \cdot 10^{-3}$ L O. The inset shows the increased island number density for exposure to 0.38 L O. Image size is 120 nm × 120 nm. Modified from [104].

on the Ir surface. The diffusion barrier is 0.55 eV [97]. O is bound to fcc sites and forms a $p(2 \times 2)$ or three 120° rotated $p(1 \times 2)$ superstructures [100]. Recent DFT calculations [101] indicate that the latter is realized. This is supported by the fact that the amount of oxygen in this superstructure is in agreement with the oxygen coverage measured in earlier XPS investigations [102, 103]. O has at room temperature a sticking coefficient of 4% [99]. At 1270 K, O is completely desorbed.

7.2 Results and Discussion

The experiments are based on previous experiments on the nucleation of Ir/Ir(111) in the presence of preabsorbed CO and O [104]. Fig. 7.1 shows STM topographs of the Ir(111) surface after deposition of 0.2 ML with and without preabsorbed adsorbates.

In Fig. 7.1(b), Ir was deposited after exposure of the surface to 6 L CO. Although the $(\sqrt{3} \times \sqrt{3})$R30° superstructure is formed and the surface is nearly completely covered, the islands still exhibit the typical shape. The island number density is increased by a factor of 2.4 ± 0.2 compared to the reference experiment without adsorbates shown in Fig. 7.1(a), indicating a higher barrier for diffusion. The stacking fault probability $P_{SF} = 0.08 \pm 0.03$ is slightly lower, but within the limits of error identical. In relation with the high amount of adsorbed CO, the changes appear moderate and manifest themselves only in the increased island number density.

The influence of O is more pronounced: Fig. 7.1(c) shows the surface after exposure to $1.1 \cdot 10^{-3}$ L O and subsequent deposition. Both island shape and island density changed. The islands are dendritic without any obviously preferred orientation. The island density is increased by a factor of 2.4 ± 0.5. Higher amounts of adsorbates even lead to higher island densities and stronger modifications of the island shapes (compare the inset in Fig. 7.1(c)). As the islands exhibit a dendritic shape without any preferred orientation, the stacking sequence is not accessible by STM.

CO is not only part of the background pressure. It is also often generated by hot filaments and during the use of many common types of evaporators. To simulate unclean evaporation conditions and to counter CO contamination by offering oxygen, the sample was exposed to a constant pressure of CO or O_2 during deposition. For experimental reasons, the exposure was started after deposition of 0.8 ML Ir. The rate Z of atoms with mass m arriving at a surface under a partial pressure p and a temperature T is given by

$$Z = \frac{p}{\sqrt{2\pi m k_B T}} \tag{7.1}$$

[35]. With respect to a deposition rate of $6.7 \cdot 10^{-3}$ ML/s and the sticking coefficient of 0.6, a partial pressure of $6.6 \cdot 10^{-9}$ mbar CO was chosen to achieve an Ir to CO arrival ratio of 1:10. Due to the strong influence of O, a much lower ratio was chosen whilst at the same time offering enough O to react with any CO that absorbed from the background pressure during the experiment[1]. $3.7 \cdot 10^{-9}$ mbar O were chosen resulting in an Ir to O arrival ratio at the surface of 1:140.

In all experiments, 50 ML Ir were deposited on Ir(111) at 350K. The results are shown in Fig. 7.2. Figs. 7.2(a) and (b) show an experiment without adsorbates. The typical morphology consisting of triangular pyramids and overgrown decoration row structures can be seen. In Figs. 7.2(c) and (d) the surface after deposition with CO is shown. The surface consists of a mound structure. The shape of the mounds is not uniform, but the sizes are similar. The mounds are separated by deep groves. No decoration row structures are seen. After deposition of 50 ML in the presence of O, the surface is again covered with mounds. Although the mound shape is not uniform, the mounds often have triangular shapes, and the mounds are larger than in the

---

[1] The pressure during deposition is well below $1 \cdot 10^{-10}$ mbar and consists to a large part of CO.

	RMS roughness (nm)	structure size (nm)	object density (10^{-3}/nm^2)	θ_F
clean	0.24 ± 0.03	40.7 ± 1.3	(2.8 ± 0.2)	
with CO	0.46 ± 0.05	18.2 ± 0.8	10.5 ± 0.7	0.52 ± 0.08
with O_2	0.49 ± 0.02	26.9 ± 1.5	5.2 ± 0.5	0.49 ± 0.09

Table 7.1: Results of the quantitative analysis of 50 ML Ir/Ir(111) grown with and without adsorbates. The object density for the case without adsorbates is the value for the island number density after deposition of 0.2 ML and is given for comparison only.

experiments with CO. In both cases, the tops of the mounds are often flat and separated by steep trenches, forming columnar structures.

Quantitative analysis reveals that the RMS roughness is in both adsorbate experiments increased by a factor of two compared to the experiment without adsorbates. The STM tip is not able to pass down steep trenches. It is probable that the trenches are deeper than measured and even lead down to the substrate, and the roughness is underestimated. The structure size is in both adsorbate experiments decreased to the reference experiment: The reference experiment exhibits a structure size of 40.7 ± 1.3 nm compared to 26.9 ± 1.5 nm for the O and 18.2 ± 0.8 nm for the CO experiment. This is also reflected in the object density, which is a factor of two higher for the experiments with CO than for the experiments with O. Both films are nearly half twinned: The film grown with CO is about 52% and the film grown with O is about 49% twinned.[2]

Deep trenches separate both mounds with different as well as the same

---

[2] Only objects that could be identified unambiguously were used for the STM analysis of θ_F. The LEED I/V analysis exhibits a value of $\theta_F = 0.557$ for CO, which is – within the limits of error – in good agreement with the results of the STM analysis, but the quality of the fits is not sufficient to allow a precise calculation.

Figure 7.2 : (facing page) STM topographs after deposition of 50 ML Ir on Ir(111) at 350 K with and without adsorbates. (a),(b) Without adsorbates. (c),(d) With CO. (e),(f) With O_2. The inset in (e) shows a stacking fault in the top layer in magnified view with enhanced contrast. Image size is 160 nm × 160 nm in (a), (c), (e) and 315 nm × 315 nm in (b), (d), (f).

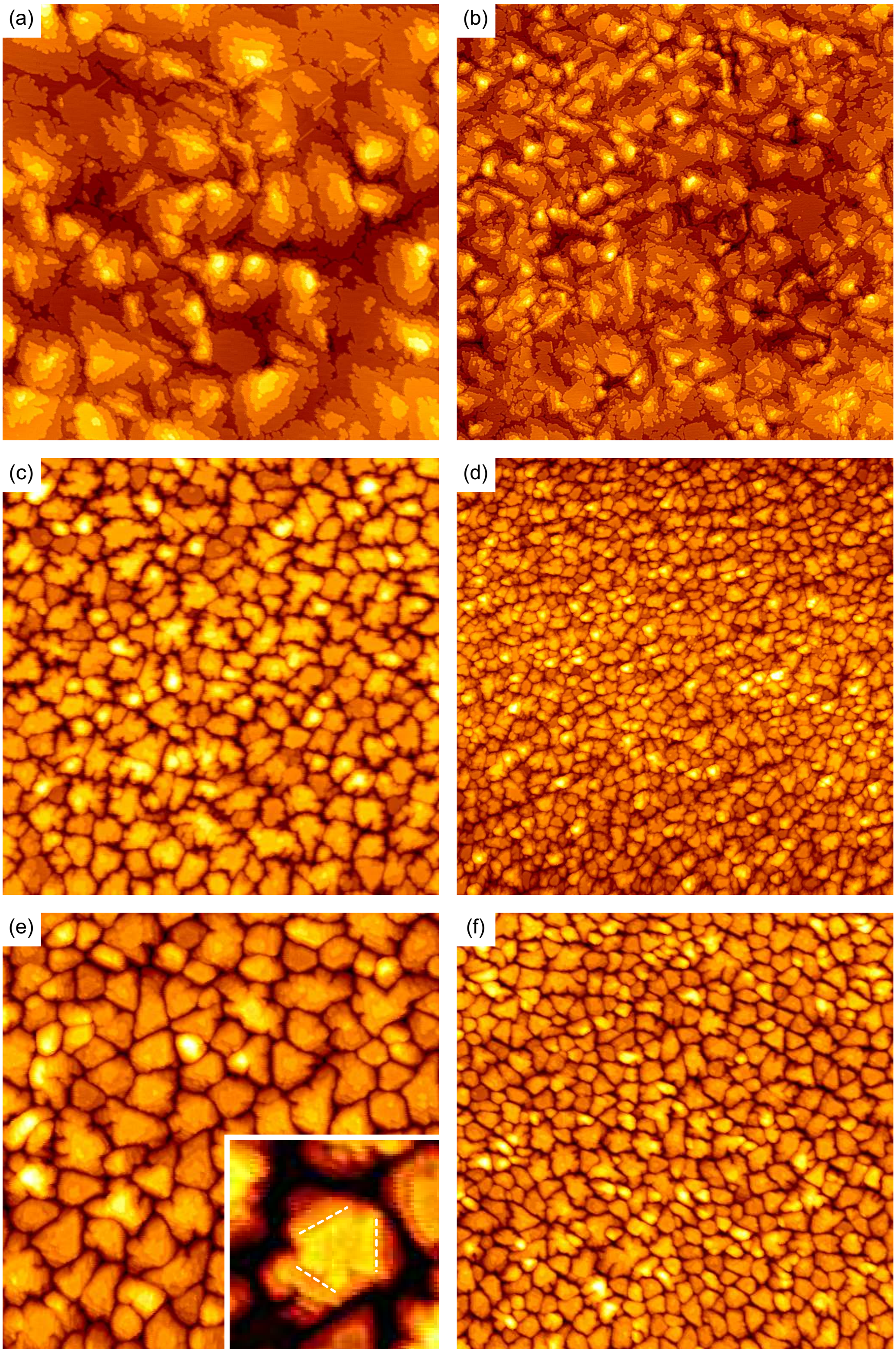
(a)
(b)
(c)
(d)
(e)
(f)

triangular orientation. The obvious lack of decoration rows combined with the much smaller structure size indicates that neither self-healing nor significant coalescence takes place. Iridium has a negative Ehrlich-Schwoebel barrier [37], and coalescence is expected. The adsorbates seem to stabilize the boundary between objects close to coalescence, not only between objects of different stacking. As a result, no coalescence and no self-healing, but columnar growth takes place, and the mound density should reflect the initial island density.

The inset in Figs. 7.2(e) shows a stacking fault in the topmost layer. As the previous experiments with preabsorbed CO showed, the stacking fault probability is nearly unchanged by the adsorbates, and the twinning of about 50% of the surface area can not be explained by an increased stacking fault probability. The columns do not only exist in either regular or twinned stacking, but often change the stacking sequence. The toy model presented in Chapter 4 appears to be applicable for this columnar growth, and in fact for both adsorbate experiments values of about 50% twinned surface area are measured as predicted by the model.

With respect to these results, the increased object density can be linked to an increased initial island number density. The increase is probably attributed to a reduced mobility caused by the adsorbates [94, 95].

7.3 Conclusion

In conclusion, it was found that CO and O prevent coalescence and self healing, and lead to columnar growth. Due to multiple twinning, the surface becomes 50% twinned for a large number of deposited layers. Both adsorbates reduce the mobility on the surface and lead to an increased island number density.

8 Summary

In the scope of the present thesis, the growth and annealing behavior of thin Iridium films on Ir(111) was studied by means of scanning tunneling microscopy (STM), low energy electron diffraction (LEED) and surface X-ray diffraction (SXRD). The influence of ion beam assisted deposition (IBAD) and adsorbates on the growth has been investigated.

Homoepitaxial thin films of Ir/Ir(111) have been grown in a range of 0.2 ML to 90 ML at 350 K with a standard deposition rate of 1.3×10^{-2} ML/s, where 1 ML (monolayer) is the surface atomic density of Ir(111). In the first layer, 11% of the islands formed are stacking fault islands. Upon coalescence, they become partially converted to regular stacking by a self-healing effect [49]. At the remaining phase boundaries between regular and faulted areas, thin monoatomic decoration rows are formed. It was found that by heterogeneous nucleation at the decoration rows and the energetic avoidance of intrinsic stacking faults, further stacking fault islands are formed that cause spread of the initial fault areas into their surroundings (proliferation effect). Replication of decoration rows in higher layers acting as nucleation centers and suppression of new fault formation next to them leads to a transition from layer-by-layer growth to a defect dominated growth with a fixed length scale. During this transition, the majority of the surface area becomes twinned. A step-influenced enhancement of the stacking fault probability initially supports the effect.

By the supply of additional energy in the order of 50 eV per deposited atom using IBAD stacking fault and twin formation can be effectively lifted. Grazing incidence IBAD leads to the complete suppression of stacking fault formation in the first layer, but the energy deposition is highly anisotropic and highly localized to illuminated step atoms and thus looses rapidly its effectivity during growth. Low energy normal incidence IBAD has been shown to lead to superior results compared to grazing incidence IBAD. The energy is distributed uniformly over the surface. Although the formation of stacking faults is not completely suppressed, the deposition of additional energy to the surface leads to a promotion of the self-healing effect and nearly defect free films. However, for normal incidence IBAD noble gas implantation takes place, potentially degrading the structural quality of the films. Therefore energizing the depositing particles themselves must be assumed to be the method of choice to obtain structurally perfect films free of twins and precipitates.

The annealing behavior of strongly twinned Ir films was investigated using thin films grown at 350 K. The investigation revealed a two step process: In a first step, the length and extension of boundaries separating areas of different stacking diminishes at temperatures 800 K-1000 K. At much higher temperatures beyond 1200 K also the twins heal in a second step. The two step annealing process is traced back to a difference in the driving force for healing: The boundaries between different stacking areas are energetically more costly than the coherent twin areas. The boundaries between different stacking areas are identified to consist of $\{111\}/\{115\}$ boundaries dissociated into coherent $\{111\}/\{111\}$ and $\{112\}/\{552\}$ boundaries. Structure models for the dissociated boundaries were given that are consistent with the fractional step of 1/3 and 2/3 of a monolayer along $<1\bar{1}0>$ heights observed in STM. Simulations of the SXRD intensities for the proposed model are in agreement with the measurements and explain new features observed in the SXRD measurements.

The influence of adsorbates on the growth of Ir/Ir(111) was studied for CO and O. It was found that exposure of the sample to CO or O during deposition prevents coalescence and self-healing of the film, and leads to columnar growth. Due to multiple twinning, the surface becomes 50% twinned. For both adsorbates, the island number density is increased, indicating a reduced mobility on the surface.

Bibliography

[1] M. J. Stowell. *Epitaxial Growth, Part B*, chapter 5, page 437. Editor J. W. Matthews. Academic Press, New York (1975).

[2] H. A. van der Vegt, J. Alvarez, X. Torelles, S. Ferrer, and E. Vlieg. *Indium-induced layer-by-layer growth and suppression of twin formation in the homoepitaxial growth of Cu(111).* Phys. Rev. B 52, 17443 (1995).

[3] J. Camarero, J. de la Figuera, J. J. de Miguel, R. Miranda, J. Álvarez, and S. Ferrer. *Structural characterisation and homoepitaxial growth on Cu(111).* Surface Science 459(1-2), 191–205 (2000).

[4] M. Giesen and H. Ibach. *Homoepitaxial growth on nominally flat and stepped Cu(111) surfaces: Island nucleation in fcc sites vs. hcp stacking fault sites.* Surf. Sci. 529, 135 (2003).

[5] K. Meinel, M. Klaua, and H. Bethge. *On twin and stacking fault formation during the epitaxial film growth of fcc materials on (111).* Phys. Stat. Sol. A 110, 189 (1988).

[6] S. A. de Vries, W. J. Huisman, P. Goedtkindt, M. J. Zwanenburg, S. L. Bennett, and E. Vlieg. *Floating stacking fault during homoepitaxial growth of Ag(111).* Phys. Rev. Lett. 81, 381–384 (1998).

[7] S. C. Wang and G. Ehrlich. *Structure, stability, and surface diffusion of clusters: Ir_x on Ir(111).* Surf. Sci. 239, 301–332 (1990).

[8] C. Busse, C. Polop, M. Müller, K. Albe, U. Linke, and T. Michely. *Stacking fault nucleation on Ir(111).* Phys. Rev. Lett. 91, 056103 (2003).

[9] M. Müller, K. Albe, C. Busse, A. Thoma, and T. Michely. *Island shapes, island densities, and stacking-fault formation on Ir(111): Kinetic Monte-Carlo simulations and experiments.* Phys. Rev. B 71, 075407 (2005).

[10] J. Camarero, L. Spendeler, G. Schmidt, K. Heinz, J. J. de Miguel, and R. Miranda. *Surfactant-induced suppression of twin formation during growth of fcc Co/Cu superlattices on Cu(111).* Phys. Rev. Lett. 73, 2448 (1994).

[11] P. L. Fevre, H. Magnan, O. Heckmann, V. Briois, and D. Chandesris. *Adsorption site, growth, and structure of Co on Cu(111) determined by multiple-scattering analysis of x-ray-absorption spectra.* Phys. Rev. B 52, 11462 (1995).

[12] M. Zheng, J. Shen, C. Mohan, P. Ohresser, J. Barthel, and J. Kirschner. *Suppression of the face-centered-cubic-hexagonal-close-packed stacking fault in Co/Cu(111) ultrathin films by pulsed laser deposition.* Appl. Phys. Lett. 74, 425 (1999).

[13] H. Holloway and D. J. Kubinski. *Giant magnetoresistance in Co/Cu multilayers with Co layers of alternating thicknesses: Reduction of magnetoresistive hysteresis.* Journal of Applied Physics 79, 7090–7094 (1996).

[14] D. J. Kubinski and H. Holloway. *Giant magnetoresistance in Co/Cu multilayers: Influence of Co thickness at the first antiferromagnetic maximum.* Journal of Applied Physics 79, 7395–7397 (1996).

[15] D. J. Monsma, J. C. Lodder, T. J. A. Popma, and B. Dieny. *Perpendicular hot electron spin-valve effect in a new magnetic field sensor: The spin-valve transistor.* Phys. Rev. Lett. 74, 5260–5263 (1995).

[16] D. J. Monsma, R. Vlutters, and J. C. Lodder. *Room temperature-operating spin-valve transistors formed by vacuum bonding.* Science 281, 407–498 (1998).

[17] M. Pratzer and H. J. Elmers. *Scanning tunneling spectroscopy of dislocations in ultrathin fcc and hcp Co films.* Phys. Rev. B 72, 035460 (2005).

[18] S. Krause, L. Berbil-Bautista, T. Hänke, F. Vonau, M. Bode, and R. Wiesendanger. *Consequences of line defects on the magnetic structure of high anisotropy films: Pinning centers on Dy/W(110).* Europhys. Lett. 76 (4), 637–643 (2006).

[19] L. Berbil-Bautista, S. Krause, M. Bode, and R. Wiesendanger. *Spin-polarized scanning tunneling microscopy and spectroscopy of ferromagnetic Dy(0001)/W(110) films.* Phys. Rev. B. 76, 064411 (2007).

[20] C. Busse, S. Baud, G. Bihlmayer, C. Polop, T. Michely, and S. Blügel. *Tunneling voltage dependent heights of faulted and unfaulted Ir islands on Ir(111).* Phys. Rev. B 68, 201401 (2003).

[21] A. L. Vázquez de Parga, F. J. García-Vidal, and R. Miranda. *Detecting electronic states at stacking faults in magnetic thin films by tunneling spectroscopy.* Phys. Rev. Lett. 85, 4365–4368 (2000).

[22] T. Shinohara, T. Sato, and T. Taniyama. *Surface ferromagnetism of Pd fine particles.* Phys. Rev. Lett. 91, 197201 (2003).

[23] B. Sampedro, P. Crespo, A. Hernando, R. Litrán, J. C. Sánchez-López, C. López-Cartes, A. Fernandez, J. Ramírez, J. González-Calbet, and M. Vallet. *Ferromagnetism in fcc twinned 2.4 nm size Pd nanoparticles.* Phys. Rev. Lett. 91, 237203 (2003).

[24] S. S. Alexandre, E. Anglada, J. M. Soler, and F. Yndurain. *Magnetism of two-dimensional defects in Pd: Stacking faults, twin boundaries, and surfaces.* Phys. Rev. B 74, 054405 (2006).

[25] F. Aguilera-Granja, J. M. Montejano-Carrizales, and A. Vega. *Twinning effects in the magnetism of small Pd clusters.* Solid State Com. 133, 573–578 (2005).

[26] H. Iwata, U. Lindefelt, S. Öberg, and P. R. Briddon. *Localized electronic states around stacking faults in silicon carbide.* Phys. Rev. B 65(3), 033203 (2001).

[27] U. Lindefelt, H. Iwata, S. Oberg, and P. R. Briddon. *Stacking faults in 3C-, 4H-, and 6H-SiC polytypes investigated by an ab initio supercell method.* Phys. Rev. B 67, 155204 (2003).

[28] J. Johansson, L. Karlsson, C. Svensson, T. Artensson, B. Wacaser, K. Deppert, L. Samuelson, and W. Seifert. *Structural properties of (111)B-oriented III–V nanowires.* Nature Materials 5(7), 574 (2006).

[29] S. Ha, M. Skowronski, J. J. Sumakeris, M. J. Paisley, and M. K. Das. *Driving force of stacking-fault formation in SiC p-i-n diodes.* Phys. Rev. Lett. 92, 175504 (2004).

[30] J. Wang, M. Tian, T. E. Mallouk, and M. H. W. Chan. *Microtwinning in template-synthesized single-crystal metal nanowires.* J. Phys. Chem. B 108, 841–845 (2004).

[31] F. E. Gabaly, W. L. Ling, K. F. McCarty, and J. de la Figuera. *The importance of threading dislocations on the motion of domain boundaries in thin films.* Science 308, 1303 (2005).

[32] W. L. Ling, N. C. Bartelt, K. F. McCarty, and C. B. Carter. *Twin boundaries can be moved by step edges during film growth.* Phys. Rev. Lett. 95, 166105 (2005).

[33] L. Royer. *Recherches expérimentales sur l'épitaxie ou orientation mutuelle de cristaux d'espèces differentes.* Bull. Soc. Fr.. Min. 51, 7 (1928).

[34] E. Bauer. *Phäenomenologische Theorie der Kristallabscheidung an Oberflächen.* Z. Kristallogr. 110, 372–394 (1958).

[35] T. Michely and J. Krug. *Islands, Mounds and Atoms.* Springer Series in Surf. Sci. Vol. 42, Berlin (2004).

[36] J. A. Venables, G. D. T. Spiller, and M. Hanbücken. *Nucleation and growth of thin films.* Reports on Progress in Physics 47(4), 399 (1984).

[37] S. C. Wang and G. Ehrlich. *Atom incorporation at surface clusters: An atomic view.* Phys. Rev. Lett. 67, 2509 (1991).

[38] F. C. Frank. *Crystal dislocations - elementary concepts and definitions.* Phil. Mag. 42, 809 (1951).

[39] R. D. Heidenreich and W. Shockley. *Report of a Conference on Strength of Solids.* Physical Society, London (1948).

[40] D. Hull. *Introduction to Dislocations (Second Edition).* Pergamon Press, Oxford (1975).

[41] M. Giesen, C. Steimer, and H. Ibach. *What does one learn from equilibrium shapes of two-dimensional islands on surfaces?* Surf. Sci. 471, 80–100 (2001).

[42] E. Lundgren, B. Stanka, M. Schmid, and P. Varga. *Thin films of Co on Pt(111): Strain relaxation and growth.* Phys. Rev. B 62, 2843 (2000).

[43] C. Busse. *Nucleation and stacking-faults on the Iridium (111) surface.* Ph.D. Thesis, Rheinisch-Westfälische Technische Hochschule Aachen, Aachen, Germany (2003).

[44] C. Polop, A. Lammerschop, C. Busse, and T. Michely. *Dependence of stacking-fault nucleation on cluster mobility.* Phys. Rev. B 71, 125423 (2005).

[45] S. Papadia, B. Piveteau, D. Spanjaard, and M. C. Desjonqueres. *Structural stability of adatom islands on fcc(111) transition-metal surfaces.* Phys. Rev. B 54, 14720 (1996).

[46] C. Busse, W. Langenkamp, C. Polop, A. Petersen, H. Hansen, U. Linke, P. J. Feibelman, and T. Michely. *Dimer binding energies on fcc(111) metal surfaces.* Surf. Sci. Lett. 539, L560–L566 (2003).

[47] S. C. Wang and G. Ehrlich. *Atomic behavior at individual binding sites: Ir, Re, and W on Ir(111).* Phys. Rev. Lett. 68(8), 1160–1163 (1992).

[48] S. C. Wang, U. Kürpick, and G. Ehrlich. *Surface diffusion of compact and other clusters: Ir_x on Ir(111).* Phys. Rev. Lett. 81(22), 4923–4926 (1998).

[49] C. Busse and T. Michely. *Self-healing of stacking faults in homoepitaxial growth on Ir(111).* Surf. Sci. 552, 281–293 (2004).

[50] C. Rosiepen. *Modellexperimente zum Wachstum und zur Texturentwicklung einer polykristallinen Ag-Schicht auf einem amorphen Si-Substrat.* Diplomarbeit, Rheinisch-Westfälische Technische Hochschule Aachen, Aachen, Germany (2005).

[51] T. Michely, M. Kaiser, and M. J. Rost. *Plug ‘n‘ play scanning probe microscopy.* Rev. Sci. Instrum. 71, 4461–4467 (2000).

[52] R. Baudoing-Savois, M. D. Santis, M. C. Saint-Lager, P. Dolle, O. Geaymond, P. Taunier, P. Jeantet, J. P. Roux, G. Renaud, A. Barbier, O. Robach, O. Ulrich, A. Mougin, and G. Bérard. *A new UHV diffractometer for surface structure and real time molecular beam deposition studies with synchrotron radiations at ESRF.* Nuclear Instruments and Methods in Physics Research Section B: Beam Interactions with Materials and Atoms 149(1-2), 213 – 227 (1999).

[53] R. Baudoing-Savois, G. Renaud, M. D. Santis, A. Barbier, O. Robach, P. Taunier, P. Jeantet, O. Ulrich, J. P. Roux, M. C. Saint-Lager, A. Barski, O. Geaymond, G. Bérard, P. Dolle, M. Noblet, and A. Mougin. *Erratum to: A new UHV diffractometer for surface structure and real time molecular beam deposition studies with synchrotron radiations at ESRF [Nucl. Instr. and Meth. B 149 (1999) 213].* Nuclear Instruments and Methods in Physics Research Section B: Beam Interactions with Materials and Atoms 159(1-2), 120 – 120 (1999).

[54] B. Henke, E. Gullikson, and J. Davis. *X-ray interactions: Photoabsorption, scattering, transmission, and reflection at E=50-30000eV, Z=1-92.* Atomic Data and Nuclear Data Tables 54, 181–342 (1993).

[55] R. Feidenhansl. *Surface structure determination by x-ray diffraction.* Surf. Sci. Rep. 10, 105–188 (1989).

[56] S. R. Andrews and R. Cowley. *Scattering of x-rays from crystal surfaces.* J. Phys. C: Solid State Phys. 18, 6427–6439. (1985).

[57] I. K. Robinson. *Crystal truncation rods and surface roughness.* Phys. Rev. B 33, 3830–3836 (1986).

[58] I. K. Robinson and D. J. Tweet. *Surface x-ray diffraction.* Rep. Prog. Phys. 55, 599–651 (1992).

[59] H. Dosch, B. W. Batterman, and D. C. Wack. *Depth-controlled grazing-incidence diffraction of synchrotron x radiation.* Phys. Rev. Lett. 56, 1144–1147 (1986).

[60] S. de Vries. *Interface structure of growing crystals.* Ph.D. Thesis, FOM Institute for Atomic and Molecular Physics, Amsterdam, The Netherlands (1999). ISBN 90-9012353-9.

[61] C. P. Wang, K. B. Do, M. R. Beasley, T. H. Geballe, and R. H. Hammond. *Deposition of in-plane textured MgO on amorphous Si3N4 substrates by ion-beam-assisted deposition and comparisons with ion-beam-assisted deposited yttria-stabilized-zirconia.* Appl. Phys. Lett. 71, 2955 (1997).

[62] S. Kreiskott, P. N. Arendt, J. Y. Coulter, P. C. Dowden, S. R. Foltyn, B. J. Gibbons, V. Matias, and C. J. Sheehan. *Reel-to-reel preparation*

of ion-beam assisted deposition (IBAD)-MgO based coated conductors. Supercond. Sci. Technol. 17, S132–S134 (2004).

[63] N. Ghafoor, F. Eriksson, P. Persson, L. Hultman, and J. Birch. *Effects of ion-assisted growth on the layer definition in Cr/Sc multilayers.* Thin Solid Films 56, 982–990 (2008).

[64] S. Esch, M. Breeman, M. Morgenstern, and T. Michely. *Nucleation and morphology of homoepitaxial Pt(111)-films grown with ion beam assisted deposition.* Surf. Sci. 365, 187–204 (1996).

[65] G. E. Lane and J. C. Anderson. *The nucleation and initial growth of gold films deposited onto sodium chloride by ion-beam sputtering.* Thin Solid Films 26, 5–23 (1975).

[66] C.-H. Choi, R. Ai, and S. A. Barnett. *Suppression of three-dimensional island nucleation during GaAs growth on Si(100).* Phys. Rev. Lett. 67, 2826 (1991).

[67] G. Rosenfeld, R. Servaty, C. Teichert, B. Poelsema, and G. Comsa. *Layer-by-layer growth of Ag on Ag(111) included by enhanced nucleation: A model study for surfactant-mediated growth.* Phys. Rev. Lett. 71, 895 (1993).

[68] J. Meyer and R. Behm. *Comment on: Layer-by-layer growth of Ag on Ag(111) included by enhanced nucleation: A model study for surfactant-mediated growth.* Phys. Rev. Lett. 73, 364 (1994).

[69] M. Marinov. *Effect of ion bombardment on the initial stages of thin film growth.* Thin Solid Films 46, 267–274 (1977).

[70] M. V. R. Murty and H. A. Atwater. *Very low temperature (<400 °c) silicon molecular beam epitaxy: The role of low energy ion irradiation.* Appl. Phys. Lett. 62, 2566 (1993).

[71] S. Bleikamp, A. Thoma, C. Polop, G. Pirug, U. Linke, and T. Michely. *New growth mode through decorated twin boundaries.* Phys. Rev. Lett. 96, 115503 (2006).

[72] S. Bleikamp, A. Thoma, C. Polop, and T. Michely. *Stacking faults in homoepitaxy on Ir(111): Detection, evolution with film thickness, and associated defect patterns.* Phys. Rev. B 77, 245424 (2008).

[73] A. Thoma and T. Michely. (unpublished).

[74] M. Rost, P. Šmilauer, and J. Krug. *Unstable epitaxy on vicinal surfaces.* Surf. Sci. 369, 393 (1996).

[75] I. Horcas, R. Fernandez, J. M. Gomez-Rodriguez, J. Colchero, J. Gomez-Herrero, and A. M. Baro. *WSXM: A software for scanning probe microscopy and a tool for nanotechnology.* Rev. Sci. Instrum. 78, 013705 (2007).

[76] N. M. Rosengaard and H. L. Skriver. *Calculated stacking-fault energies of elemental metals.* Phys. Rev. B 47, 12865 (1993).

[77] J. C. Hamilton, M. R. Sorensen, and A. F. Voter. *Compact surface-cluster diffusion by concerted rotation and translation.* Phys. Rev. B 61, R5125 (2000).

[78] J. B. Pendry. *Low Energy Electron Diffraction.* Academic Press, London (1974).

[79] M. A. van Hove, W. H. Weinberg, and C. M. Chan. *Low-Energy Electron Diffraction.* Springer-Verlag, Berlin (1986).

[80] M. Kalff, G. Comsa, and T. Michely. *How sensitive is epitaxial growth to adsorbates?* Phys. Rev. Lett. 81, 1255–1258 (1998).

[81] F. E. Gabaly, J. M. Puerta, C. Klein, A. Saa, A. K. Schmid, K. F. McCarty, J. I. Cerda, and J. del la Figuera. *Structure and morphology of ultrathin Co/Ru(0001) films.* New J. Phys. 9, 80 (2007).

[82] E. A. Marquis, D. L. Medlin, and F. Léonard. *Stabilization of extended stacking faults by {111}/{112} twin junction interactions.* Acta Materialia 55(17), 5917 – 5923 (2007).

[83] K. L. Merkle and D. Wolf. *Low-energy configurations of symmetric and asymmetric tilt grain boundaries.* Philosophical Magazine A 65:2, 513–530 (1992).

[84] U. Wolf, F. Ernst, T. Muschik, M. Finnis, and H. Fischmeister. *The influence of grain boundary inclination on the structure and energy of $\sigma = 3$ grain boundaries in copper.* Philosophical Magazine A 66:6, 991–1016 (1992).

[85] R. Fullman. Technical Report RL-422, SO-2006, General Electric Research Laboratory Research Report (1950).

[86] R. Fullman. *Interfacial free energy of coherent twin boundaries in copper.* Journal of Applied Physics 22, 448 (1951).

[87] R. Fullman. *Cristallography and interfacial free energy of noncoherent twin boundaries in copper.* Journal of Applied Physics 22, 456 (1951).

[88] B. Poelsema, J. B. Hannon, N. C. Bartelt, and G. L. Kellogg. *Bulk-surface vacancy exchange on pt(111).* Applied Physics Letters 84, 2551–2553 (2004).

[89] D. R. Lide, editor. *CRC Handbook of Chemistry and Physics.* CRC Press, Boca Raton, New York, 78th edition (1997-1998).

[90] S. Bleikamp and T. Michely. *Ion assistance in epitaxial growth as a strategy to suppress twinning.* Thin Solid Films 518, 1914–1919 (2010).

[91] H. Hansen, C. Polop, T. Michely, A. Friedrich, and H. M. Urbassek. *Step edge sputtering yield at grazing incidence ion bombardment.* Phys. Rev. Lett. 92(24), 246106 (2004).

[92] A. Redinger, Y. Rosandi, H. M. Urbassek, and T. Michely. *Step-edge sputtering through grazing incidence ions investigated by scanning tunneling microscopy and molecular dynamics simulations.* Phys. Rev. B 77, 195436 (2008).

[93] T. Michely, K. H. Besocke, and G. Comsa. *Observation of sputtering damage on Au(111).* Surf. Sci. 230, L135 – L139 (1990).

[94] Z. Zhang and M. G. Lagally. *Atomic-scale mechanisms for surfactant-mediated layer-by-layer growth in homoepitaxy.* Phys. Rev. Lett. 72, 693–696 (1994).

[95] S. Esch, M. Hohage, T. Michely, and G. Comsa. *Origin of oxygen induced layer-by-layer growth in homoepitaxy on Pt(111).* Phys. Rev. Lett. 72, 518–521 (1994).

[96] H. A. van der Vegt, H. M. van Pinxteren, M. Lohmeier, E. Vlieg, and J. M. C. Thornton. *Surfactant-induced layer-by-layer growth of Ag on Ag(111).* Phys. Rev. Lett. 68, 3335–3338 (1992).

[97] W. P. Krekelberg, J. Greeley, and M. Mavrikakis. *Atomic and molecular adsorption on Ir(111).* J. Phys. Chem. B 108, 987 (2004).

[98] J. Lauterbach, R. W. Boyle, M. Schick, W. J. Mitchell, B. Meng, and W. H. Weinberg. *The adsorption of CO on Ir(111) investigated with FT-IRAS.* Surf. Sci. 350, 32 (1996).

[99] D. I. Hagen, B. E. Nieuwenhuys, G. Rovida, and G. Somorjai. *LEED, Auger, and TDS of chemisorbed CO and O2 on the (111) Iridium surfaces.* Surf. Sci. 57, 632 (1976).

[100] C. M. Chan and W. H. Weinberg. *LEED structural analysis of the (2x2) oxygen overlayer on the Ir(111) surface.* J. Chem. Phys. 71, 2788 (1979).

[101] Y. Xu and M. Mavrikakis. *Adsorption and dissociation of O_2 on Ir111.* Journal of Chemical Physics 116, 10846 (2002).

[102] P. A. Zhdan, G. K. Boreskov, and A. I. Boronin. *An XPS investigation of the chemisorption of Oxygen on the Iridium (111) surface.* Surface Science 61, 25–36 (1976).

[103] T. S. Marinova and K. L. Kostov. *Interaction of Oxygen with a clean Ir(111) surface.* Surface Science 185, 203–212 (1987).

[104] A. Thoma. *Wachstum unter Einfluß von Stapelfehlern im System Ir/Ir(111).* Diplomarbeit, Rheinisch-Westfälische Technische Hochschule Aachen, Aachen, Germany (2004).

List of Publications

Parts of the results presented in this thesis have been published in the following publications:

[1] S. Bleikamp, A. Thoma, C. Polop, G. Pirug, U. Linke, and T. Michely.
New Growth Mode through Decorated Twin Boundaries.
Physical Review Letters 96, 115503 (2006).

[2] S. Bleikamp, A. Thoma, C. Polop, and T. Michely.
Stacking faults in homoepitaxy on Ir(111): Detection, evolution with film thickness, and associated defect patterns.
Physical Review B 77, 245424 (2008).

[3] S. Bleikamp, and T. Michely.
Ion assistance in epitaxial growth as a strategy to suppress twinning.
Thin Solid Films 518, 1914–1919 (2010).

[4] S. Bleikamp, J. Coraux, and T. Michely.
Twins and their boundaries during homoepitaxy on Ir(111).
In preparation.

Publications on other topics:

[5] A. T. N'Diaye, S. Bleikamp, P. J. Feibelman, and T. Michely.
Two-Dimensional Ir Cluster Lattice on a Graphene Moiré on Ir(111).
Physical Review Letters 97, 215501 (2006).

[6] C. Polop, C. Rosiepen, S. Bleikamp, R. Drese, J. Mayer, A. Dimyati, and T. Michely.
The STM view of the initial stages of polycrystalline Ag film formation.
New Journal of Physics 9, 74 (2007).

[7] D. Förster, S. Bleikamp, and T. Michely.
Biaxially textured Ag films by grazing ion beam assisted deposition.
Submitted to Thin Solid Films.

Deutsche Kurzfassung

Das Wachstums- und Ausheilverhalten von homoepitaktischen dünnen Iridiumschichten auf Ir(111) wurde mittels Rastertunnelmikroskopie (engl. *scanning tunneling microscopy*, STM), Beugung von niederenergetischen Elektronen (engl. *low energy electron diffraction*, LEED) und oberflächennaher Röntgenbeugung (engl. *surface X-ray diffraction*, SXRD) im Hinblick auf die Bildung von Stapelfehlern und die daraus resultierende Verzwilligung untersucht.

Durch heterogene Nukleation weiterer Stapelfehler an Phasengrenzen zwischen regulärem und fehlgestapelten Gebiet breiten sich fehlgestapelte Gebiete in der nächsthöheren Lage in ihre Umgebung aus (Proliferations-Effekt). In diesem Prozess werden die Phasengrenzen überwachsen, stabilisiert und entwickeln sich zu persistenten Fehlerstrukturen. Dies führt zu einem Übergang von dem ursprünglichen Lage-für-Lage-Wachstumssmodus zu einem heterogenen, defektorientiertem Wachstum und einer überwiegenden Verzwilligung der Oberfläche. Es zeigt sich, dass Stufenkanten die Wahrscheinlichkeit der Bildung von Stapelfehlern erhöhen und damit diesem Prozess anfänglich Vortrieb leisten.

Durch die Zuführung von zusätzlicher Energie in Größenordnung von 50 eV während der Deposition mittels Ionenstrahl-unterstützter Deposition (engl. *ion beam assisted deposition*, IBAD) kann die Bildung von Stapelfehlern und Verzwilligung effektiv aufgehoben werden. Verschiedene Verfahren wurden hierzu getestet.

Die verzwillingten Bereiche der stark verzwillingten Ir/Ir(111)-Filme weisen eine hohe Stabilität gegen thermisches Ausheilen auf. Die Ausheilung findet in einem zweistufigen Prozess statt: Zwischen 800 K bis 1000 K verringern sich zuerst lediglich die Grenzflächen zwischen Gebieten unterschiedlicher Stapelung. Erst beginnend mit Temperaturen von über 1200 K verringert sich der Anteil an verzwillingter Stapelung. Strukturmodelle für die verschiedenen Grenzflächen wurden entwickelt. Die Grenzflächen zwischen Gebieten unterschiedlicher Stapelung bestehen aus {111}/{115} Grenzflächen, welche in eine Struktur aus {111}/{111} und {112}/{552} Grenzflächen dissoziieren.

Anhand von CO und O wurde der Einfluss von Adsorbaten auf das Wachstum von Ir/Ir(111) untersucht. Die Exposition der Probe zu CO oder O während der Deposition verhindert die Koaleszenz der Filme, führt zu säulenartigem Wachstum und mehrfacher Verzwilligung der einzelnen Säulen. Bei beiden Adsorbaten ist die Inseldichte erhöht, was auf eine reduzierte Mobilität an der Oberfläche schließen lässt.

Danksagung

Ohne die Unterstützung und Hilfestellung von vielen verschiedenen Personen wäre diese Arbeit nicht möglich gewesen. Dafür möchte ich mich bei diesen Personen ganz herzlich bedanken. Einige von ihnen möchte ich hier besonders erwähnen:

Ich bedanke mich bei Herrn Prof. Dr. Thomas Michely für die Möglichkeit, diese Arbeit in seiner Arbeitsgruppe anzufertigen, und für die Betreuung dieser Arbeit. Die mit ihm geführten Diskussionen haben maßgeblich zu dieser Arbeit beigetragen.

Prof. Dr. Mohsen Abd-Elmeguid war so freundlich, sich als zweiter Betreuer zur Verfügung zu stellen.

Ich bedanke mich bei Herrn Dr. Johann Coraux, Frau Dr. Odile Robach und Herrn Dr. Gilles Renaud, die sich als Kooperationspartner für die SXRD-Messungen an der ESRF zur Verfügung gestellt und auch die zugehörigen Simulationen durchgeführt haben.

Herrn Dr. Carsten Busse und Herrn Arne Thoma, welche die vorhergehenden Untersuchungen durchgeführt haben, auf denen diese Arbeit aufbaut, danke ich für manche Anregung und für ihre Bereitschaft zur Diskussion.

Weiterhin danke ich auch den Technikern und Mitarbeitern der mechanischen und elektronischen Werkstätten des I. Physikalischen Instituts der RWTH Aachen und des 2. Physikalischen Instituts der Universität zu Köln, welche alle anfallenden Arbeiten schnell und sorgfältig ausführten.

Auch möchte ich mich bei allen Mitgliedern der Arbeitsgruppe und der Institute für die gute Zusammenarbeit und das produktive Arbeitsumfeld bedanken.

Abschließend möchte ich mich auch bei meiner Familie und meinen Freunden bedanken, die mich stets unterstützt haben.

Diese Arbeit entstand im Rahmen des durch die Deutsche Forschungsgemeinschaft geförderten Projektes “Kinetics of stacking faults in thin films” und wäre ohne die finanzielle Unterstützung nicht möglich gewesen.

Offizielle Erklärung

Ich versichere, dass ich die von mir vorgelegte Dissertation selbständig angefertigt, die benutzten Quellen und Hilfsmittel vollständig angegeben und die Stellen der Arbeit – einschließlich Tabellen, Karten und Abbildungen –, die anderen Werken im Wortlaut oder dem Sinn nach entnommen sind, in jedem Einzelfall als Entlehnung kenntlich gemacht habe; dass diese Dissertation noch keiner anderen Fakultät oder Universität zur Prüfung vorgelegen hat; dass sie – abgesehen von unten angegebenen Teilpublikationen – noch nicht veröffentlicht worden ist sowie, dass ich eine solche Veröffentlichung vor Abschluss des Promotionsverfahrens nicht vornehmen werde. Die Bestimmungen der Promotionsordnung sind mir bekannt. Die von mir vorgelegte Dissertation ist von Prof. Dr. Thomas Michely betreut worden.

Köln, den 18. Februar 2010

Sebastian Bleikamp

Lebenslauf

	Sebastian Bleikamp Diplom-Physiker
Anschrift	Jakobstraße 96, 52064 Aachen
Geburtsdatum	8. Februar 1978
Geburtsort	Oberhausen
Familienstand	ledig
Staatsangehörigkeit	deutsch
Schulausbildung	
1985 – 1989	Städtische Gemeinschaftsgrundschule am Oemberg, Mülheim an der Ruhr
1989 - 1998	Gymnasium Karl-Ziegler-Schule, Mülheim an der Ruhr
Juni 1998	Abitur
Studium	
1998 - 2005	Studium der Physik an der Rheinisch-Westfälischen Technischen Hochschule (RWTH) Aachen
2004 - 2005	Diplomarbeit bei Prof. Dr. Thomas Michely I. Physikalisches Institut, RWTH Aachen Thema: *Einfluß von Defekten auf die morphologische Entwicklung von fcc(111) Metalloberflächen*
Promotion	
2005 - 2010	Promotion bei Prof. Dr. Thomas Michely
bis 2007	I. Physikalisches Institut, RWTH Aachen
ab 2007	II. Physikalisches Institut, Universität zu Köln Thema: *Stacking Faults and Twinning in Homoepitaxial Thin Films on Ir(111)*